

HZDR-070

# TERAHERTZ NEAR-FIELD INVESTIGATION OF A PLASMONIC GaAs SUPERLENS

Markus Fehrenbacher

Wissenschaftlich Technische Berichte  
HZDR-070 · ISSN 2191-8708

WISSENSCHAFTLICH-  
TECHNISCHE BERICHTE

**hzdr**



HELMHOLTZ  
ZENTRUM DRESDEN  
ROSSENDORF

Druckausgabe: ISSN 2191-8708

Elektronische Ausgabe: ISSN 2191-8716

Die elektronische Ausgabe erscheint unter Creative Commons License (CC BY 4.0):

<https://www.hzdr.de/publications/Publ-23470>

<urn:nbn:de:bsz:d120-qucosa-200855>

Die vorliegende Arbeit wurde sowohl als Dissertation an der Fakultät Mathematik und Naturwissenschaften der Technischen Universität Dresden sowie als Wissenschaftlich-Technischer Bericht des Helmholtz-Zentrum Dresden – Rossendorf mit der Berichtsnummer **HZDR-070** veröffentlicht.

2016

Herausgegeben vom

Helmholtz-Zentrum Dresden - Rossendorf

Bautzner Landstraße 400

01328 Dresden

Germany

Wissenschaftlich-Technische Berichte  
HZDR-070

Markus Fehrenbacher

**TERAHERTZ NEAR-FIELD INVESTIGATION  
OF A PLASMONIC GaAs SUPERLENS**

**HZDR**

 **HELMHOLTZ**  
| ZENTRUM DRESDEN  
| ROSSENDORF

---

---

# Terahertz Near-field Investigation of a Plasmonic GaAs Superlens

DISSERTATION

zur Erlangung des akademischen Grades  
Doctor rerum naturalium  
(Dr. rer. nat.)

durchgeführt am

Helmholtz-Zentrum Dresden-Rossendorf  
Institut für Ionenstrahlphysik und Materialforschung

eingereicht an der

Fakultät Mathematik und Naturwissenschaften  
der Technischen Universität Dresden

von

Dipl.-Phys. Markus Fehrenbacher  
geboren am 08.07.1985 in Schramberg

Eingereicht am 28.10.2015

Verteidigt am 03.03.2016

1. Gutachter: Prof. Dr. Manfred Helm (TU Dresden)
2. Gutachter: Prof. Dr. Thomas Taubner (RWTH Aachen)

# Abstract

This work presents the first demonstration of a semiconductor based plasmonic near-field superlens, utilizing highly doped GaAs to generate infrared optical images with a spatial resolution beyond the diffraction limit. Being easily transferable to other semiconductor materials, the concept described in this thesis can be exploited to realize spectrally adjustable superlenses in a wide spectral range.

The idea of superlensing has been introduced theoretically in 2000, followed by numerous publications including experimental studies. The effect initiated great interest in optics, since in contrast to diffraction limited conventional optical microscopy it enables subwavelength resolved imaging by reconstructing the evanescent waves emerging from an object. With techniques like scanning near-field optical microscopy (SNOM) and stimulated emission depletion (STED) being already successfully established to overcome the conventional restrictions, the concept of superlensing provides a novel, different route towards high resolution. Superlensing is a resonant phenomenon, relying either on the excitation of surface plasmons in metallic systems or on phonon resonances in dielectric structures. In this respect a superlens based on doped semiconductor benefits from the potential to be controlled in its operational wavelength by shifting the plasma frequency through adjustment of the free carrier concentration.

For a proof of principle demonstration, we investigate a superlens consisting of a highly n-doped GaAs layer ( $n = 4 \times 10^{18} \text{cm}^{-3}$ ) sandwiched between two intrinsic layers. Recording near-field images of subwavelength sized gold stripes through the trilayer structure by means of SNOM in combination with a free-electron laser, we observe both enhanced signal and improved spatial resolution at radiation wavelengths close to  $\lambda = 22 \mu\text{m}$ , which is in excellent agreement with simulations based on the Drude-Lorentz model of free electrons. Here, comparative investigations of a purely intrinsic reference sample confirm that the effect is mediated by the charge carriers within the doped layer. Furthermore, slightly differently doped samples provide indications for the expected spectral shift of the resonance. According to our calculations, the wavelength range to be exploited by n-GaAs based superlenses reaches far into the terahertz region, whereas other semiconductor materials are required to explore the near infrared.



# Contents

<b>Abstract</b>	<b>iii</b>
<b>1 Introduction</b>	<b>1</b>
<b>2 The diffraction limit</b>	<b>5</b>
<b>3 Fundamentals I - Superlensing</b>	<b>9</b>
3.1 The perfect lens . . . . .	9
3.1.1 Negative refraction . . . . .	10
3.1.2 Amplification of evanescent waves . . . . .	13
3.1.3 Static limit . . . . .	17
3.2 The superlens . . . . .	18
3.2.1 Practical limitations . . . . .	18
3.2.2 Obtainable resolution of a near-field superlens . . . . .	19
3.2.3 Transfer function . . . . .	22
3.3 A different point of view: Plasmonics . . . . .	25
3.4 From first experiments to the GaAs superlens . . . . .	28
<b>4 Fundamentals II - Near-field optical microscopy</b>	<b>31</b>
4.1 Concept . . . . .	31
4.2 s-SNOM theory . . . . .	32
4.2.1 Emission of an oscillating dipole . . . . .	33
4.2.2 Model of dipole and image dipole . . . . .	33
4.2.3 Scattering characteristics . . . . .	36
4.3 AFM tip as a scatterer . . . . .	41
4.4 Signal formation . . . . .	42
<b>5 Doped GaAs as a superlens material</b>	<b>49</b>
5.1 Concept . . . . .	49
5.2 Infrared dielectric function . . . . .	50



5.3	Damping versus electron density . . . . .	53
5.4	Superlensing condition adjustable by doping . . . . .	54
5.5	Role of the effective mass . . . . .	57
<b>6</b>	<b>Preparation and characterization</b>	<b>61</b>
6.1	Preparation . . . . .	61
6.2	Topography . . . . .	63
6.3	Electronic properties . . . . .	65
6.3.1	Fourier transform infrared spectroscopy . . . . .	66
6.3.2	Hall measurements . . . . .	67
6.3.3	Summary and comments . . . . .	69
6.4	Exclusion of resonant artifacts . . . . .	71
<b>7</b>	<b>Experimental details</b>	<b>75</b>
7.1	AFM to probe the near-field . . . . .	75
7.2	Radiation source FELBE . . . . .	80
7.3	s-SNOM setup and adjustment . . . . .	83
7.4	Direct detection at FELBE . . . . .	85
<b>8</b>	<b>Results of near-field investigation</b>	<b>87</b>
8.1	Sample overview and expectations . . . . .	87
8.2	Data acquisition and evaluation . . . . .	90
8.3	Imaging a periodic stripe-pattern . . . . .	91
8.3.1	Doping induced near-field enhancement . . . . .	91
8.3.2	Spectral dependence of the superlensing effect . . . . .	93
8.3.3	Near-field resonance of the doped layer . . . . .	96
8.3.4	Comparison of various superlens structures - indication of spectral tuning . . . . .	99
8.4	Imaging a non-periodic object . . . . .	101
8.5	Distance dependence . . . . .	103
8.6	Bandwidth of superlensing - discussion . . . . .	105
<b>9</b>	<b>Conclusion and outlook</b>	<b>109</b>
	<b>Bibliography</b>	<b>113</b>
	<b>Acknowledgement</b>	<b>123</b>





# 1 Introduction

Nowadays, progress in both science and industry is often connected with understanding the functionality of structures and devices on a continually decreasing scale. The rapid developments within the last decades, no matter if in biomedicine or data storage, would have been impossible without the enormous capabilities of a variety of microscopy techniques. Meanwhile, images at a nanometer spatial resolution or even beyond are routinely obtained. Smallest structures are resolved by electron microscopy [1], scanning tunnel microscopy (STM) [2] and atomic force microscopy (AFM) [3], enabling to identify single atoms in a crystal lattice. However, all of these techniques only yield little or no chemical information about a sample. This is in contrast to optical microscopy, since photon energies are in the range of binding energies in matter. Here, electronic and vibrational transitions are typically probed by visible and infrared light, respectively. Besides, in contrast to the above mentioned high resolution methods, light allows for imaging the interior of optically transparent objects, like the inner structure of a living cell. There is no doubt that high resolution optical microscopy is of tremendous interest in various areas of research.

Unfortunately, the wave nature of electromagnetic radiation imposes fundamental limitations on the obtainable resolution of conventional optical microscopy. This restriction is known as the *diffraction limit*. It was shown in 1873 by Ernst Abbe [4] that no structures smaller than about half the wavelength can be resolved, and consequently nanomaterials cannot be imaged by visible light. Techniques like solid immersion microscopy [5] or  $4\pi$ -microscopy [6] have been established to enhance the resolution by increasing the aperture of the objective, however they obey the limit set by diffraction. In order to achieve deep subwavelength resolution, other concepts are required and indeed have been realized.

Two main approaches have evolved which meanwhile enable optical microscopy far beyond the diffraction limit. On the one hand, there is stimulated emission depletion (STED) microscopy [7] (and other closely related techniques), which was awarded with the Nobel Prize in chemistry in 2014. Here, two laser beams overlapping at their foci are raster-scanned across a fluorescent structure, where one of them triggers the fluorescence and the other one, providing a doughnut shaped profile, switches it off again. The size of the remaining fluorescent area in the center of the doughnut depends on the intensity of

the second laser, providing a resolution that is not limited by the wavelength of the first, stimulating laser. On the other hand, scanning near-field optical microscopy (SNOM) [8, 9] makes use of the localized near-field interaction between a pointed probe and the sample of interest, yielding optical information on a scale of the probe's apex rather than the applied wavelength. Both sorts of microscopes are commercially available and frequently applied. While STED opens up unforeseen opportunities in virology, neuroscience and tumor research, SNOM has enabled a vast number of spectroscopic studies on the nanometer scale in material science. However, without diminishing these very important achievements, both STED and SNOM also exhibit profound disadvantages as compared to conventional optical microscopy. STED, on the one hand, relies on fluorescence of the object of interest, restricting its application mainly to biomedicine, where fluorescent labeling [10] is a common approach to identify structures in cells. Hence, it does not yield immediate chemical information, since the attached dyes are imaged rather than the objects themselves. This in contrast to SNOM, where light directly interacts with the sample. In particular, *scattering-type* SNOM (s-SNOM) [9, 11, 12] allows for almost wavelength independent performance, whereas *aperture* SNOM (a-SNOM) [8, 13] is basically limited to the visible range, since cutoff effects [14, 15] strongly suppress the transmission of infrared radiation through nanometer scaled apertures of tapered probes. By combining s-SNOM with Fourier transform infrared spectroscopy (FTIR) [16, 17] or tunable laser sources such as a free-electron laser [18, 19], optical characterization with nanometer spatial resolution becomes possible over a wide spectral range. In the case of SNOM, the drawback arises from the fact that it measures the evanescently decaying near field of a sample, making it only suitable for surface studies with poor sensitivity for buried objects ( $\approx 100$  nm depth) [20, 21] as compared to the conventional far-field approach. Finally, it should also be mentioned that both STED and SNOM are scanning techniques, giving rise to long acquisition times when imaging large areas with high resolution.

In 2000, a theoretical study of the British physicist John Pendry [22] initiated the *quest for the superlens* [23], a new kind of optical lens promising to overcome all the above mentioned restrictions. Such a superlens works similarly to a conventional lens, however it not only reconstructs the propagating waves emerging from an object, which gives rise to a diffraction limited image, but also the near field, where all the fine details of the object are contained. Here, the obtainable resolution is not limited by diffraction, but rather by the quality of the superlens. It soon became clear that due to dissipation, inherent to all materials, images with subwavelength resolution are only possible to be obtained over very short distances [24], i.e. on the order of the wavelength used. Nevertheless, this innovative concept gave rise to a wealth of both theoretical and experimental studies, also including

ideas for practical application such as in photolithography [25].

The present work deals with a particular version of a superlens, the *plasmonic near-field superlens*, which is a thin metallic layer that allows for near-field imaging via coupled surface plasmons. For the first time, it is experimentally demonstrated [26] that a doped semiconductor, n-GaAs, is capable of superlensing, where the operational wavelength can be adjusted by changing the doping level.

This thesis is organized as follows. In Chapter 2 we first introduce the diffraction limit, where this whole work is all about overcoming this limitation. The concept of the superlens with its idealized counterpart, the *perfect lens*, is discussed theoretically in Chapter 3, and an overview about previous experimental work is given. For measuring the near-field images obtained via the GaAs superlens we apply s-SNOM (see above), which records the evanescent waves in the image plane. Chapter 4 provides the fundamentals of this microscopy technique. After that, in Chapter 5, the optical properties of n-GaAs are discussed in detail, focusing on the expected superlens performance. This is followed by presenting the preparation and characterization of the samples (Chapter 6) as well as the experimental methods (Chapter 7), the latter including a short introduction on the functionality of a free-electron laser, which was exploited as radiation source. Finally, the experimental results are shown and discussed in Chapter 8, whereupon Chapter 9 completes the thesis by a conclusion and outlook. Each chapter starts with a short introduction which at the same time summarizes the main aspects.



## 2 The diffraction limit

*In this first short chapter, the diffraction limit is introduced, fundamentally limiting the obtainable spatial resolution of conventional optical microscopy. This is the starting point of this thesis, which is all about overcoming this limitation by a phenomenon referred to as superlensing.*

In conventional optical microscopy, the resolution of an image is constrained by the wavelength  $\lambda$  of the applied radiation. This was for the first time shown by Ernst Abbe in 1873 [4] and can be described as follows [22].

Let us consider a 2D object in the  $x$ - $y$  plane emitting electromagnetic radiation at an angular frequency  $\omega$ . For simplicity, the object is assumed to be surrounded by air. The electric field component can be written as a Fourier expansion,

$$\mathbf{E}(\mathbf{r}, t) = \sum_{\sigma, k_x, k_y} \mathbf{E}^\sigma(k_x, k_y) \cdot e^{ik_x x + ik_y y + ik_z z - i\omega t}. \quad (2.0.1)$$

Here, the index  $\sigma$  accounts for different polarization states and the components of the wave vector  $\mathbf{k}$  are interconnected via

$$\mathbf{k}^2 = k_x^2 + k_y^2 + k_z^2 = \frac{\omega^2}{c^2}, \quad (2.0.2)$$

( $c$  is the speed of light) which follows from the wave equation

$$\nabla^2 \mathbf{E} - \frac{1}{c^2} \frac{\partial^2 \mathbf{E}}{\partial t^2} = 0. \quad (2.0.3)$$

The microscope reconstructs the distribution of the electric (and magnetic) field on the object's surface, where contrast arises from in-plane variations. For a given wave, this variation is characterized by the  $x$ - $y$ -projection of  $\mathbf{k}$  with large wavenumbers corresponding to high resolution. Here, the length scale  $\Delta$  of observed structures is given by

$$\Delta = \frac{2\pi}{\sqrt{k_x^2 + k_y^2}}. \quad (2.0.4)$$



To be captured by the microscope, light has to travel in  $z$ -direction. For  $k_z$  there are two regimes, following Equation 2.0.2:

$$k_z = +\sqrt{\frac{\omega^2}{c^2} - k_x^2 - k_y^2} \quad \text{for} \quad \frac{\omega^2}{c^2} > k_x^2 + k_y^2, \quad (2.0.5)$$

$$k_z = +i\sqrt{k_x^2 + k_y^2 - \frac{\omega^2}{c^2}} \quad \text{for} \quad \frac{\omega^2}{c^2} < k_x^2 + k_y^2. \quad (2.0.6)$$

The first case yields propagating waves, whereas the latter results in

$$\mathbf{E}(\mathbf{r}, t) = \sum_{\sigma, k_x, k_y} \mathbf{E}^\sigma(k_x, k_y) \cdot e^{ik_x x + ik_y y - i\omega t} \cdot e^{-\tilde{k}_z z}, \quad (2.0.7)$$

with  $\tilde{k}_z = -ik_z$  being a real positive number. Equation 2.0.7 describes evanescent waves which decay exponentially with  $z$  within the so called *near-field region*. This part of the emitted radiation does not reach the lens of the microscope, which only captures the propagating waves. Hence, values of the transverse wave vector larger than  $k_{max} = \omega/c$  do not contribute to the image, resulting in a minimum of observable structure size in the order of

$$\Delta_{min} \approx \frac{2\pi}{k_{max}} = \frac{2\pi c}{\omega} = \lambda. \quad (2.0.8)$$

This fundamental limitation is called the *diffraction limit*.

More practically orientated, the obtainable resolution of a lens [27] is usually given by

$$\Delta_{min} \approx 1.22 \frac{\lambda}{2NA}, \quad (2.0.9)$$

with the numerical aperture

$$NA = n^* \cdot \sin \theta. \quad (2.0.10)$$

Here,  $\theta$  is the half-angle of the cone of light emitted from the object towards the lens (see Figure 2.0.1) and  $n^*$  is the refractive index of the medium surrounding the lens. Note that the prefactor 1.22 results from a rather arbitrary definition of resolution (Rayleigh criterion). At a given distance between lens and object, a lens with a large diameter  $D$  results in a large  $NA$  and, hence, provides a better resolution  $\Delta_{min}$  than a small lens. This can be understood by considering the theoretical analysis above: the outer regions of the lens capture the radiation emitted at a small angle with respect to the object's surface,

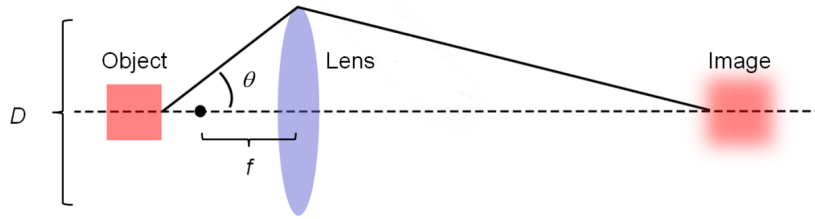


**Figure 2.0.1:** Focusing action of a lens with diameter  $D$  and focal length  $f$ . The image appears blurred, since only the propagating waves are reconstructed in the image plane.

which provides large in-plane wavenumbers and therefore contains the small sized details of a structure (see Equation 2.0.4). Note that for a given  $D$  the resolution of a lens is limited by its focal length  $f$ , since this is the minimum distance of the object at which a (real) image is formed. All in all, the performance is favored by a large diameter  $D$  and a small focal length  $f$ . However, even in the best case ( $\sin \theta \rightarrow 1$ ), structures smaller than  $\Delta_{min} \approx 0.61\lambda/n^*$  are not resolved, which reflects the absence of the object's near-field, as discussed. Note that the obtainable resolution can be improved by filling the space between object and lens with a medium of higher refractive index  $n^* > 1$  (liquid or solid immersion), which increases the numerical aperture  $NA$ .

To sum up: The diffraction limit is a consequence of the incapability of conventional optics to access the near-field region of an object, where the electric field varies on length scales smaller than the applied wavelength  $\lambda$ . This work is about entering this near-field regime, investigating *near-field superlenses* by means of *scanning near-field optical microscopy* with deep subwavelength spatial resolution.



## 3 Fundamentals I - Superlensing

*In this chapter, the phenomenon of superlensing is introduced, enabling optical imaging with a spatial resolution beyond the diffraction limit. A planar slab consisting of a negative refractive index material acts like a perfect lens, since both propagating and evanescent waves arising from an object are reconstructed. For the former, this is based on negative refraction, whereas the latter is due to an amplification process within the slab. In the electrostatic limit, negative permittivity is sufficient to enable near-field imaging of electric fields with a so-called near-field superlens. It will be shown that dissipation, which is inherent in all real materials, limits the obtainable resolution of such a superlens. The spectral behavior is described by the so called transfer function, which is the ratio of the field intensities in the object- and the image plane as a function of the radiation wavelength and the Fourier component of the field distribution on the object's surface. We also note that superlensing can be understood as the consequence of the excitation of slow surface plasmon polaritons at the superlens surface. Finally, a short overview about the experimental realization of superlenses is given, from first investigations to the here presented GaAs based system.*

### 3.1 The perfect lens

In this section, the theoretical concept of a *perfect lens* is introduced. A perfect lens is referred to be a slab that consists of a hypothetical loss-free material exhibiting simultaneously negative permittivity  $\varepsilon$  and negative permeability  $\mu$ , resulting in a negative refractive index  $n^*$ . In principle, such a material would allow for optical imaging with unlimited spatial resolution, since not only the far field but also the near field of an object is reconstructed on the other side of the lens. For simplicity, the concept is introduced by considering the surrounding medium to be air, where perfect imaging occurs if the slab exhibits  $\varepsilon = \mu = -1$  and hence  $n^* = -1$ . Note that, here and in the following,  $\varepsilon$  and  $\mu$  are considered to be the *relative* permittivity and permeability, respectively. In the static limit, where all lengths scales are significantly smaller than the applied wavelength  $\lambda$ , radiative effects can be neglected, decoupling electric and magnetic fields. It is shown

that in this case  $\varepsilon = -1$  is sufficient in order to generate such perfect images. Hence, the perfect lens concept can be applied to non-magnetic materials in this limit, which applies to doped GaAs as the material of interest in this work.

### 3.1.1 Negative refraction

The performance of a conventional lens relies on the refraction of electromagnetic radiation at its boundaries, forcing a beam to converge to a focus. This direction change depends on the change of refractive index  $n^*$  and is described by Snell's law [27]. If a beam enters medium 2 ( $n_2^*$ ) from medium 1 ( $n_1^*$ ), it is refracted according to

$$n_1^* \cdot \sin \theta_1 = n_2^* \cdot \sin \theta_2, \quad (3.1.1)$$

where  $\theta_1$  and  $\theta_2$  are the angles between the ray and the normal of the material interface. Here, same signs of the angles correspond to opposite sides of the normal. The refractive index depends on the radiation frequency  $\omega$ , causing dispersion, and fulfills the relation

$$n^*(\omega)^2 = \varepsilon(\omega)\mu(\omega), \quad (3.1.2)$$

where the wave vector  $\mathbf{k}$  inside this medium is given by

$$\mathbf{k}^2 = n^{*2} \cdot \frac{\omega^2}{c^2}. \quad (3.1.3)$$

The relative permittivity  $\varepsilon$  and the relative permeability  $\mu$  characterize the material's interaction with the electric and magnetic field component of light, respectively. For all natural materials,  $n^*$  is given by

$$n^*(\omega) = +\sqrt{\varepsilon(\omega)\mu(\omega)}. \quad (3.1.4)$$

In general,  $\varepsilon$  and  $\mu$  exhibit positive values. In such a medium, light propagates with a velocity  $c/n^*$ . In contrast, in proximity of frequencies  $\omega$  where the microscopic constituents of the medium are resonantly excited,  $\varepsilon$  (electric resonance) and  $\mu$  (magnetic resonance) change strongly as a function of  $\omega$  and can become negative valued<sup>1</sup>. Here, the charge carriers move in the opposite direction to the force caused by the respective fields. In case of one of them being negative,  $n^*$  becomes a complex quantity, making the field

<sup>1</sup>Note that in reality such resonances are always accompanied by a non-vanishing imaginary part, as can formally be seen by applying the Kramers-Kronig relations [28]. However, for a simplified theoretical approach,  $\varepsilon$  and  $\mu$  will be considered to be real in this section, as it was also assumed in Ref. [29].

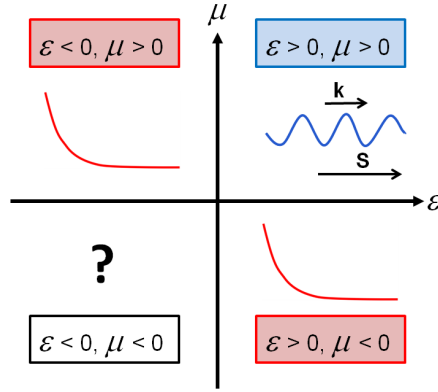


**Figure 3.1.1:** Schematic classification of materials with permittivity  $\epsilon$  and permeability  $\mu$  [30]. Values of  $\epsilon > 0$  and  $\mu > 0$  allow electromagnetic waves to propagate with the Poynting vector  $\mathbf{S}$  parallel to the wave vector  $\mathbf{k}$ . Materials with *either*  $\epsilon < 0$  or  $\mu < 0$  gives rise to evanescent decay. The case  $\epsilon < 0$  and  $\mu < 0$  is not found in nature and is discussed in this and the following section.

evanescently decay. Both sorts of such media - exhibiting *either* negative  $\epsilon$  or negative  $\mu$  - are well known, however there is no material found in nature that exhibits *both* negative  $\epsilon$  and negative  $\mu$  (see Figure 3.1.1 for an overview). Interestingly, a simultaneous sign change of  $\epsilon$  and  $\mu$  has no effect on the relations above. This issue was discussed theoretically by Veselago [29]. In the following, such a medium will be referred to as a *negative index material (NIM)*.

In order to analyze the behavior of light in a NIM,  $\epsilon$  and  $\mu$  must be considered separately, not in the form of their product. Most fundamentally, the electric field  $\mathbf{E}$ , the magnetic flux density  $\mathbf{B}$  and their associated fields  $\mathbf{D} = \epsilon\epsilon_0\mathbf{E}$  (electric displacement field) and  $\mathbf{H} = \mathbf{B}/(\mu\mu_0)$  (magnetic field) have to satisfy Maxwell's equations. These imply boundary conditions [27] at the interface between two dielectrics (no free charges or currents assumed),

$$E_{1\parallel} = E_{2\parallel}, \quad H_{1\parallel} = H_{2\parallel} \quad (3.1.5)$$

$$\epsilon_1 E_{1\perp} = \epsilon_2 E_{2\perp}, \quad \mu_1 H_{1\perp} = \mu_2 H_{2\perp}. \quad (3.1.6)$$

For simplicity,  $\epsilon_1, \mu_1 = 1$  and  $\epsilon_2, \mu_2 = -1$  are considered, representing air and a NIM, respectively. In this case, while the parallel components of  $\mathbf{E}$  and  $\mathbf{H}$  are continuous, the normal components change sign. The direction of the wave vector  $\mathbf{k}$  results from applying Faraday's and Ampere's law, respectively, assuming a plane monochromatic wave  $\propto e^{i(\mathbf{k}\mathbf{r} - \omega t)}$ :

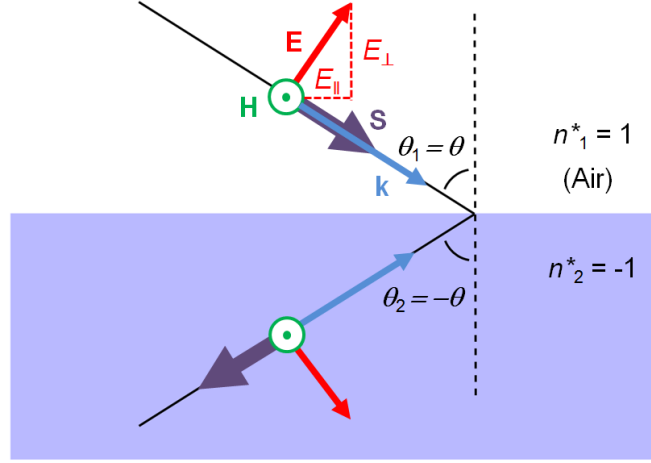


**Figure 3.1.2:** Refraction of a beam (electric field  $\mathbf{E}$ , magnetic field  $\mathbf{H}$ , wave vector  $\mathbf{k}$  and Poynting vector  $\mathbf{S}$ ) entering a NIM from free space. For the special case described here, there is no reflection (perfect impedance matching).

$$\nabla \times \mathbf{E} = -\mu\mu_0 \frac{\partial \mathbf{H}}{\partial t} \Rightarrow \mathbf{k} \times \mathbf{E} = \omega\mu\mu_0 \mathbf{H}, \quad (3.1.7)$$

$$\nabla \times \mathbf{H} = \varepsilon\varepsilon_0 \frac{\partial \mathbf{E}}{\partial t} \Rightarrow \mathbf{k} \times \mathbf{H} = -\omega\varepsilon\varepsilon_0 \mathbf{E}. \quad (3.1.8)$$

In a NIM, where  $\varepsilon < 0$  and  $\mu < 0$ , the vectors  $\mathbf{E}$ ,  $\mathbf{H}$  and  $\mathbf{k}$  form a left-handed set, which is in contrast to materials with  $\varepsilon > 0$  and  $\mu > 0$ , where they are a right-handed triplet. Hence, a NIM is also referred to as a *left-handed material*. Considering this as well as the boundary conditions given by Equations 3.1.5 and 3.1.6, light entering a NIM from free space is refracted to the same side of the surface normal, as shown in Figure 3.1.2. This is in accordance with the description by Snell's law for an interface between two media with refractive indices  $n_1^* = +1$  and  $n_2^* = -1$ . Therefore, such a behavior is referred to as *negative refraction*. With that, Equation 3.1.4 has to be extended by the special case

$$n^* = -\sqrt{\varepsilon(\omega)\mu(\omega)} \quad \text{for} \quad \varepsilon < 0 \wedge \mu < 0. \quad (3.1.9)$$

Note that the direction of the phase velocity, given by  $\mathbf{k}$ , points towards the boundary at *both* sides of the interface. This is very counterintuitive, since in the NIM the wave appears to approach the source. However, the energy flux determined by the Poynting vector

$$\mathbf{S} = \mathbf{E} \times \mathbf{H} \quad (3.1.10)$$

points away from the source, as required by causality. This allows us to complete the third

quadrant of Figure 3.1.1 by inserting Figure 3.1.3, a NIM supporting propagating waves with antiparallel  $\mathbf{k}$  and  $\mathbf{S}$ .

It is worth mentioning that, for the case described above, all energy is transferred to (and also out of) the NIM. This is because the impedances

$$Z = \sqrt{\frac{\mu\mu_0}{\varepsilon\varepsilon_0}} \quad (3.1.11)$$

of both media are equal [22]. So, besides an extraordinary refracting behavior, such a material provides full transmission of radiation passing through.

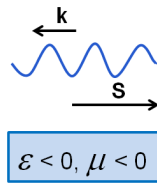


**Figure 3.1.3:** In a medium with  $\varepsilon < 0$  and  $\mu < 0$  waves propagate with  $\mathbf{k}$  and  $\mathbf{S}$  pointing in opposite directions.

### 3.1.2 Amplification of evanescent waves

The peculiar properties of a NIM can be exploited to realize a novel kind of imaging device. A planar slab performs similar to a lens, however, in contrast to a conventional one, propagating waves are focused once within the medium followed by a second reconstruction on the other side of the slab, where the image can be recorded (see Figure 3.1.4, black lines). As it was described in Chapter 2, this far field only carries spatial information of an object at a scale not smaller than the working wavelength. For a conventional lens, this is the reason for the diffraction limit. In case of a NIM lens, however, in addition to the far field, the near field (evanescent waves) is also reconstructed in the image plane, enabling imaging with subwavelength resolution. This is possible since the NIM rather *amplifies* the evanescent waves than attenuates them (see Figure 3.1.4, red line). This unique fact was theoretically discovered by Pendry [22] and will be discussed in the following.

Let us consider a ray with an electric field  $\mathbf{E} = \mathbf{E}_0 e^{ik_x x + ik_z z - i\omega t}$  arising from an object, approaching a slab of NIM ( $\varepsilon = -1$  and  $\mu = -1$ ) from free space. Per definition, the interface is the  $x$ - $y$  plane. After hitting the surface, the transmitted and reflected electric fields change their orientation with the amplitudes changing to  $tE_0$  and  $rE_0$ , respectively. Here,  $r$  and  $t$  are known as the *Fresnel coefficients* [28]. The tangential component of the wave vector,  $k_x$ , is conserved, which follows straight from the boundary conditions for  $\mathbf{E}$



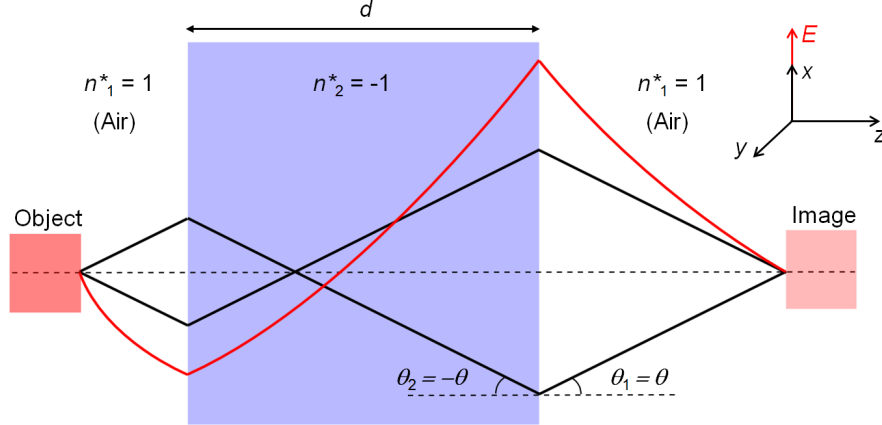


**Figure 3.1.4:** Image formation by a NIM lens, reconstructing both propagating (black) and evanescent (red) waves from an object. Note the different vertical axes for the two cases. In contrast to a conventional lens (see Figure 2.0.1) all details of the object are reconstructed in the image plane.

and  $\mathbf{H}$  (see Equations 3.1.5 and 3.1.6). The normal component  $k_z$ , on the other hand, changes sign in case of the reflected beam, whereas in transmission it is modified to  $k'_z$  as required by a change of the refractive index. Taking into account both surfaces of the slab (thickness  $d$ ), the total transmission (coefficient  $T$ ) and total reflection (coefficient  $R$ ) is calculated by considering all multiple reflections. While  $t$  and  $r$  describe the change of the electric field during the entering process, transmission and reflection of the beam exiting the slab are characterized by  $t'$  and  $r'$ . This yields<sup>2</sup>

$$T = tt'e^{ik'_z d} + tt'r'^2 e^{3ik'_z d} + tt'r'^4 e^{5ik'_z d} + \dots = \frac{tt'e^{ik'_z d}}{1 - r'^2 e^{2ik'_z d}}, \quad (3.1.12)$$

$$R = r + r'e^{ik'_z d}(tt'e^{ik'_z d} + tt'r'^2 e^{3ik'_z d} + tt'r'^4 e^{5ik'_z d}) + \dots = r + \frac{r'tt'e^{2ik'_z d}}{1 - r'^2 e^{2ik'_z d}}. \quad (3.1.13)$$

In the following  $T$  and  $R$  are calculated, where the fractions of the beam transmitted through and reflected by the slab exhibit electric-field amplitudes  $TE_0$  and  $RE_0$ , respectively. Since the properties of an electromagnetic wave at an interface depend on its polarization, two cases are discussed separately. On the one hand p-polarized waves, where the electric-field vector  $\mathbf{E}^P$  lies in the plane of incidence, defined by the surface normal and the incident propagation vector  $\mathbf{k}$ . On the other hand s-polarized waves, where the electric-field vector  $\mathbf{E}^S$  is perpendicular to the plane of incidence. The general case is a superposition of these two special cases.

<sup>2</sup>Convergence of a geometric series  $\sum_{k=0}^{\infty} a_0 q^k = \frac{a_0}{1-q}$ , considering that  $|r'| < 1$ .

### p-Polarization

For p-polarized light, the Fresnel coefficients  $t$  and  $r$  at the first interface are given by [22]

$$t = \frac{2\varepsilon k_z}{\varepsilon k_z + k'_z}, \quad r = \frac{\varepsilon k_z - k'_z}{\varepsilon k_z + k'_z}. \quad (3.1.14)$$

Conversely, the transmitted part experiences transmission and reflection at the other surface according to

$$t' = \frac{2k'_z}{k'_z + \varepsilon k_z}, \quad r' = \frac{k'_z - \varepsilon k_z}{k'_z + \varepsilon k_z}. \quad (3.1.15)$$

Here, the refractive index of free space is already considered, whereas  $\varepsilon = -1$  for the NIM is inserted later. Note that, usually, the Fresnel coefficients are given as a function of the incidence angle  $\theta_1$  and transmission angle  $\theta_2$ . Here,  $\cos \theta_i = (k_{z,i}c)/(n_i^*\omega)$  yields Equations 3.1.14 and 3.1.15.

For a propagating wave entering a NIM with  $\varepsilon = -1$  and  $\mu = -1$  it was already shown in the previous section that  $k'_z = -k_z$ , which yields  $t = 1, t' = 1$  and  $r = 0, r' = 0$ . This corresponds to full transmission both into and out of the NIM without any reflection, which is in accordance with the already mentioned perfect match of impedances (see Equation 3.1.11). In case of evanescent waves, however, the argumentation resulting in  $k'_z = -k_z$  does not hold, since it was based on a discussion about the direction of  $\mathbf{k}$ , which is invalid for imaginary  $k_z$  (i.e. evanescent waves). As we saw in Chapter 2, this applies to large tangential wavenumbers  $k_x$  and  $k_y$ ,

$$k_z = +i\sqrt{k_x^2 + k_y^2 - \frac{\omega^2}{c^2}} \quad \text{with} \quad \frac{\omega^2}{c^2} < k_x^2 + k_y^2, \quad (3.1.16)$$

corresponding to an exponential decay away from the object. For the transmitted part of such a wave entering a NIM, causality requires further decay away from the surface, so

$$k'_z = +i\sqrt{k_x^2 + k_y^2 - \varepsilon\mu\frac{\omega^2}{c^2}}, \quad \text{with} \quad \varepsilon\mu\frac{\omega^2}{c^2} < k_x^2 + k_y^2. \quad (3.1.17)$$

Substituting  $\varepsilon, \mu = -1$  yields  $k'_z = k_z$ , causing  $t, t', r$  and  $r'$  to diverge to infinity. To obtain a meaningful result, one has to consider the total process according to Equations 3.1.12 and 3.1.13. Since  $t, t', r$  and  $r'$  all diverge at an equal rate with different signs,  $T^P$  and  $R^P$

converge. Hence we obtain

$$\lim_{\substack{\varepsilon \rightarrow -1 \\ \mu \rightarrow -1}} T^{\text{P}} = \lim_{\substack{\varepsilon \rightarrow -1 \\ \mu \rightarrow -1}} \frac{tt'e^{ik'_z d}}{1 - r'^2 e^{2ik'_z d}} = e^{-ik'_z d} = e^{-ik_z d} = e^{+\tilde{k}_z d}, \quad (3.1.18)$$

$$\lim_{\substack{\varepsilon \rightarrow -1 \\ \mu \rightarrow -1}} R^{\text{P}} = \lim_{\substack{\varepsilon \rightarrow -1 \\ \mu \rightarrow -1}} \left( r + \frac{r'tt'e^{2ik'_z d}}{1 - r'^2 e^{2ik'_z d}} \right) = 0. \quad (3.1.19)$$

Therefore, even though presuming exponential decay after entering the NIM, the wave is exponentially *amplified* through the slab. Note that, as already introduced in Chapter 2,  $\tilde{k}_z$  is a positive real number.

### s-Polarization

For s-polarized light, we get

$$t = \frac{2\mu k_z}{\mu k_z + k'_z}, \quad r = \frac{\mu k_z - k'_z}{\mu k_z + k'_z}, \quad (3.1.20)$$

and

$$t' = \frac{2k'_z}{k'_z + \mu k_z}, \quad r' = \frac{k'_z - \mu k_z}{k'_z + \mu k_z}. \quad (3.1.21)$$

Same considerations as in the case of p-polarized radiation reveal vanishing reflection of propagating waves ( $k'_z = -k_z$ ) and amplified transmission of evanescent waves ( $k_z = k'_z$  with both being imaginary numbers), where the latter yields

$$\lim_{\substack{\varepsilon \rightarrow -1 \\ \mu \rightarrow -1}} T^{\text{S}} = e^{-ik'_z d} = e^{-ik_z d} = e^{+\tilde{k}_z d}, \quad (3.1.22)$$

$$\lim_{\substack{\varepsilon \rightarrow -1 \\ \mu \rightarrow -1}} R^{\text{S}} = 0. \quad (3.1.23)$$

In conclusion, it was shown both for p- and for s-polarized light, and hence for arbitrary polarization, that a NIM with negative refractive index  $n^* = -1$  and moreover  $\varepsilon, \mu = -1$  is capable of focusing an object's far field and compensating the decay of its near field, resulting in an image formation with unlimited resolution. In literature, this is referred to as a *perfect lens*. Here, note that not only  $n^*$  but also  $\varepsilon$  and  $\mu$  have to match the corresponding values of the surrounding medium with opposite signs.

Interestingly, in a specific case it is sufficient if *either*  $\varepsilon$  or  $\mu$  is negative in order to obtain such a perfect image. This is the subject of the following section.

### 3.1.3 Static limit

In the previous sections, we analyzed how propagating and evanescent waves behave in a NIM, concluding that the NIM can act as a perfect lens. If all dimensions are much smaller than the wavelength, radiative effects can be neglected. Here, magnetic and electric fields are decoupled, entering the regime of electro- and magnetostatics [22]. In this limit

$$\frac{\omega}{c} \ll \sqrt{k_x^2 + k_y^2}. \quad (3.1.24)$$

The wave vector of an evanescent wave arising from the object (see Equation 3.1.16) can then be approximated by

$$\lim_{k_x^2 + k_y^2 \rightarrow \infty} k_z = \lim_{k_x^2 + k_y^2 \rightarrow \infty} i \sqrt{k_x^2 + k_y^2 - \frac{\omega^2}{c^2}} = i \sqrt{k_x^2 + k_y^2}, \quad (3.1.25)$$

where for the part transmitted into the NIM (see Equation 3.1.17) we obtain

$$\lim_{k_x^2 + k_y^2 \rightarrow \infty} k'_z = \lim_{k_x^2 + k_y^2 \rightarrow \infty} i \sqrt{k_x^2 + k_y^2 - \varepsilon \mu \frac{\omega^2}{c^2}} = i \sqrt{k_x^2 + k_y^2} = k_z. \quad (3.1.26)$$

Note that in the static limit, not only the structures to be imaged, but also the thickness  $d$  is set to be much smaller than the wavelength  $\lambda$ , where the latter corresponds to the assumption that the speed of light  $c$  is infinite. Here, deviations from  $d \ll \lambda$  result in retardation effects [31], making the lens no longer perfect.

In contrast to the general considerations, where  $\varepsilon = \mu = -1$  yields  $k'_z = k_z$ , the latter is valid independently of both  $\varepsilon$  and  $\mu$  in the static limit. In this case, inserting Equations 3.1.14, 3.1.15, 3.1.20 and 3.1.21 into Equations 3.1.12 and 3.1.13 reveals that reflection and transmission of p-polarized light just depends on  $\varepsilon$ , while  $\mu$  is the relevant parameter for s-polarized radiation. The transmission- and reflection coefficients  $T$  and  $R$ , respectively, are calculated as follows.

**p-Polarization**

$$\lim_{\varepsilon \rightarrow -1} \left( \lim_{k_x^2 + k_y^2 \rightarrow \infty} T^P \right) = \lim_{\varepsilon \rightarrow -1} \frac{4\varepsilon e^{ik_z d}}{(\varepsilon + 1)^2 - (\varepsilon - 1)^2 e^{2ik_z d}} = e^{-ik_z d} = e^{+\tilde{k}_z d} \quad (3.1.27)$$

$$\lim_{\varepsilon \rightarrow -1} \left( \lim_{k_x^2 + k_y^2 \rightarrow \infty} R^P \right) = \lim_{\varepsilon \rightarrow -1} \left( \frac{\varepsilon - 1}{\varepsilon + 1} + \frac{1 - \varepsilon}{1 + \varepsilon} \frac{4\varepsilon e^{2ik_z d}}{(\varepsilon + 1)^2 - (\varepsilon - 1)^2 e^{2ik_z d}} \right) = 0 \quad (3.1.28)$$

**s-Polarization**

$$\lim_{\mu \rightarrow -1} \left( \lim_{k_x^2 + k_y^2 \rightarrow \infty} T^S \right) = \lim_{\mu \rightarrow -1} \frac{4\mu e^{ik_z d}}{(\mu + 1)^2 - (\mu - 1)^2 e^{2ik_z d}} = e^{-ik_z d} = e^{+\tilde{k}_z d} \quad (3.1.29)$$

$$\lim_{\mu \rightarrow -1} \left( \lim_{k_x^2 + k_y^2 \rightarrow \infty} R^S \right) = \lim_{\mu \rightarrow -1} \left( \frac{\mu - 1}{\mu + 1} + \frac{1 - \mu}{1 + \mu} \frac{4\mu e^{2ik_z d}}{(\mu + 1)^2 - (\mu - 1)^2 e^{2ik_z d}} \right) = 0 \quad (3.1.30)$$

In the static limit, amplification of evanescent waves solely requires  $\varepsilon = -1$  or  $\mu = -1$ , depending on the polarization of the incident beam. While dielectric activity is required for p-polarized light, magnetic resonances enable perfect imaging for s-polarized radiation.

## 3.2 The superlens

In this section, limitations imposed by real materials are taken into account, giving rise to the term *superlens* as the practical realization of the perfect lens concept. We discuss why there is only application potential in the static limit and show that the obtainable spatial resolution of such a superlens operating in the near-field region is limited by losses and favored by a surrounding medium of large permittivity. Finally, the so called transfer function is introduced, which simulates the imaging performance of a superlens.

### 3.2.1 Practical limitations

A material exhibiting  $\varepsilon < 0$  and  $\mu < 0$  at the same time, which is the requirement for negative refraction and hence for the perfect lens, is not found in nature. This is due to the fact that dielectric and magnetic resonances occur at distinctly separated radiation frequencies, the latter typically dissipating above 100 GHz [32]. However, negative refraction can be achieved by artificially engineered metamaterials, as we will further discuss in Section 3.4. Nevertheless, due to losses, a far-field application as a lens with subwavelength spatial res-

olution is not promising [24, 33]. The discussion so far was based on the assumption of  $\varepsilon$  and  $\mu$  being real negative quantities, which is convenient for understanding the concept of a perfect lens. In reality, however, dissipation has to be considered, giving rise to complex values of  $\varepsilon = \varepsilon' + i\varepsilon''$  and  $\mu = \mu' + i\mu''$  with non negligible imaginary parts. Such a system, which takes into account this limitation, is referred to as a *superlens*. It was shown [24] that, even if the losses are considered to be very small, resolution improvement in comparison to conventional optics can just be obtained if the distance  $2d$  between object and image ( $d$  is the thickness of the lens, see Figure 3.1.4) is in the order of the wavelength  $\lambda$ .

### 3.2.2 Obtainable resolution of a near-field superlens

The concept of superlenses is impacted by both the feasibility of metamaterials exhibiting negative refraction, which is a highly nontrivial issue especially at optical wavelengths [34], and by unavoidably inherent losses, hindering any far-field application. Both issues can be overcome in the static limit ( $d \ll \lambda$ , see Section 3.1.3), where subwavelength resolution can be obtained if either  $\varepsilon < 0$  or  $\mu < 0$ , rather than  $n^* < 0$ . Being restricted to the near-field region, such a device is called a *near-field superlens*. Since  $\varepsilon_- < 0$  accompanied by  $\mu = 1$  (non-magnetic material) is very common (e.g. noble metals at optical frequencies or doped semiconductors in the infrared), we will restrict ourselves to this case, confining our attention to p-polarized light. Here, the index "-" was added to the permittivity  $\varepsilon_-$  of the superlens layer for clarity, indicating its negative value. In the static limit, structure sizes ( $x$ - $y$  plane) much smaller than  $\lambda$  correspond to large tangential wavenumbers

$$k_t = \sqrt{k_x^2 + k_y^2} \gg \frac{\omega}{c}, \quad (3.2.1)$$

resulting in imaginary values of  $k_z$ . Hence the electric field  $E_0$  of a structure at a distance  $d/2$  from the superlens decays evanescently according to  $e^{-k_t d/2}$  on the way to the slab, where  $k_t = -ik_z$  (see Equation 3.1.25). As we discussed in Section 3.1.3, a superlens with thickness  $d$  and  $\varepsilon_- = -1$  compensates this decay via exponential amplification of transmission  $T^P = e^{+k_t d}$ . Neglecting losses, the original amplitude  $E_0$  is finally obtained again at a distance  $d/2$  on the other side of the slab, which is therefore the image plane of the superlens (see Figure 3.2.1a). Here,  $T^P$  is given by [22]

$$T^P = \frac{4\varepsilon_- e^{-k_t d}}{(\varepsilon_- + 1)^2 - (\varepsilon_- - 1)^2 e^{-2k_t d}} \quad (3.2.2)$$

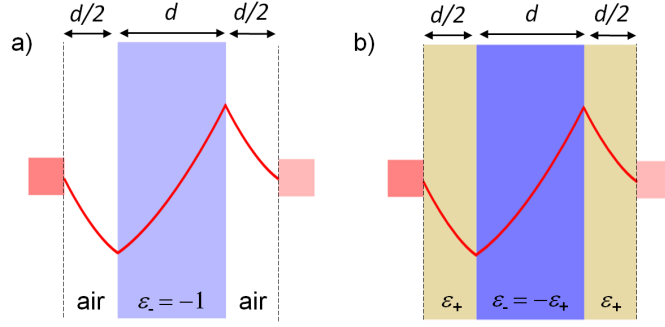


**Figure 3.2.1:** (a) Superlens suspended in air, where the resonance condition is  $\epsilon_- = -1$ . Object plane and image plane, indicated by dashed lines, are at a distance  $2d$ , where  $d$  is the thickness of the superlens. The symmetric case depicted here is a special case. (b) If the surrounding medium is a dielectric of permittivity  $\epsilon_+$  the superlens condition changes to  $\epsilon_- = -\epsilon_+$ . In both cases, reconstruction of evanescent waves (red line) is obtained in the image plane.

(see Equation 3.1.27). Any deviation from  $\epsilon_- = -1$  will degrade the amplifying effect of the superlens. In particular, as mentioned, the superlensing condition is  $\epsilon_- = -1 + i\epsilon_-''$  with  $\epsilon_-'' > 0$  for a realistic, lossy system. In case of small losses according to  $\epsilon_-'' \ll 1$ , we can approximate [35]

$$T^P \approx \frac{e^{-k_t d}}{\frac{1}{4}(\epsilon_-'')^2 + e^{-2k_t d}}. \quad (3.2.3)$$

The amplifying power is significantly suppressed when

$$\frac{\epsilon_-''^2}{4} > e^{-2k_t d}, \quad (3.2.4)$$

resulting in a limited resolution where structures smaller than

$$\Delta = \frac{-2\pi d}{\ln\left(\frac{\epsilon_-''}{2}\right)} \quad (3.2.5)$$

cannot be resolved. Here,  $\Delta = 2\pi/k_t$  was applied (see Equation 2.0.4). This is the resolution limit of a low-loss near-field superlens suspended in air [35].

In the experiment, such a system as depicted in Figure 3.2.1a obviously cannot be realized, since it would require a layer of subwavelength thickness to float in air above an object to be imaged. On the other hand, superlensing has been demonstrated a number of times by sandwiching the superlens layer between dielectric layers of positive permittivity  $\epsilon_+$  [36, 37, 38] (see Figure 3.2.1b). As a beneficial side effect, for given losses,  $\epsilon_+ > 1$  comes

with an increase of obtainable resolution as compared to air being the surrounding medium [35, 39]. While all calculations so far have been carried out for this case, i.e.  $\varepsilon_+ = 1$ , the resonance condition for a superlens layer of permittivity  $\varepsilon_-$  surrounded by a medium with dielectric constant  $\varepsilon_+$  is given by

$$\varepsilon_- = -\varepsilon_+. \quad (3.2.6)$$

Considering losses giving rise to complex valued permittivities, i.e.  $\varepsilon_- = \varepsilon'_- + i\varepsilon''_-$  and  $\varepsilon_+ = \varepsilon'_+ + i\varepsilon''_+$ , the best resolution is obtained if

$$\varepsilon'_- = -\varepsilon'_+. \quad (3.2.7)$$

In practice, dissipation in the surrounding medium can usually be neglected, hence we assume that  $\varepsilon''_+ \approx 0$ . With absorption within the superlens also being small,  $\varepsilon''_- \ll |\varepsilon'_-|$ , the transmission coefficient  $T^P$  through one layer of thickness  $d$  is given by

$$T^P \approx \frac{\varepsilon'^2_- e^{-k_t d}}{\frac{1}{4}(\varepsilon''_-)^2 + \varepsilon'^2_- e^{-2k_t d}}, \quad (3.2.8)$$

corresponding to a resolution limit of [40]

$$\Delta = \frac{-2\pi d}{\ln\left(\frac{\varepsilon''_-}{-2\varepsilon'_-}\right)}. \quad (3.2.9)$$

This shows that the ratio  $\varepsilon''_-/\varepsilon'_-$  limits the performance. Comparing this to the obtainable resolution of a superlens surrounded by air (see Equation 3.2.5), the large value of  $\varepsilon'_+ = -\varepsilon'_-$  reduces the impact of the dissipation  $\varepsilon''_-$ , resulting in a smaller observable structure size  $\Delta$ . In Ref. [35], the transmission through a stack of silver and GaAs layers was simulated, exhibiting permittivities of  $\varepsilon_- = -12 + 0.4i$  and  $\varepsilon_+ = 12$ , respectively, at a radiation wavelength of  $\lambda = 578$  nm. Here, the performance was found<sup>3</sup> to be indeed much better than when replacing GaAs by air (considering a shifted resonance wavelength of  $\lambda = 365$  nm, where  $\varepsilon_- = -1 + 0.4i$ ). Despite providing interesting insights, these simulations lack experimental feasibility, since a layer system of GaAs and silver (not to mention air and silver) with well defined thicknesses on the nanometer scale can hardly be fabricated. In contrast, a similar system can be readily obtained by replacing silver with doped GaAs, which provides negative permittivity in the infrared spectral region.

---

<sup>3</sup>For these hypothetical considerations, the authors of Ref. [35] neglected absorption across the band gap of GaAs at this wavelength. This dissipation results in a non-vanishing imaginary part of  $\varepsilon_+$ , i.e.  $\varepsilon_+(\lambda = 578 \text{ nm}) \approx 12 + 2i$  [41], imposing additional limitations to the performance of a real GaAs-silver superlens.



It is the goal of this work to discuss and experimentally evidence whether such kind of superlens is capable to provide enhancement of evanescent waves and hence imaging with subwavelength resolution.

### 3.2.3 Transfer function

In this section, the so called *transfer function*  $|T_{\text{SL}}|^2$  of a near-field superlens is introduced, which will be applied in Section 8.1 in order to simulate the performance of the superlens sample to be investigated. Here,  $T_{\text{SL}}$  is the ratio between the electric fields  $E_{\text{image}}$  in the image plane and  $E_0$  emitted by the object to be imaged, i.e.

$$T_{\text{SL}} = \frac{E_{\text{image}}}{E_0}. \quad (3.2.10)$$

Hence,  $|T_{\text{SL}}|^2$  describes the intensity change regarding the imaging process, where phase effects can be neglected in the near-field limit. For the hypothetical perfect lens,  $|T_{\text{SL}}|^2$  is equal to 1 for all emitted wave vectors, providing an image with unlimited resolution. Throughout this thesis, the transfer function will refer to p-polarized light, which is the requirement for near-field superlensing with a non-magnetic material (see Section 3.1.3). Here, please note the difference between  $T_{\text{SL}}$  and  $T^{\text{P}}$ , where the latter describes the transmission through the superlens layer only, as discussed in the previous sections. Denoting the field change from object to superlens and from superlens to image as  $T_{\text{in}}$  and  $T_{\text{out}}$ , respectively,  $T_{\text{SL}}$  is given by

$$T_{\text{SL}} = T_{\text{in}} T^{\text{P}} T_{\text{out}} \quad (3.2.11)$$

For the near-field superlens suspended in air with the object at a distance  $d/2$ , as depicted in Figure 3.2.1a, this results in

$$T_{\text{SL}} = e^{-k_t d/2} \frac{4\varepsilon_- e^{-k_t d}}{(\varepsilon_- + 1)^2 - (\varepsilon_- - 1)^2 e^{-2k_t d}} e^{-k_t d/2}, \quad (3.2.12)$$

where  $k_t$  is the tangential wavenumber of the emitted light (see Equations 3.2.1 and 3.2.2). Thus, a perfect field reconstruction is obtained if  $\varepsilon_- = -1$ , since for all  $k_t$  we get  $T_{\text{SL}} = 1$  and hence  $|T_{\text{SL}}|^2 = 1$ . As discussed in Section 3.2.2, unavoidable loss prevents achieving this efficiency in practical systems.

In this work, a superlens consisting of a doped GaAs layer (thickness  $d$ ) sandwiched between two intrinsic layers (thickness  $d/2$ ) is investigated, where object- and image plane coincide with the outer surfaces of the intrinsic layers. Therefore, in order to obtain  $T_{\text{SL}}$ ,

one has to consider as well multiple reflections at these two interfaces. On the image side, the structure borders on air, where the transmitted field is measured, and on the object side, due to the sample preparation procedure (see Section 6.1), there is glue of unknown permittivity. Due to this uncertainty, the superlens is assumed in the calculations to be adjacent to air on both sides. In the following, we will discuss qualitatively how to calculate the transfer function of such a trilayer structure.

We denote  $t_{ij}$  and  $r_{ij}$  as the transmission and reflection Fresnel coefficient, respectively, for a wave entering medium  $j$  ( $\varepsilon_j$ ) from medium  $i$  ( $\varepsilon_i$ ). With  $k_t$  being continuous, the normal component of the wave vector  $\mathbf{k}$  changes from  $k_{z,i} = \sqrt{\varepsilon_i(\omega/c)^2 - k_t^2}$  to  $k_{z,j} = \sqrt{\varepsilon_j(\omega/c)^2 - k_t^2}$ . For a layer  $m$  (thickness  $d$ ) adjacent to medium  $l$  on the incident side and medium  $n$  on the other side,  $t_{ln}$  and  $r_{ln}$  describe the transmission through and reflection by the slab, respectively, and are given by<sup>4</sup>

$$t_{ln} = \frac{t_{lm}t_{mn}e^{ik_{z,m}d}}{1 - r_{mn}r_{ml}e^{2ik_{z,m}d}}, \quad (3.2.13)$$

$$r_{ln} = r_{lm} + \frac{r_{mn}t_{lm}t_{ml}e^{2ik_{z,m}d}}{1 - r_{mn}r_{ml}e^{2ik_{z,m}d}}. \quad (3.2.14)$$

This was already discussed in detail in Section 3.1.2 for the special case of the surrounding medium of the layer being air on both sides [22].

The system representing the superlens sample realized in the experimental part of this thesis, as described above, is shown in Figure 3.2.2, being a three-layered structure suspended in air according to an effective five layer system. The calculation of  $T_{\text{SL}}$  comprises the following steps: Denoting the layers, including the surrounding air, as 1-5 counting from the incident side, layers 3-5 are treated first to obtain  $t_{35}$  and  $r_{35}$  by applying Equations 3.2.13 and 3.2.14. After that, layer 2 is taken into consideration for  $t_{25}$  and  $r_{25}$ , where Equations 3.2.13 and 3.2.14 are repeated with  $t_{35}$  and  $r_{35}$  accounting for the overall transmission- and reflection properties of layer 4. Finally,  $t_{15}$  and  $r_{15}$  is obtained by adding layer 1. This procedure is indicated schematically in Figure 3.2.2. With  $\varepsilon_2 = \varepsilon_4 := \varepsilon_+$  and  $\varepsilon_3 := \varepsilon_-$ , the condition for superlensing is  $\varepsilon_- = -\varepsilon_+$ . As mentioned, the object and image plane coincide with the two surfaces adjacent to air, hence

$$T_{\text{SL}} = t_{15}, \quad (3.2.15)$$

implying that, in this case, the transfer function  $|T_{\text{SL}}|^2$  equals the *transmittance* through

---

<sup>4</sup>Please note the agreement with the expressions found in Ref. [27], taking into account that  $r_{12} = -r_{21}$  and  $r_{12}^2 + t_{12}t_{21} = 1$ .

the three-layered superlens structure. In particular, this applies to the calculated transfer function of the superlens sample presented in Section 8.1. Finally, note that for a given material system, the transfer function is a function of  $k_t$  and the free-space wavelength  $\lambda$ ,

$$|T_{\text{SL}}|^2 = |T_{\text{SL}}|^2(k_t, \lambda), \quad (3.2.16)$$

since  $\lambda$  determines the permittivities  $\varepsilon_i$  of the contributing layers and  $k_t$  sets the direction of the incoming beam. It is worth emphasizing that large values of the transfer function at large  $k_t$  correspond to high spatial resolution, since high order Fourier components of the object's electric field are reconstructed in the image.

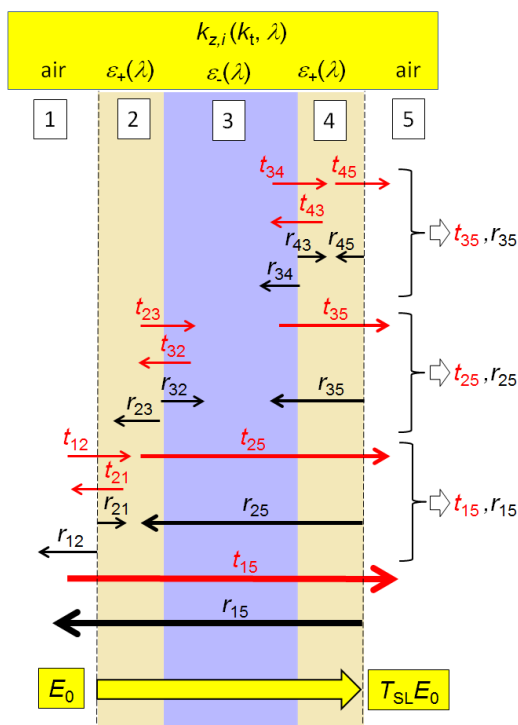


**Figure 3.2.2:** Sketch regarding the calculation of the transfer function  $|T_{\text{SL}}|^2$  of a tri-layer system representing the superlens sample realized in the experiment. The electric field  $E_0$  emitted by an object is modified to  $T_{\text{SL}}E_0$  by the imaging process, where the calculation of  $T_{\text{SL}}$  involves multiple transmissions  $t_{ij}$  and reflections  $r_{ij}$  at all contributing boundaries. Object and image plane at a distance  $2d$  are indicated by black dashed lines, where  $d$  is the thickness of the middle layer (blue) exhibiting negative permittivity  $\varepsilon_-$ .

### 3.3 A different point of view: Plasmonics

So far, near-field superlensing has been explained through enhanced transmission of evanescent waves. However, there is another interpretation of this phenomenon. It was introduced in Section 3.2.2 that a planar slab of negative permittivity  $\varepsilon_-$  embedded in a medium of positive permittivity  $\varepsilon_+$  acts as a superlens if

$$\varepsilon_- = -\varepsilon_+. \quad (3.3.1)$$

This is also the condition for the existence of slow surface plasmon polaritons [42] at a metal-dielectric interface, which will be discussed in the following.

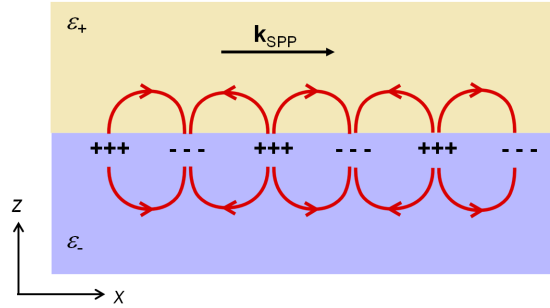


**Figure 3.3.1:** Illustration of the combined character of a surface plasmon polariton (SPP) with wave vector  $\mathbf{k}_{\text{SPP}}$ . Charge oscillations at the surface of an electric conductor ( $\varepsilon_-$ ) bordering on a dielectric ( $\varepsilon_+$ ) are accompanied by electromagnetic waves (red arrows indicate the electric field component).

Surface plasmons are quanta of plasma oscillations, i.e. oscillations of the free electron density, localized at the interface between a dielectric ( $\varepsilon_+ > 0$ ) and an electric conductor ( $\varepsilon_- < 0$ ). Being always accompanied by electromagnetic oscillations, a quasiparticle called surface plasmon polariton (SPP) is introduced that consists of the plasmon and its surrounding electromagnetic field. Here, the electric component contributes both longitudinal and transversal fields (see Figure 3.3.1), classified as transverse magnetic (TM) modes which can be excited by p-polarized light only. With  $x$  and  $z$  being the directions of SPP propagation and surface normal, respectively, the electric field can be written as [42, 43]

$$\mathbf{E}_j = [E_x^j, 0, E_z^j] e^{i(k_{\text{SPP}}x - \omega t)} e^{-\alpha_j |z|}. \quad (3.3.2)$$

Here,  $j = +$  for the dielectric and  $j = -$  for the conductor. This is a wave propagating in  $x$ -direction and decaying exponentially in  $z$ -direction. The wavenumber  $k_{\text{SPP}}$  and the inverse penetration depth  $\alpha_j$  follow from the boundary conditions (Equations 3.1.5 and 3.1.6) for the components of  $\mathbf{E}_j$  and the associated magnetic field  $\mathbf{H}_j$ . Thus, the SPP

dispersion relation  $k_{\text{SPP}}(\omega)$  is given by

$$k_{\text{SPP}} = \frac{\omega}{c} \sqrt{\frac{\varepsilon_-(\omega)\varepsilon_+}{\varepsilon_-(\omega) + \varepsilon_+}}, \quad (3.3.3)$$

where it is assumed that  $\varepsilon_+$  is constant. The results for  $\alpha_j$  are not shown here but are, for instance, given in Refs. [42, 43]. For a qualitative discussion here, the metallic dielectric function  $\varepsilon_-(\omega)$  is approximated by applying the model system of a free electron gas [44] with no attenuation, providing<sup>5</sup>

$$\varepsilon_- = 1 - \left(\frac{\omega_p}{\omega}\right)^2, \quad (3.3.4)$$

with the plasma frequency

$$\omega_p = \sqrt{\frac{ne^2}{m^*\varepsilon_0}}. \quad (3.3.5)$$

Here,  $n$  is the electron density,  $e$  the elementary electric charge,  $m^*$  the effective mass of an electron and  $\varepsilon_0$  the permittivity of vacuum. The resulting SPP dispersion is depicted in Figure 3.3.2. For small radiation frequencies  $\omega \ll \omega_p$ ,  $\varepsilon_-$  exhibits large negative values, so in this limit

$$\lim_{\omega \rightarrow 0} k_{\text{SPP}} = \frac{\omega}{c_+}, \quad (3.3.6)$$

where  $c_+ = c/\sqrt{\varepsilon_+}$  is the speed of light in the dielectric. On the other hand,  $k_{\text{SPP}}$  goes to infinity when  $\varepsilon_-$  approaches  $-\varepsilon_+$ , which is the case for

$$\omega_{\text{SPP}} = \omega_p \sqrt{\frac{1}{1 + \varepsilon_+}}. \quad (3.3.7)$$

Here, the phase velocity  $v_{\text{SPP}} = \omega/k_{\text{SPP}}$  of the SPPs goes to zero for an excitation frequency  $\omega_{\text{SPP}}$  which satisfies the superlensing condition given by Equation 3.3.1. Hence, the superlensing effect can be regarded as the consequence of slowing of light at metallic surfaces [45], providing near-field imaging through a thin conducting layer without any blurring<sup>6</sup>. Here, the large tangential wavenumbers  $k_t$  of an object's electric field, which

<sup>5</sup>In Section 5.2 the infrared permittivity of doped GaAs, which is relevant for this work, will be introduced (see Equation 5.2.6). Note that this is in accordance with Equations 3.3.4 and 3.3.5 when taking into account the background permittivity  $\varepsilon_{\text{optic}}$  at high frequencies, electron damping  $\gamma_{\text{el}}$  and the presence of lattice vibrations (phonons).

<sup>6</sup>Later in this thesis, at some points, these slow SPPs at superlensing conditions will be referred to as *localized* polaritons, however, please be aware that the term localized surface plasmon (LSP) in literature usually denotes plasmons confined to metallic nanoparticles.

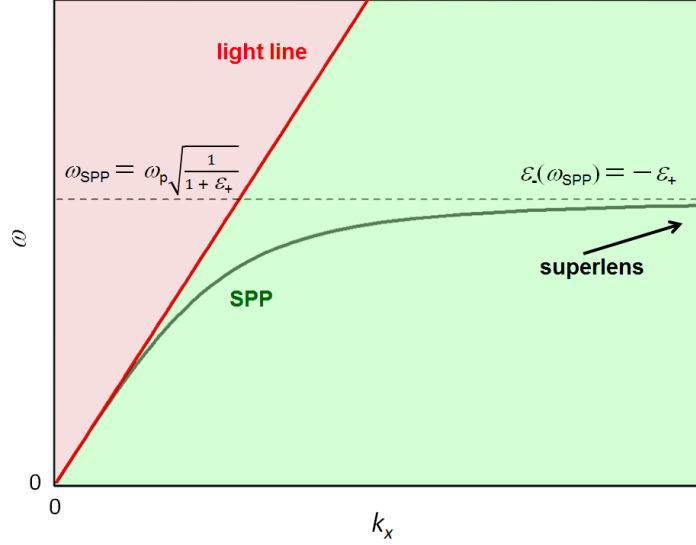


**Figure 3.3.2:** Dispersion of an electromagnetic wave within a dielectric of permittivity  $\varepsilon_+$  (red line; the slope is  $c_+ = c/\sqrt{\varepsilon_+}$ ) and of a SPP, i.e.  $k_{\text{SPP}}(\omega)$ , at the interface with an adjacent conductor (dielectric function  $\varepsilon_-$ ), both propagating in  $x$ -direction. The red and the green areas correspond to the regions of propagating (arbitrary direction) and evanescent waves in the dielectric, respectively. The superlensing condition corresponds to  $\omega = \omega_{\text{SPP}}$ .

have to be supported by the superlens in order to enable subwavelength spatial resolution (see previous sections), correspond to the large values of  $k_{\text{SPP}}$ .

The field distribution at superlensing condition is depicted in Figure 3.2.1, illustrating that the field is amplified at the image side of the superlens surface, whereas it is small at the object side. Note that the latter corresponds to an *anti-plasmon* state that cannot exist in isolation [46], since the field would diverge exponentially. However, for a thin superlens slab it couples with the SPP on the other side, resulting in enhanced near-field transmission.

As can be seen in Figure 3.3.2, the phase velocity of SPPs is always lower than of propagating light in the dielectric, the latter being represented by the red area in the figure (note that light cannot propagate in the conductor). Due to this momentum mismatch, generally, SPPs are not excited by light in a sample of the geometry depicted in Figure 3.3.1. However, tangential wavenumbers larger than  $\omega/c_+$  can be provided by evanescent waves (green area in Figure 3.3.2), as we have discussed in detail previously in this chapter. A standard way to excite SPPs via evanescent waves is attenuated total reflection (ATR) using a prism [43]. For the superlens investigations in this work, on the other hand, these evanescent fields are primarily generated at the probe apex of a near-field optical micro-

scope (see Section 4), which therefore not only measures but also initiates the superlensing effect. Here, a probe with curvature radius  $a$  provides wavenumbers in the order of  $1/a$  [47], which is far beyond  $\omega/c_+$  in our experiments, where a tip with  $a \approx 50$  nm probes near fields at mid-infrared frequencies.

In the present work a plasmonic superlens based on doped GaAs is investigated, however the superlensing effect is not limited to metallic materials. The required negative permittivity may also result from phonon resonances, giving rise to superlensing in electrically isolating media [36, 37, 38]. Here, in analogy to the considerations in the present section, near-field imaging is provided by *surface phonon polaritons* instead of SPPs.

### 3.4 From first experiments to the GaAs superlens

Ever since Pendry theoretically demonstrated in 2000 [22] that materials with negative refractive index  $n^* < 0$  (negative index materials, NIMs) [29] promise optical imaging beyond the diffraction limit (see Section 3.1.2), there has been a lot of experimental activity in order to realize such a *superlens*. One major drawback of this idea is the fact that a NIM requires strong electric and magnetic activity at the same time (see Section 3.1.1), which is not found in nature. However, negative  $n^*$  can be achieved with artificial media that consist of periodic microstructure arrays. Here, typical length scales are much smaller than the working wavelength  $\lambda$ , so that the wave cannot resolve the individual constituents. This is referred to as a *metamaterial* [30].

It was Pendry himself who suggested, even before his perfect lens (the idealized analog to the superlens) proposal, that thin wires and "split ring" resonators made out of metal allow for independent control of the electric [48, 49] and magnetic [50] response, respectively. By choosing the right shapes and dimensions of these structures, both  $\epsilon$  and  $\mu$  become negative at the same desired frequency, giving rise to negative refraction. Following Pendry's idea, the first NIM was demonstrated at microwave frequencies [51, 52]. Shortly after, the creation of an image inside the NIM, which is a characteristic feature of this kind of lens (see Figure 3.1.4), was observed in the same spectral region [53]. Here, instead of split rings and wires, the metamaterial was made of a planar transmission line network, periodically implemented by inductors and capacitors. Despite having proven the imaging capability of a NIM, however, this did not yet verify the superlens concept. As introduced in Section 3.1.2, a superlens is characterized by near-field amplification, which allows for images of an object with *subwavelength resolution*. This was finally confirmed as well by a transmission line based metamaterial [54]. Here, not only imaging beyond the diffraction

limit<sup>7</sup> was demonstrated but also the growth of evanescent waves within the NIM was directly measured. Thus, the key predictions of the theory had been verified.

All these pioneering experiments have been carried out in the microwave spectral region or even at radio frequencies. Here, wavelengths in the cm range allow for structuring the metamaterial at large scale, which is comparably easy to realize. With the idea of the resonance frequencies being inversely proportional to the structure size of the metamaterial, downscaling appears to be the way to realize superlensing at visible wavelengths. However, this provides a number of problems [34]: In addition to fabrication issues, losses within the conducting structures become more prominent at short  $\lambda$ , which hinders a good performance of the NIM. Apart from that, the design utilizing wires and split rings relies on them behaving like ideal conductors, which breaks down on the nanometer scale and for high frequencies. Nevertheless, employing alternative designs, negative refraction at optical wavelengths has been demonstrated successfully [34, 56].

Even though all these great achievements provide extraordinary new electromagnetic phenomena, the dream of a superlens based microscope that works in the far field and is not limited by diffraction is practically impossible. The reason is dissipation, unavoidably inherent to all materials, no matter if natural or artificially structured. In particular, it has been shown theoretically that resolution improvement in comparison to a conventional lens is not possible over distances much larger than  $\lambda$  [24], which is just as short as a few hundreds of nanometers in the visible .

Due to this severe restriction, superlens based imaging experiments providing subwavelength resolution were all performed in the near field. In the electrostatic limit, i.e. at scales significantly smaller than  $\lambda$ , Pendry suggested [22] that there is even no need for elaborate fabrication of metamaterials, since naturally occurring negative permittivity  $\epsilon$  is sufficient (see Section 3.1.3). Silver was exploited for a proof-of-principle study of such kind, the *near-field superlens*, indeed confirming the enhancement of evanescent waves [57] and demonstrating near-field imaging well beyond the diffraction limit [58]. With the effect occurring in the ultraviolet (UV), silver has been envisioned for use in photolithography [25]. In the infrared, on the other hand, silicon carbide (SiC) [36], perovskites [37, 38] and graphene [59] revealed subwavelength imaging capabilities.

In all of these cases, superlensing is observed at one particular wavelength only, with a certain bandwidth. Here, this wavelength is determined by the plasma frequency [25, 58, 59] or the spectral position of a phonon resonance [36, 37, 38], depending on the

---

<sup>7</sup>Note that subwavelength imaging was also demonstrated before by implementing so-called Swiss Roll structures [55]. This metamaterial, however, is not a real NIM, merely exhibiting negative permeability  $\mu$  rather than  $n^* < 0$  which gives rise to reconstruction of the magnetic field component in the static limit (see Section 3.1.3).



respective mechanism of image formation (*plasmonic* or *phononic* superlens, see Section 3.3). Therefore, the limited spectrum of suitable materials restricts accessible operating wavelengths. There are several approaches to tackle this limitation. On the one hand, a multilayered stack of dielectrics with different phonon frequencies [60] and the concept of an "unmatched superlens" [61] have been discussed in order to broaden the bandwidth of a superlens. On the other hand, plasmonic systems offer the possibility to change the spectral behavior by manipulation of electronic properties. Correspondingly, doped graphene [62] and metal-dielectric composites [63, 64] have been suggested for spectrally adjustable near-field imaging, potentially covering the visible and infrared spectral regions. In particular, semiconductors have been discussed to be exploited as plasmonic devices [40, 65, 66, 67], where the doping level determines the operational wavelength. The present work deals with the first experimental demonstration of such a near-field superlens [26], making use of gallium arsenide (GaAs) doped with silicon (Si).

# 4 Fundamentals II - Near-field optical microscopy

*This chapter lays the theoretical foundation for scattering-type scanning near-field optical microscopy (s-SNOM), which is the experimental technique used to investigate the near-field superlens in this work. In s-SNOM, a nm-sized probe is brought into the near-field region of a sample, acting as a scatterer that transfers the subwavelength-scaled optical information into the accessible far field. Usually, and also in our case, this probe is the tip of an atomic force microscope (AFM). Approximating the tip by a spherical particle of same curvature radius, the quasi-electrostatic dipole model gives an analytical expression for the amplitude and phase of the scattered near field, which together yield information about the local complex permittivity of the sample. Here, the spatial resolution is determined by the radius of the probe, independent of the wavelength. Moreover, small negative values of the sample's permittivity give rise to a resonant increase of the scattering amplitude and strong phase changes, accompanied by a characteristic dependence on the probe-sample distance, where the usual case is nonlinear decay of both amplitude and phase away from the surface. When operating the AFM in tapping mode, the probe oscillates vertically to the sample surface at a frequency  $\Omega$ . The nonlinear distance dependence of the probe-sample coupling gives rise to a modulation of the scattered near field at higher harmonics of  $\Omega$ . By demodulating the signal at these higher orders unwanted far-field background can be suppressed, as the latter is only modulated at the fundamental frequency.*

## 4.1 Concept

The diffraction limit, restricting optical resolution to structure sizes in the order of the wavelength  $\lambda$ , arises due to the fact that conventional microscopes capture the far-field contribution of an object's electromagnetic wave only (see Section 2). Finer detailed information is confined to the object's surface, where evanescent waves are bound to the so called near-field region: In Chapter 2 we discussed that if the tangential wavenumber  $k_t = \sqrt{k_x^2 + k_y^2}$  (the  $z$ -axis being the surface normal) of an emitted wave, determining the

spatial resolution, reaches values larger than  $\omega/c = 2\pi/\lambda$ , the electric component  $\mathbf{E}$  decays evanescently away from the surface according to

$$\mathbf{E}(\mathbf{r}, t) \propto e^{-\tilde{k}_z z} \quad \text{with} \quad \tilde{k}_z = -ik_z = \sqrt{k_t^2 - \frac{4\pi^2}{\lambda^2}}. \quad (4.1.1)$$

For structure sizes much smaller than  $\lambda$ , this can be approximated (see also Section 3.1.3) by

$$\tilde{k}_z = k_t \quad \text{if} \quad k_t \gg \frac{2\pi}{\lambda}. \quad (4.1.2)$$

This means that, in this regime, spatial information is lost within a distance equal to the dimension of the structure itself. Therefore, if aiming for an optical resolution in the nm-range, a probe has to be positioned in nm-distance from the object, which is enabled experimentally by scanning probe microscopy (SPM) techniques such as scanning tunneling microscopy (STM) [68] and atomic force microscopy (AFM) [69]. Both STM and AFM allow one to precisely scan a tip across a sample at a constant distance from the surface, thereby recording a height profile. Two different approaches are exploited to access the near-field simultaneously to the topography. On the one hand, the probe can be exploited as a small aperture locally illuminating the sample, which is referred to as *aperture scanning near-field optical microscopy*<sup>1</sup> (*a-SNOM*) [8, 13, 70]. On the other hand, the probe can act as a scatterer transferring the local near-field into the far-field, where it can be detected. This method is called *scattering-type scanning near-field optical microscopy* (*s-SNOM*) [9, 11, 12]. Here, the size of the aperture or the scatterer, respectively, defines the resolution, which is independent of  $\lambda$ . In the infrared, which is the spectral region of interest in this work, s-SNOM is the method of choice, primarily because radiation at such a long wavelength cannot pass a nm-sized aperture of a tapered probe due to cutoff effects [14, 15]. In the following, the underlying theory of s-SNOM will be presented.

## 4.2 s-SNOM theory

In this section, we analytically derive the scattering behavior of a subwavelength sized spherical particle, representing the probe in scattering-type scanning near-field optical microscopy (s-SNOM) [71]. Here, when placing the particle in direct proximity of a sample, the amplitude and the phase of the scattered light yield information about its local permittivity. Importantly, the spatial resolution here is given by the particle size, independent of

---

<sup>1</sup>The aperture can also be utilized for local detection, with the illumination not necessarily being confined to the location of interest.

the wavelength.

### 4.2.1 Emission of an oscillating dipole

In s-SNOM, the light scattered by a probe in proximity to the sample surface is detected. For a probe size much smaller than  $\lambda$  (Rayleigh scattering), this corresponds to the emission of an oscillating electric dipole with dipole moment  $\mathbf{P}$  interacting with the sample. Assuming air environment, the electric component  $\mathbf{E}$  of this emitted radiation at the position  $\mathbf{r} = r\mathbf{n}$  relative to the dipole is given by

$$\mathbf{E} = \frac{e^{ikr}}{4\pi\epsilon_0} \left( \frac{k^2}{r} [(\mathbf{n} \times \mathbf{P}) \times \mathbf{n}] + \left( \frac{1}{r^3} - \frac{ik}{r^2} \right) [3\mathbf{n}(\mathbf{n} \cdot \mathbf{P}) - \mathbf{P}] \right), \quad (4.2.1)$$

where the time dependent factor  $e^{-i\omega t}$  is omitted [28, 72]. The detector, located at a distance much larger than the wavelength  $\lambda$ , is only reached by the far-field contribution  $\propto 1/r$ ,

$$\mathbf{E}_s = \frac{1}{4\pi\epsilon_0} \frac{e^{ikr}}{r} k^2 [(\mathbf{n} \times \mathbf{P}) \times \mathbf{n}], \quad (4.2.2)$$

giving rise to the s-SNOM signal (the index of  $\mathbf{E}_s$  refers to *scattered*). Information about local optical properties arises due to the interaction between probe and sample, modifying  $\mathbf{P}$  and thereby generating optical contrast. This coupling occurs at a distance  $r$  much smaller than  $\lambda$  (*near field*), where

$$\mathbf{E}_{nf} = \frac{1}{4\pi\epsilon_0} [3\mathbf{n}(\mathbf{n} \cdot \mathbf{P}) - \mathbf{P}] \frac{1}{r^3} \quad (4.2.3)$$

dominates ( $e^{ikr} \approx 1$ ). In order to interpret the s-SNOM signals, the change of  $\mathbf{P}$  due to the near-field interaction is expressed as a function of the sample's permittivity  $\epsilon$  (we restrict ourselves to non-magnetic materials with  $\mu = 1$ ). This will be the subject of the following discussion.

### 4.2.2 Model of dipole and image dipole

To understand the signals obtained by s-SNOM, the scattering behavior of a small particle (size  $\ll \lambda$ ) [72] in proximity to a half-space of relative permittivity  $\epsilon$  is discussed in this section, representing the s-SNOM probe next to the sample surface. The following discussion is based on the considerations in Ref. [71]. The polarizability  $\alpha$  of such a particle in

air, exposed to an external electric field  $\mathbf{E}_0$ , is defined by

$$\mathbf{P} = \alpha \mathbf{E}_0, \quad (4.2.4)$$

where  $\mathbf{P}$  is the dipole moment induced by  $\mathbf{E}_0$ . In general,  $\alpha$  is a complex valued tensor [72], depending on the shape and the material of the particle. For a homogeneous sphere with a radius  $a \ll \lambda$  and permittivity  $\varepsilon_p$  (the index  $p$  represents particle or probe),  $\alpha$  is given by

$$\alpha = 4\pi\varepsilon_0 a^3 \frac{\varepsilon_p - 1}{\varepsilon_p + 2}. \quad (4.2.5)$$

Here, resonant scattering is expected if  $\varepsilon_p = -2$ , known as the Fröhlich resonance [72]. The optical response of the spherical particle changes when it is placed in the near-field region of the sample at a spacing  $h$ . Here, the scattering is described by the coupled system of the particle's dipole moment  $\mathbf{P}$  (amplitude  $P$ ) and its image dipole moment  $\mathbf{P}'$  (amplitude  $P'$ ) within the sample (see Figure 4.2.1), the latter representing the modification of the scattered field due to a redistribution of charge carriers at the sample's surface. This image dipole is given by

$$\mathbf{P}' = \pm\beta\mathbf{P} \quad \text{with} \quad \beta = \frac{\varepsilon - 1}{\varepsilon + 1}, \quad (4.2.6)$$

where  $\varepsilon$  is the permittivity of the sample and  $\beta$  is the so-called response function. The presence of the sample breaks the symmetry of the system, resulting in a strong dependency of the scattered light on the polarization of the incident electric field  $\mathbf{E}_0$ , which is accounted for by the  $\pm$ -sign in Equation 4.2.6 as explained below. Here, we discuss s- and p-polarization separately, where the former is oriented parallel and the latter perpendicular to the sample surface<sup>2</sup>. In case of p-polarization, the two induced dipoles are parallel to each other ( $P' = +\beta P$ ) whereas antiparallel orientation arises in case of s-polarization ( $P' = -\beta P$ ). This is trivially seen by considering the associated electric field lines (not shown). It immediately becomes clear that, in general, the total scattering amplitude is higher for p-polarized light, where  $P$  and  $P'$  generate fields with the same orientation. In contrast,  $P'$  leads to a reduction of the total field for s-polarization. In the following, we calculate an effective polarizability  $\alpha^{\text{eff}}$  for the two cases, determining the scattering behavior of the coupled system of particle and sample.

---

<sup>2</sup>To be more precise, p-polarized light actually refers to the electric component being parallel to the plane of incidence, also providing a component parallel to the sample surface. However, in the experiment, the latter is small for an angle of incidence as large as  $65^\circ$  (see Figure 8.2.1).

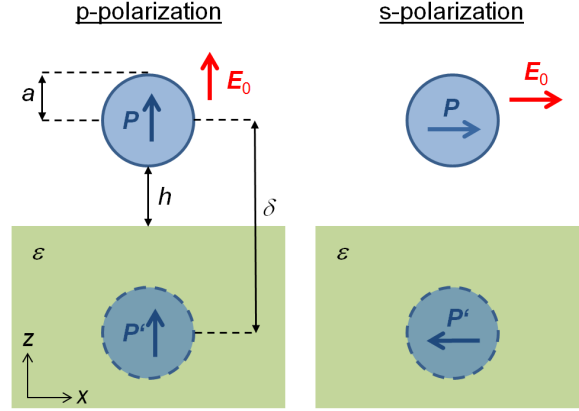


**Figure 4.2.1:** Dipole moment  $\mathbf{P}$  and image dipole moment  $\mathbf{P}'$  of a spherical particle in proximity to a sample of permittivity  $\epsilon$ , induced by an external electric field  $\mathbf{E}_0$  which is assumed to be oriented either perpendicular (left) or parallel (right) to the surface (adapted from Ref. [71]).

### p-polarization

The dipole of the particle,  $\mathbf{P} = \alpha \mathbf{E}_0 = \alpha E_0 \mathbf{e}_z = P \mathbf{e}_z$ , gives rise to an image dipole  $\mathbf{P}' = P' \mathbf{e}_z = +\beta \mathbf{P}$  at a distance  $\delta = 2(h + a)$  (see Figure 4.2.1) which in turn generates an additional electric field  $\mathbf{E}' = E' \mathbf{e}_z$  at the position of the particle, where  $E'$  is given by

$$E' = \frac{P'}{2\pi\epsilon_0\delta^3} = \frac{\beta P}{2\pi\epsilon_0\delta^3}, \quad (4.2.7)$$

This can be seen by applying Equation 4.2.3 to  $\mathbf{P}'$ , considering that the particle is in the near-field region of the sample, i.e. at distance much smaller than  $\lambda$ . Taking this into account, the amplitude of the dipole  $\mathbf{P}$  in presence of the sample is modified according to

$$P = \alpha(E_0 + E') = \alpha E_0 + \frac{\alpha\beta P}{2\pi\epsilon_0\delta^3} \quad (4.2.8)$$

and therefore

$$P = \frac{\alpha}{1 - \frac{\alpha\beta}{2\pi\epsilon_0\delta^3}} E_0. \quad (4.2.9)$$

The field scattered by the particle-sample system, which is measured in SNOM, equals the combined far-field emission of  $P$  and  $P'$ . To account for  $P'$ , the effective polarizability  $\alpha_{\perp}^{\text{eff}}$  is introduced<sup>3</sup>

$$\alpha_{\perp}^{\text{eff}} = \frac{P^{\text{eff}}}{E_0} = \frac{P + P'}{E_0} = \frac{(1 + \beta)P}{E_0}. \quad (4.2.10)$$

<sup>3</sup>The index  $\perp$  accounts for the p-polarization perpendicular to the sample surface.

Applying Equation 4.2.9 and inserting  $\delta = 2(h + a)$ , we get

$$\alpha_{\perp}^{\text{eff}} = \frac{\alpha(1 + \beta)}{1 - \frac{\alpha\beta}{16\pi\epsilon_0(h+a)^3}}. \quad (4.2.11)$$

### s-polarization

In this case,  $\mathbf{E}_0 = E_0\mathbf{e}_x$  and therefore  $\mathbf{P} = P\mathbf{e}_x$ , generating an image dipole  $\mathbf{P}' = P'\mathbf{e}_x = -\beta\mathbf{P}$ . In addition to  $\mathbf{E}_0$ , the particle senses the near-field  $\mathbf{E}' = E'\mathbf{e}_x$  of  $\mathbf{P}'$ , with

$$E' = -\frac{P'}{4\pi\epsilon_0\delta^3} = \frac{\beta P}{4\pi\epsilon_0\delta^3}. \quad (4.2.12)$$

Following the same argumentation as for p-polarized light (note the different magnitudes of  $E'$  for the two cases),  $P$  in presence of the sample is calculated by accounting for an effective total electric field  $E_0 + E'$ , giving rise to an effective polarizability<sup>4</sup>

$$\alpha_{\parallel}^{\text{eff}} = \frac{\alpha(1 - \beta)}{1 - \frac{\alpha\beta}{32\pi\epsilon_0(h+a)^3}}. \quad (4.2.13)$$

As discussed previously,  $|\alpha_{\parallel}^{\text{eff}}|$  in general is smaller than  $|\alpha_{\perp}^{\text{eff}}|$  due to the antiparallel arrangement of  $P$  and  $P'$ . In particular, the common case  $\beta \approx 1$  yields  $P \approx -P'$  for s-polarization, resulting in vanishing scattering of the coupled system of particle and sample. So even though assuming a symmetric particle, the scattering efficiency is larger for p-polarized radiation where the fields of  $P$  and  $P'$  superpose constructively.

### 4.2.3 Scattering characteristics

Since in our investigations exclusively p-polarized light is applied, which is required for near-field superlensing in non-magnetic materials (see Section 3.1.3), we solely consider  $\alpha_{\perp}^{\text{eff}}$  in the following<sup>5</sup>. The scattered electric field reaching the detector, which is located at  $\mathbf{r} = r\mathbf{n}$  with respect to the sample, is given by

$$\mathbf{E}_s = \frac{1}{4\pi\epsilon_0} \frac{e^{ikr}}{r} k^2 \alpha_{\perp}^{\text{eff}} [(\mathbf{n} \times \mathbf{E}_0) \times \mathbf{n}], \quad (4.2.14)$$

<sup>4</sup>The index  $\parallel$  accounts for the s-polarization parallel to the sample surface.

<sup>5</sup>Note that in the experiment, the probe is the apex of an elongated AFM tip (see Section 4.3) pointing towards the sample surface rather than a spherical particle, which already gives the dipole the tendency to oscillate in  $z$ -direction.

where the dielectric function  $\varepsilon$  of the sample is taken into account by  $\alpha_{\perp}^{\text{eff}} = \alpha_{\perp}^{\text{eff}}(\beta) = \alpha_{\perp}^{\text{eff}}(\beta(\varepsilon))$  (see Equations 4.2.2, 4.2.4, 4.2.6 and 4.2.11). Since in general  $\varepsilon$  is a complex quantity, this also applies to  $\alpha_{\perp}^{\text{eff}}$  and we can write

$$\alpha_{\perp}^{\text{eff}} := \sigma = se^{i\varphi} = \frac{\alpha(1 + \beta)}{1 - \frac{\alpha\beta}{16\pi\varepsilon_0(h+a)^3}}, \quad (4.2.15)$$

where  $\sigma$  is by definition [73] the complex *scattering coefficient*,  $s$  the *scattering amplitude* and  $\varphi$  the *scattering phase*. These are the quantities to be measured by s-SNOM, which contain the information about the sample's local complex permittivity. The power of the scattered light, which is detected, can be calculated by integrating the Poynting vector  $\mathbf{S}_s = \mathbf{E}_s \times \mathbf{H}_s$  over the area of the detector (neglecting background radiation, which is considered in Section 4.4.). However, an interpretation of the absolute signal is hardly possible, since it strongly depends on the exact shape of the AFM probe, which is unknown and differs from tip to tip. Therefore, the evaluation of s-SNOM signals is usually performed in a relative fashion, comparing the signals obtained with different samples or at different locations of one sample, the latter giving rise to optical contrast. Given that the conditions of two measurements are the same, i.e. the same AFM tip being equally illuminated (constant  $\mathbf{E}_0$ ) at equal distances from the surface, this allows for a comparison of the respective local permittivities. Labeling the two measurements with indices  $A$  and  $B$ , this relation is given by

$$\frac{E_s^A}{E_s^B} = \frac{\sigma(\varepsilon^A)}{\sigma(\varepsilon^B)}. \quad (4.2.16)$$

Thus, the analytical dipole model can be applied to predict the optical contrast between materials with different  $\varepsilon$ . Typically, reference measurements on gold samples are performed in order to obtain quantitative information.

Usually, metals like gold, aluminum or platinum are utilized as probe materials. In the infrared, which is the spectral region of interest in this work, metals exhibit a spectrally flat response with permittivities in the order of  $\varepsilon \approx -1000 + 1000i$  [74]. Therefore, the polarizability  $\alpha$  of the probe (see Equation 4.2.5) can be approximated by

$$\alpha \approx 4\pi\varepsilon_0 a^3. \quad (4.2.17)$$

Taking this into account and considering the response function  $\beta = \beta(\varepsilon) = \beta(\varepsilon' + i\varepsilon'')$  (see Equation 4.2.6), the scattering coefficient for the probe being in contact with the sample



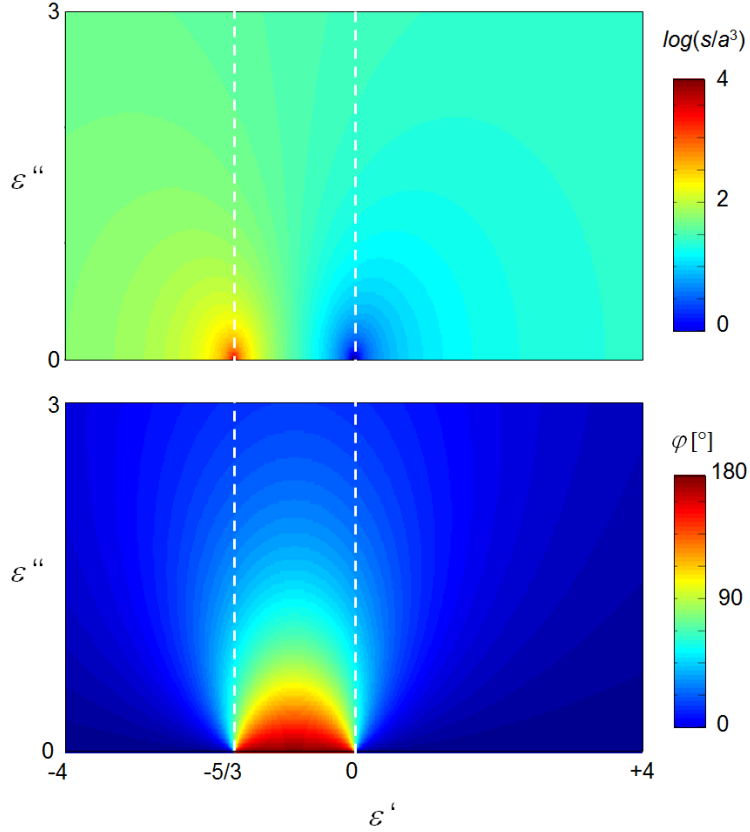


**Figure 4.2.2:** Scattering amplitude  $s$  and scattering phase  $\varphi$  of a metallic particle with radius  $a$  in contact with a plane sample of permittivity  $\varepsilon = \varepsilon' + i\varepsilon''$ . The amplitude  $s$  is normalized to  $a^3$  and plotted in logarithmic scale for better visibility. For this calculation,  $\varepsilon_0$  is set to 1.

( $h = 0$ ) is given by

$$\sigma = 32\pi\varepsilon_0 a^3 \frac{\varepsilon' + i\varepsilon''}{3(\varepsilon' + i\varepsilon'' + \frac{5}{3})}. \quad (4.2.18)$$

Obviously, the permittivity of the sample impacts both the amplitude  $s$  and the phase  $\varphi$  of  $\sigma = se^{i\varphi}$  and therefore of the scattered electric field  $\mathbf{E}_s \propto \sigma$ . A resonant increase of  $s$  can be expected if  $\varepsilon' = -5/3$  accompanied by a small value of  $\varepsilon''$ , whereas it experiences a minimum at  $\varepsilon' = 0$ . In the latter case p-polarization exceptionally yields antiparallel orientation of dipole  $P$  and image dipole  $P'$ , since  $\beta = -1$ . Note that, on the other hand,  $\varepsilon = 1$  results in  $\sigma = \alpha$ , which corresponds to the particle in absence of a sample. As can be seen in Figure 4.2.2, the overall behavior gets much less pronounced for lossy materials, i.e. larger values of  $\varepsilon''$ . This also applies to the phase  $\varphi$ , which shifts by up to  $180^\circ$  (small  $\varepsilon''$ ) in the region  $\varepsilon' = -5/3$  to  $\varepsilon' = 0$ .

SNOM data are usually obtained with the probe oscillating in the direction perpendicular to the sample surface, which allows for separating the signal from undesired background

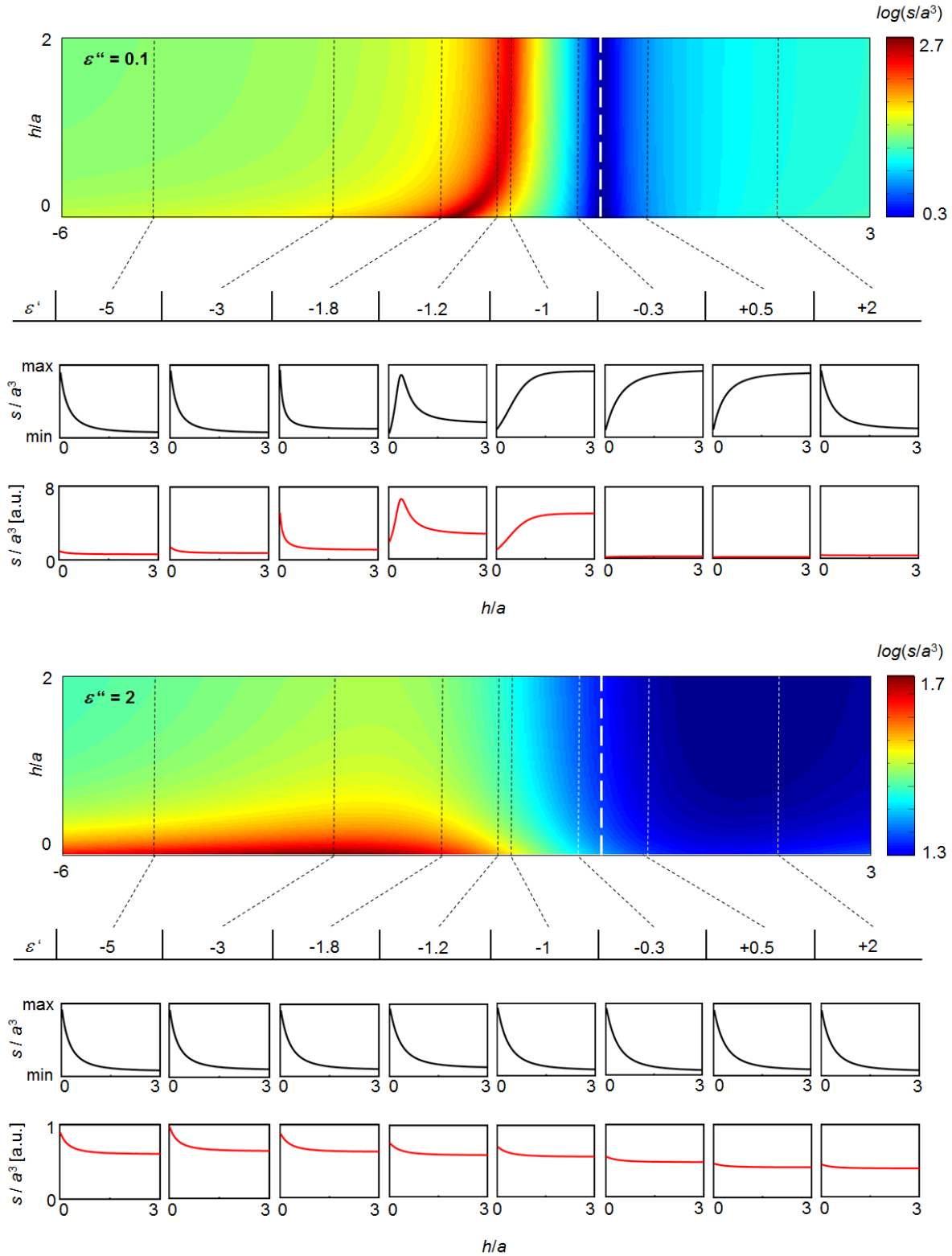


**Figure 4.2.3:** Scattering amplitude  $s$  of a metallic particle with radius  $a$  as function of the distance  $h$  to a plane sample of real permittivity  $\epsilon'$  with constant imaginary part  $\epsilon'' = 0.1$  (top) and  $\epsilon'' = 2$  (bottom), respectively. For this calculation,  $\epsilon_0$  is set to 1. For selected  $\epsilon'$ ,  $s(h)$  is shown both on an arbitrary (black curve) and an absolute scale (red curves; note the different scales for the two cases).

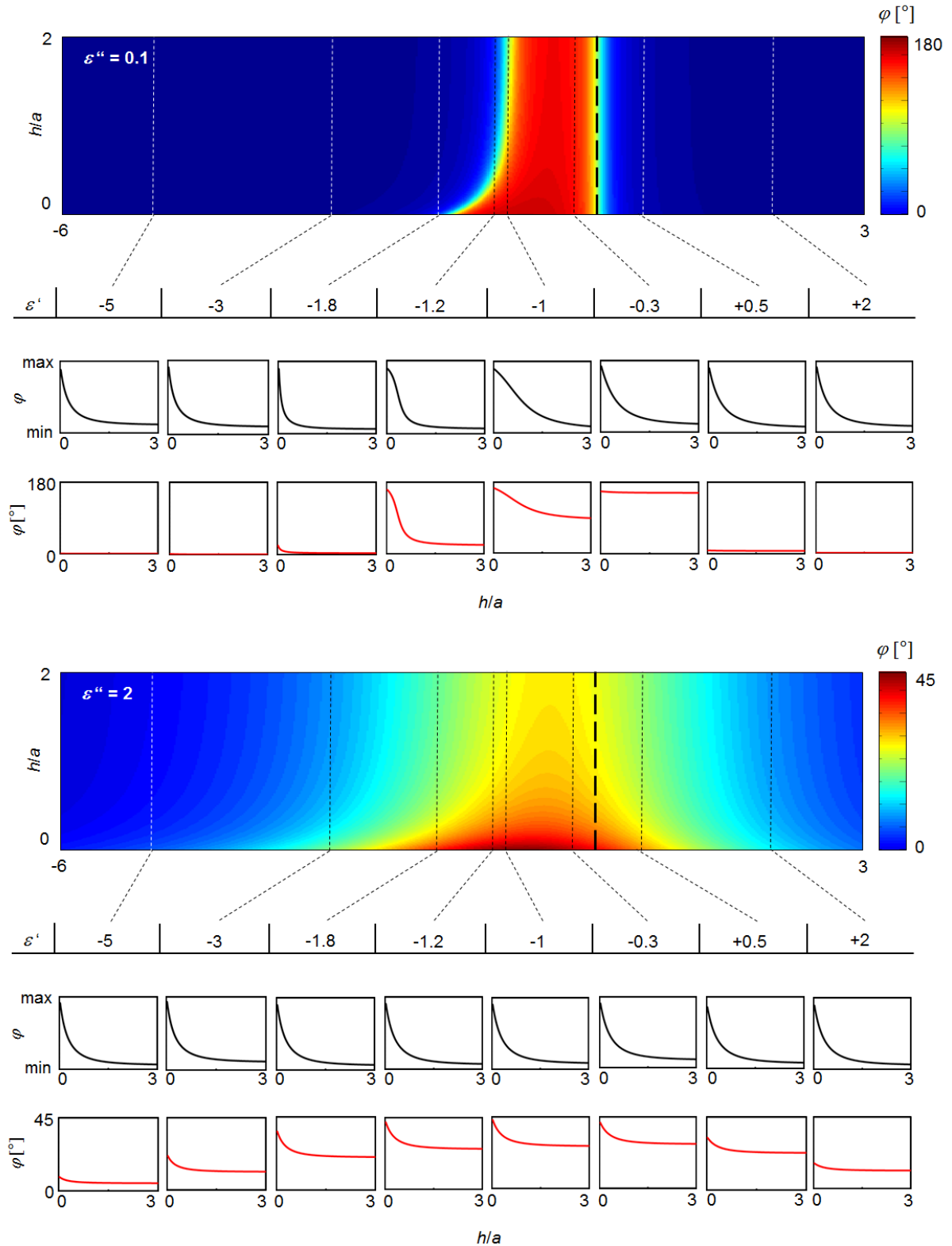


**Figure 4.2.4:** Scattering phase  $\varphi$  of a metallic particle with radius  $a$  as function of the distance  $h$  to a plane sample of real permittivity  $\varepsilon'$  with constant imaginary part  $\varepsilon'' = 0.1$  (top) and  $\varepsilon'' = 2$  (bottom), respectively. For selected  $\varepsilon'$ ,  $\varphi(h)$  is shown both on an arbitrary (black curves) and an absolute scale (red curves; note the different scales for the two cases).

reflections (see Section 4.4). Therefore, it is also important to know how  $\sigma$  depends on the probe-sample distance  $h$ . For non-resonant samples, i.e.  $|\varepsilon'| \gg 1$ , we can approximate  $\beta \approx 1$  which results in

$$s = \frac{8\pi\varepsilon_0 a^3}{1 - \frac{1}{4}\left(\frac{a}{h+a}\right)^3}. \quad (4.2.19)$$

Here, phase changes are negligible and  $s$  is largest for  $h = 0$ , decreasing with increasing  $h$  in a nonlinear fashion. In proximity to  $\varepsilon' = 0$ , however, this is not necessarily true. Figures 4.2.3 and 4.2.4 provide an overview on  $s(h)$  and  $\varphi(h)$ , respectively, for  $\varepsilon' = -6$  to  $+3$ . Two cases are shown: on the one hand  $\varepsilon'' = 0.1$ , corresponding to a sample inhering rather low losses, and on the other hand  $\varepsilon'' = 2$ , representing more dissipation. As one can see, both  $s$  and  $\varphi$  in general decay rapidly when increasing  $h$ . However, in case of low losses, the characteristic behavior of the  $h$ -dependence changes between  $\varepsilon' = -1.5$  and  $+1$ . This in particular applies to  $s$ , which in this region *increases* with increasing  $h$ , providing a maximum at  $h \neq 0$ . This corresponds to a shift of the resonance for different  $h$ . Here,  $s$  reaches its maximum value for  $\varepsilon' = -5/3$  if the particle is in contact with the sample ( $h = 0$ ), whereas for  $h > a$  the condition is  $\varepsilon' = -1$ . The behavior of  $\varphi(h)$ , on the other hand, changes not as drastically (aside from absolute values), however a slower decrease in this region is clearly noticeable. All of these peculiarities around  $\varepsilon' \approx -1$ , both for  $s(h)$  and  $\varphi(h)$ , disappear for larger losses, i.e.  $\varepsilon'' = 2$ . Note that for very dissipative samples, i.e.  $\varepsilon'' \gg 1$ , we obtain  $\beta \rightarrow 1$ , which corresponds to the non-resonant case given by Equation 4.2.19.

As a final remark, the signal strength  $\propto s$  increases with increasing particle size, however this comes with a reduction of spatial resolution, which is determined by  $a$ . Moreover, it affects the  $h$ -dependence of  $\sigma$ , which as well occurs on the scale of  $a$ .

### 4.3 AFM tip as a scatterer

In the experiment, the s-SNOM probe is a sharp, pyramid shaped tip of a scanning probe microscope (SPM), which is in our case an atomic force microscope (AFM) (see Section 7.1). In contrast, the analytical description of s-SNOM in the previous sections was based on the assumption that the scatterer is a spherical particle with radius  $a$ . Hence, the question arises to what extent the theory is applicable to experimental results, where  $a$  is the curvature radius of the probe's apex. It has been shown in various works [75, 76] that, despite neglecting the real shape of the tip, material contrasts due to different permittivities can be well explained by this approach. Also, the distance dependence of the near-field

coupling between tip and sample (see Figures 4.2.3 and 4.2.4) agrees qualitatively well with the experiment [77], as well as the spectral behavior of the near-field signal [78], considering  $\varepsilon = \varepsilon(\lambda)$ . For a quantitative consensus, however, more precise models are required, making use of complex numerical simulations which take into account a realistic shape of the scatterer [79, 80]. In particular, the elongated shape of an AFM tip has to be considered when studying polarization dependent effects. Since this is not the case in this work, such a detailed analysis is not required here.

## 4.4 Signal formation

In the s-SNOM measurements performed in this work the scattered radiation is detected by a mercury cadmium telluride (MCT) detector, generating a voltage that is proportional to the optical power  $P_{det}$  at its active surface. Here,  $P_{det}$  in turn is proportional to the square modulus of the detected electric-field component,

$$P_{det} \propto |\mathbf{E}_{det}|^2. \quad (4.4.1)$$

The quantity of interest is the light scattered at the SNOM probe's apex only, providing the electric field  $\mathbf{E}_s$  (see Equation 4.2.14) which contains the information about the sample's local near-field. However, unavoidably, radiation is not only scattered at the tip's apex, but also at surrounding structures like the shaft of the tip, the cantilever or other scattering centers at the sample surface (edges, particles...), causing an additional electric field  $\mathbf{E}_b$  (background radiation, see Figure 4.4.1). The two fields at the position of the detector can be written as

$$\mathbf{E}_s = E_s \mathbf{e}_s e^{i(\omega t + \varphi_s)} \quad (4.4.2)$$

$$\mathbf{E}_b = E_b \mathbf{e}_b e^{i(\omega t + \varphi_b)}, \quad (4.4.3)$$

oscillating at the same angular frequency  $\omega$ , but differing in amplitude  $E$ , orientation  $\mathbf{e}$  and phase  $\varphi$ . Taking into account the unwanted background,  $P_{det}$  is given by

$$\begin{aligned} P_{det} &\propto |\mathbf{E}_s + \mathbf{E}_b|^2 \\ &= E_s^2 + E_b^2 + 2E_s E_b \mathbf{e}_s \cdot \mathbf{e}_b \cos(\varphi_s - \varphi_b) \end{aligned} \quad (4.4.4)$$

In general,  $E_s$  is much smaller than  $E_b$ , manifesting a severe challenge in s-SNOM, which is the separation of the tiny near-field signal from a large background (note in particular that the phase  $\varphi_b$  of this background is unknown). To this end, one makes use of the fact

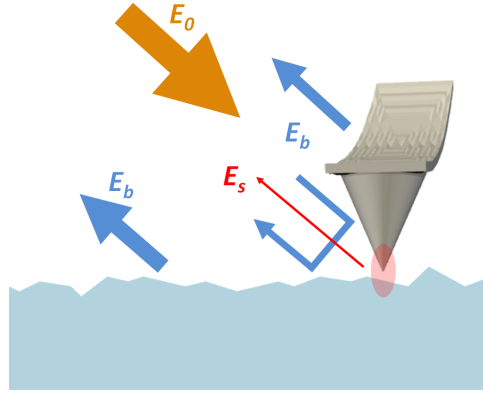


**Figure 4.4.1:** The AFM tip is illuminated by radiation with an electric field  $\mathbf{E}_0$ . The light reaching the detector consists of both the scattered field  $\mathbf{E}_s$  at the apex of the tip and the elsewhere scattered background field  $\mathbf{E}_b$ .

that when increasing the distance  $h$  between probe and tip by  $\Delta h$ ,  $E_s$  is strongly modified in a nonlinear fashion, whereas there is only a slight linear change of  $E_b$  (see Figure 4.4.2) [71]. On the one hand, the nonlinear behavior of  $E_s$  is caused by the short range near-field coupling between tip and sample, which occurs on a scale of the probe's curvature radius  $a$ , namely

$$E_s \propto \frac{1}{1 - C \left(\frac{a}{h+a}\right)^3}, \quad (4.4.5)$$

where  $C$  depends on the polarizability of the tip  $\alpha$  and the response of the sample  $\beta$  (see Equations 4.2.14 and 4.2.15). Note that  $E_s$  varies on the scale of  $a$ , independent of the wavelength  $\lambda$ . On the other hand, a change of  $E_b$  arises due to a displacement of the tip shaft and the cantilever within the (far-)field generated by the laser radiation (this includes not only the beam profile itself, but also standing wave patterns, which possibly arise across the sample surface due to scattering events at structures surrounding the tip), varying on a scale of  $\lambda$ . If  $\Delta h$  is much smaller than  $\lambda$ , this is accompanied by only a slight modification of  $E_b$  changing linearly with  $h$ . In the experiment, the probe is a metalized AFM tip with an apex radius  $a$  of about 50 nm, operated in so called tapping mode (or amplitude-modulated (AM) mode, see Section 7.1), where the probe is oscillating with an amplitude  $A = \Delta h$  of about 100 nm (peak to peak). Since experiments are performed in the mid-infrared region ( $\lambda \approx 20 \mu\text{m}$ ), the condition  $\Delta h \ll \lambda$  is well fulfilled and we can assume a linear variation of  $E_b$ ,

$$E_b \propto \tilde{C} + C' \cdot h. \quad (4.4.6)$$

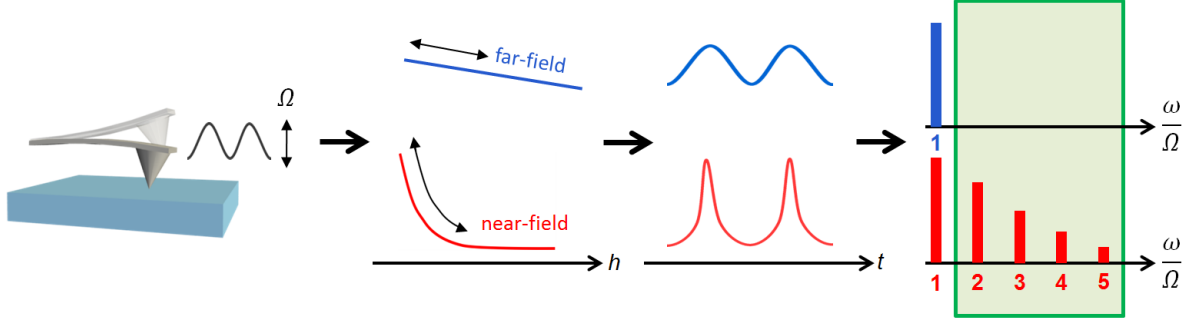


**Figure 4.4.2:** Schematic of the signal demodulation: The oscillation of the s-SNOM tip at a frequency  $\Omega$  gives rise to a modulation of the scattered near-field, decaying nonlinearly away from the sample surface, at higher harmonics of  $\Omega$ . In contrast, the linearly varying far-field background just results in a modulation at the fundamental frequency. Hence, lock-in demodulation at higher harmonics yields a near-field signal with suppressed background (adapted from Ref. [81]).

Here, the constant part  $\tilde{C}$  comprises, for instance, the light scattered from the sample surface, which is not affected by the tapping of the cantilever. In the following, this unmodulated electric field will be denoted as  $\mathbf{E}_{bc}$  (constant), while  $\mathbf{E}_{bm}$  (modulated) represents the background modulated by the cantilever motion (linear in  $h$ ).

The oscillation of the tip gives rise to a periodic modulation of the detected power  $P_{det}$  according to

$$P_{det} = P_{det}(h(t)). \quad (4.4.7)$$

For small amplitudes  $A$  the oscillation is harmonic and can be written as

$$h(t) = h_0 + \frac{1}{2}A(1 + \cos(\Omega t)), \quad (4.4.8)$$

where  $h_0$  is the lower turning point. The total field scattered at the system of sample and oscillating tip can be written as [71]

$$\mathbf{E}_{det} = \mathbf{E}_{bc} + \mathbf{E}_{1,mod} \cos(\Omega t) + \mathbf{E}_{2,mod} \cos(2\Omega t) + \dots, \quad (4.4.9)$$

with

$$\mathbf{E}_{n,mod} = E_{n,mod} \mathbf{e}_{n,mod} e^{i(\omega t + \varphi_{n,mod})}, \quad (4.4.10)$$

Here, all components  $\mathbf{E}_{n,mod} = \mathbf{E}_{n,s} + \mathbf{E}_{n,bm}$  contain both the near-field scattered at the

SNOM tip,  $\mathbf{E}_{n,s}$ , and the  $h$ -modulated part of the far-field scattered at the tip shaft and cantilever,  $\mathbf{E}_{n,bm}$ . For the measured power  $P_{det}$  this yields<sup>6</sup> [71]

$$\begin{aligned}
P_{det} &\propto |\mathbf{E}_{det}|^2 = \mathbf{E}_{det}\mathbf{E}_{det}^* \\
&= \text{constant} + |\mathbf{E}_{bc}|^2 \\
&+ [\text{Re}(\mathbf{E}_{1,mod}\mathbf{E}_{2,mod}^*) + 2\text{Re}(\mathbf{E}_{bc}\mathbf{E}_{1,mod}^*)] \cos(\Omega t) \\
&+ \left[\frac{1}{2}|\mathbf{E}_{1,mod}|^2 + 2\text{Re}(\mathbf{E}_{bc}\mathbf{E}_{2,mod}^*)\right] \cos(2\Omega t) \\
&+ \text{higher harmonics}
\end{aligned} \tag{4.4.11}$$

Typically, the light scattered at the sample surface and surrounding structures exceeds the radiation modulated by the tip oscillation by far,

$$E_{bc} \gg E_{n,mod}, \tag{4.4.12}$$

making the first term in each bracket negligible. As already indicated in the beginning of this section, the modulation of the slowly varying far-field  $E_{bm}$  is significantly weaker than the modulation of the scattered near-field  $E_s$ . Due to the linear dependence of the background this effect gets even more prominent with increasing harmonic according to [71]

$$\frac{E_{n,s}}{E_{n,bm}} = \left(\frac{\lambda}{2\pi a}\right)^n. \tag{4.4.13}$$

This means that, the higher the order  $n$ , the more efficient the suppression of non-local scattering events. On the other hand, the signal strength decreases with increasing  $n$ , making the optimum frequency  $n\Omega$  for lock-in demodulation a trade off between background-free data acquisition and signal strength. For a sufficiently high value of  $n$  we can approximate  $\mathbf{E}_{n,mod} \approx \mathbf{E}_{n,s}$ . Hence, the near-field signal  $NF_{n\Omega}$ , demodulated at the frequency  $n\Omega$ , reads

$$\begin{aligned}
NF_{n\Omega} &\propto \text{Re}(\mathbf{E}_{bc}\mathbf{E}_{n,s}^*) \\
&= 2E_{bc}E_{n,s}\mathbf{e}_{bc}\mathbf{e}_s \cos(\varphi_{bc} - \varphi_{n,s}) \\
&\propto E_{bc}E_{n,s} \cos(\varphi_{bc} - \varphi_{n,s}).
\end{aligned} \tag{4.4.14}$$

Note that the polarization  $\mathbf{e}_s = \mathbf{e}_{n,s}$  is not impacted by the tip oscillation. According to Equation 4.2.14, the field  $\mathbf{E}_s$  scattered at the probe's apex is proportional to the scattering

<sup>6</sup>The asterisk \* denotes the conjugated complex of respective fields. Here, we apply  $\mathbf{E}_i\mathbf{E}_j^* + \mathbf{E}_j\mathbf{E}_i^* = 2\text{Re}(\mathbf{E}_i\mathbf{E}_j^*)$  (real part). Furthermore, the following trigonometric relations are applied:  $\cos^2(x) = \frac{1}{2}(1 + \cos(2x))$  and  $2\cos(x)\cos(2x) = \cos(x) + \cos(3x)$ .



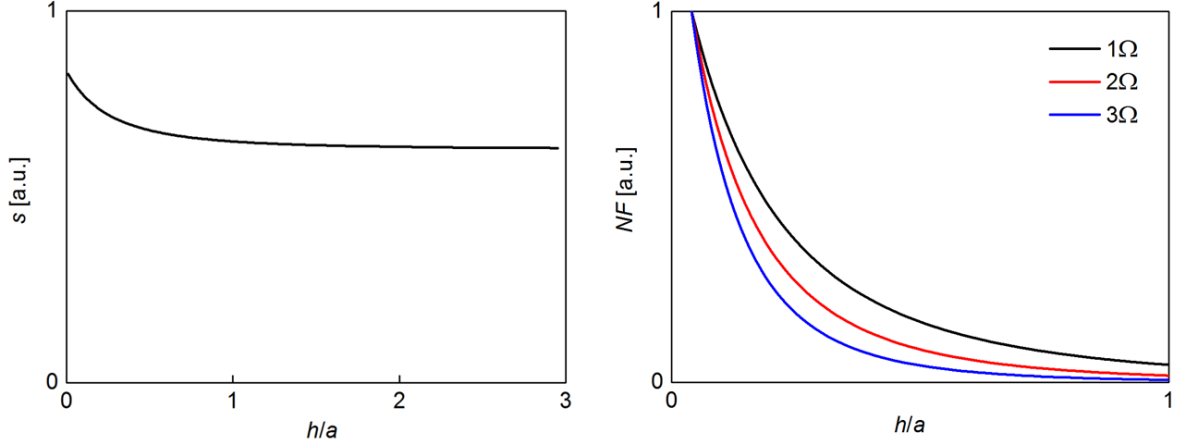


**Figure 4.4.3:** Scattering amplitude  $s$  and near-field signal  $NF_{n\Omega}$  at non-resonant condition as a function of the probe-sample distance  $h$ , where  $h$  is normalized to the curvature radius  $a$  of the s-SNOM probe.

coefficient  $\sigma$ ,

$$\mathbf{E}_s \propto \mathbf{e}_s \sigma = \mathbf{e}_s s e^{i\varphi}, \quad (4.4.15)$$

where  $\sigma$  was derived analytically in Section 4.2.3 (Equation 4.2.15). Here, the scattering amplitude  $s$  and the scattering phase  $\varphi$  yield the information about the complex local permittivity of the sample, being the quantity of interest in s-SNOM. Since the modulation of  $\mathbf{E}_s$  by the tip oscillation exclusively arises due to the  $h$ -dependency of  $s(h)e^{i\varphi(h)}$ , we can express the Fourier coefficients  $\mathbf{E}_{n,s}$  as

$$\mathbf{E}_{n,s} \propto \mathbf{e}_s s_n e^{i\varphi_n}, \quad (4.4.16)$$

where both the proportionality factor and  $\mathbf{e}_s$  are independent of  $h$ . Inserting this into Equation 4.4.14, the near-field signal can be written as

$$NF_{n\Omega} \propto E_{bc} s_n \cos(\varphi_{bc} - \varphi_n), \quad (4.4.17)$$

where  $s_n$  and  $\varphi_n$  are given by the Fourier transformation

$$s_n e^{i\varphi_n} = \frac{\Omega}{\pi} \int_0^{2\pi/\Omega} s(h(t)) e^{i\varphi(h(t))} \cos(n\Omega t) dt. \quad (4.4.18)$$

For oscillation amplitudes  $\Delta h$  much smaller than the curvature radius  $a$  of the probe apex, the  $n^{\text{th}}$  Fourier component is given by the  $n^{\text{th}}$  derivative of  $s e^{i\varphi}$  with respect to the distance  $h$  [82]. At non-resonant conditions, i.e. no resonant enhancement of the near-field coupling

between probe and sample, changes of the scattering phase  $\varphi$  are negligible when increasing the distance  $h$ , whereas the amplitude  $s$  provides a nonlinear decay (see Equation 4.2.19). In this case and assuming that  $\Delta h \ll a$ , Figure 4.4.3 depicts both  $s$  and  $NF_{n\Omega} \propto s_n$  for the first three harmonics as a function of  $h$ . As one can see, in each case the signal decays to almost zero within a distance in the order of  $a$ , where the dependence steepens with increasing demodulation harmonic. For larger oscillation amplitudes (in the experiment,  $\Delta h$  is typically in the order of  $a$ ), the general behavior remains the same, while the decay of  $NF_{n\Omega}$  becomes less steep [71].

Even though the modulation of the near-field signal  $NF$  by the tip oscillation significantly eases the interpretation of the obtained signal, since complicated interference terms can be neglected, the evaluation is still aggravated by the unknown phase relation between background radiation  $\mathbf{E}_{bc}$  and light scattered at the probe  $\mathbf{E}_s$  [83]. In particular, a phase change of the background during a measurement gives rise to a change of the signal which might be erroneously interpreted as near-field contrast. Nevertheless, we will discuss in Section 7.4 why the measurements obtained with our setup are not significantly impacted by such artifacts. In general, however, this is not true. The issue can be overcome by applying an additional field  $\mathbf{E}_{ref}$  of *controlled phase*  $\varphi_{ref}$  which interferes with the scattered near-field. If this field is much stronger than the unmodulated background,  $E_{ref} \gg E_{bc}$ , the latter can be neglected and the demodulated near-field signal is given by

$$NF_{n\Omega} \propto E_{ref} s_n \cos(\varphi_{ref} - \varphi_n). \quad (4.4.19)$$

This approach is referred to as *interferometric detection* (in contrast to *non-interferometric detection*, also referred to as *direct detection*), allowing for disentangled extraction of both the scattering amplitude  $s$  and phase  $\varphi$ . Note that Equation 4.4.19 refers to so-called *homodyne* interferometric detection, where the wavelength of the reference field is the same as of the field scattered at the probe. In contrast, the wavelengths are shifted with respect to each other for *heterodyne* interferometric detection, giving rise to beatings of the signal at the difference frequency. For details, see for instance Refs. [84, 85, 86].



# 5 Doped GaAs as a superlens material

*In this chapter we discuss the potential of n-doped GaAs to be exploited as a plasmonic near-field superlens with an operational wavelength adjustable by doping. First, an analytical expression of the dielectric function based on the Drude-Lorentz model is introduced, taking into account free electrons and optical phonons. Here, the electronic response to infrared radiation is determined by the density and the scattering rate of the electrons. By changing the doping level, the superlensing wavelength can be controlled over a wide infrared spectral range, the losses being rather constant at operational conditions. However, there is a short wavelength limit at  $\lambda \approx 15 \mu\text{m}$  due to a maximum obtainable electron density by doping with silicon. At high doping levels in the range of  $10^{19} \text{ cm}^{-3}$  autocompensation of free electrons becomes an issue. As we will see, this effect results in increased dissipation without opening up new spectral ranges and should therefore be avoided. Finally, the role of the electron effective mass on the analysis is discussed.*

## 5.1 Concept

Near-field superlensing through a thin layer takes place if the real permittivity of the slab exhibits same absolute value and opposite sign as the surrounding medium (see Equation 3.2.7), relying on the excitation of localized surface polaritons, as we qualitatively discussed in Section 3.3. By sandwiching a n-doped GaAs layer between two intrinsic layers, as shown in Figure 5.1.1, localized surface *plasmon* polaritons (SPPs) appear at the two interfaces if

$$\varepsilon'_{\text{n-GaAs}}(\lambda_{\text{SL}}) = -\varepsilon'_{\text{GaAs}}(\lambda_{\text{SL}}), \quad (5.1.1)$$

where  $\varepsilon'_{\text{GaAs}}$  and  $\varepsilon'_{\text{n-GaAs}}$  are the real parts of the dielectric functions  $\varepsilon$  of the undoped layers and the doped layer, respectively. Since negative  $\varepsilon'_{\text{n-GaAs}}$  arises due to the presence of free electrons forming SPPs, we will refer to the layered system as a *plasmonic near-field superlens* (in contrast to a phononic superlens [36, 37, 38]). For the superlensing wave-

length  $\lambda_{\text{SL}}$ , the transfer of evanescent waves through the three-layered system is resonantly enhanced. Placing an object at one side of the slab, this enhancement can be exploited to obtain an image with subwavelength resolution on the other side. The objective of this work is to confirm the superlensing performance of such a system based on doped GaAs.

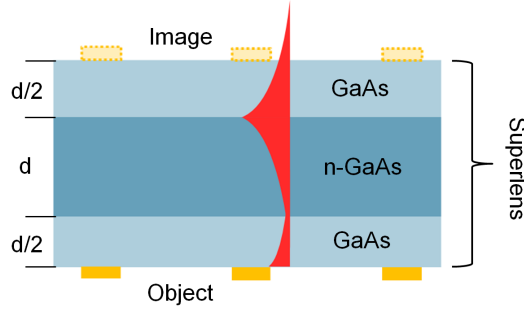


**Figure 5.1.1:** Performance of a three-layered GaAs superlens at resonance condition (Equation 5.1.1). The red feature indicates the enhancement of the object's near-field through the slab.

## 5.2 Infrared dielectric function

The optical response of a non-magnetic material (permeability  $\mu = 1$ ) like GaAs can equivalently be described in terms of its relative permittivity  $\varepsilon$  (also called dielectric function) and its refractive index  $n^*$ , being directly linked to each other via

$$n^* = \sqrt{\varepsilon}. \quad (5.2.1)$$

In general,  $n^*$  and  $\varepsilon$  are frequency dependent, complex quantities,

$$n^*(\omega) = n'(\omega) + in''(\omega), \quad (5.2.2)$$

$$\varepsilon(\omega) = \varepsilon'(\omega) + i\varepsilon''(\omega). \quad (5.2.3)$$

Here,  $n''$  is directly related to the absorption coefficient [27]

$$\alpha = \frac{2\omega n''}{c}. \quad (5.2.4)$$

In many cases, absorption is directly associated with  $\varepsilon''$ . It is true that if  $\varepsilon'' \ll \varepsilon'$  and  $\varepsilon' > 0$ , which often applies, dissipation is negligible. However, in general,  $\alpha$  depends on

both  $\varepsilon'$  and  $\varepsilon''$ , since

$$n'' = \sqrt{\frac{\sqrt{\varepsilon'^2 + \varepsilon''^2} - \varepsilon'}{2}}. \quad (5.2.5)$$

Nevertheless, we will consider  $\varepsilon''$  as a synonym for dissipation within the near-field superlens, since it is the relevant parameter for the obtainable resolution (see Equation 3.2.9) at a given  $\varepsilon'$ , the latter defining the resonance condition of superlensing (see Equation 5.1.1). While  $n^*$ , and therefore  $\alpha$ , is used in the context of propagating electromagnetic waves,  $\varepsilon$  is the more convenient choice in the near-field region, where electric and magnetic fields are decoupled.

For radiation wavelengths  $\lambda$  with a photon energy well below the band-gap energy ( $E_g = 1.42 \text{ meV} \hat{=} \lambda_g = 870 \text{ nm}$  [87]), the permittivity of doped GaAs is well described by the Drude-Lorentz model. Here, the dispersion  $\varepsilon(\omega)$  is derived by describing the light's impact on the free-electrons and the crystal lattice through classical equations of motion [27, 44], taking into account respective oscillation resonance frequencies and damping constants. Based on such an analysis, the infrared permittivity of doped GaAs is given by [87]

$$\varepsilon(\omega) = \varepsilon_{\text{optic}} - \frac{\omega_{\text{TO}}^2 (\varepsilon_{\text{static}} - \varepsilon_{\text{optic}})}{\omega^2 - \omega_{\text{TO}}^2 + i\omega\gamma_{\text{p}}} - \frac{\omega_{\text{p}}^2 \varepsilon_{\text{optic}}}{\omega^2 + i\omega\gamma_{\text{el}}}. \quad (5.2.6)$$

For the phononic part, represented by the second term, the energy of the transverse optical phonon  $\hbar\omega_{\text{TO}} = 33.25 \text{ meV}$  and the associated damping coefficient  $\gamma_{\text{ph}}$  with  $\hbar\gamma_{\text{ph}} = 0.25 \text{ meV}$  are well known from literature<sup>1</sup>, as well as the static (low-frequency) permittivity  $\varepsilon_{\text{static}} = 12.85$  and the optical (high-frequency) permittivity  $\varepsilon_{\text{optic}} = 10.88$  [87]. The electronic response (third term), on the other hand, of course depends on the doping level, which determines both the plasma frequency  $\omega_{\text{p}}$  as the natural (angular) frequency of an electron density oscillation, and the scattering rate  $\tau$  of the electrons that describes the damping  $\gamma_{\text{el}}$  of the plasma oscillation. Here, both  $\gamma_{\text{el}}$  and  $\omega_{\text{p}}$  are a function of the electron density  $n$ , however there is only an analytical expression for the latter [87],

$$\omega_{\text{p}} = \sqrt{\frac{ne^2}{m^* \varepsilon_0 \varepsilon_{\text{optic}}}}, \quad (5.2.7)$$

where  $\varepsilon_0$  is the permittivity of vacuum,  $-e$  the charge of an electron and  $m^*$  its effective mass in the conduction band of GaAs. For  $\gamma_{\text{el}}(n)$  please see Section 5.3.

<sup>1</sup>Note that the energy of the longitudinal optical phonon,  $\hbar\omega_{\text{LO}} = 36.13 \text{ meV}$ , is built into this model by the Lyddane-Sachs-Teller relation,  $\varepsilon_{\text{static}}/\varepsilon_{\text{optic}} = (\omega_{\text{LO}}/\omega_{\text{TO}})^2$ .

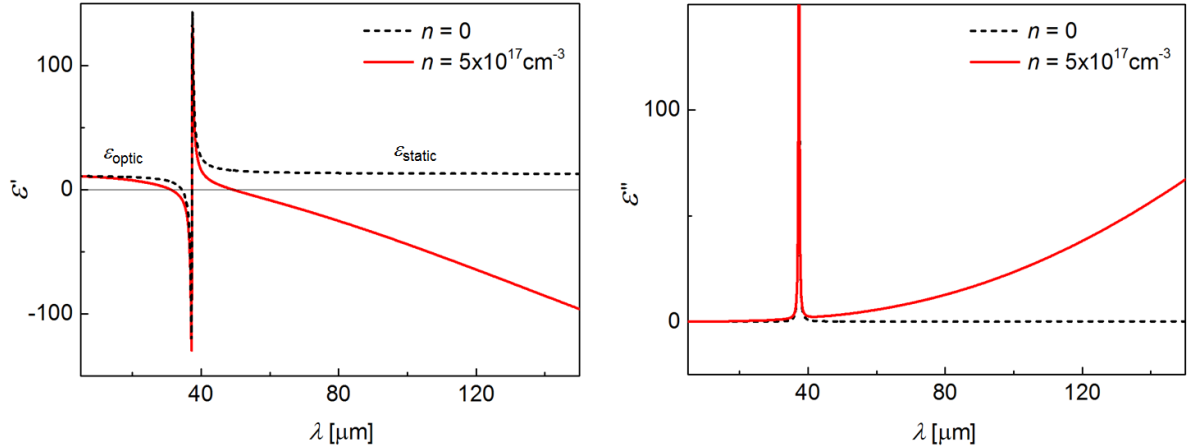


**Figure 5.2.1:** Real part  $\varepsilon'$  and imaginary part  $\varepsilon''$  of the dielectric function  $\varepsilon$  of GaAs. The black dashed and red solid line correspond to intrinsic ( $n = 0$ ) and doped ( $n = 5 \times 10^{17} \text{cm}^{-3}$ ) GaAs, respectively.

In Figure 5.2.1,  $\varepsilon'$  and  $\varepsilon''$  are shown both for intrinsic and doped GaAs, depicted as a function of  $\lambda$ . In the undoped case,  $\varepsilon$  is rather constant except the region of phonon resonances (this is also called the Reststrahlen band), with  $\varepsilon' \approx \varepsilon_{\text{optic}}$  for shorter and  $\varepsilon' \approx \varepsilon_{\text{static}}$  for longer  $\lambda$ . With the same exception of phononic absorption,  $\varepsilon''$  is negligibly small over the whole spectral range. This does not apply to doped GaAs, where Drude absorption by free charge-carriers is reflected by an increase of  $\varepsilon''$  and negative values of  $\varepsilon'$  at long  $\lambda$ , the latter being required for the occurrence of the near-field superlensing effect (see Section 5.4).

As a side note, it may be mentioned that Equation 5.2.6 simplifies the actual system by not considering the potential creation of phonon combinations [88] and oversimplifying the coupling of phonons and plasmons [89]. However, it is known from terahertz time-domain spectroscopy that the Drude-Lorentz model well describes the ac-conductivity in n-GaAs in the far-infrared [90, 91]. In the spectral range of interest in this work, involving the Reststrahlen band of GaAs, the reflectance spectra of the superlenses (layers of doped and intrinsic GaAs) could be fitted with very good accuracy, providing meaningful results for the electronic quantities  $n$  and  $\gamma_{\text{el}}$  which are used as fitting parameters (see Section 6.3.1). This was confirmed by the comparison to values obtained by Hall measurements (see Section 6.3.2), where the data analysis does not involve the dielectric function. Therefore, we assume that for our samples, it is reasonable to apply the Drude-Lorentz model to simulate the superlensing effect (see Section 8.1), which was investigated in the same spectral region as the reflectance measurements.

### 5.3 Damping versus electron density

In order to calculate the expected superlensing wavelength  $\lambda_{\text{SL}}$  of a plasmonic superlens, one has to know both the electron density  $n$  and the electron damping  $\gamma_{\text{el}}$ , determining the permittivity of the conductive layer. Here,  $\gamma_{\text{el}}$  increases with increasing  $n$  as a consequence of increased Coulomb scattering. However, there is no analytical expression that quantitatively describes the dependence  $\gamma_{\text{el}}(n)$ . In this section, we take into account experimental results from literature to obtain a relation, which will be the basis for our calculations in Section 5.4.

Doping a III-V semiconductor with a group IV element can result in both free electrons and free holes. Such a behavior is called amphoteric doping, which for instance applies to doping GaAs with Si. If Si (group IV) occupies a Ga (group III) site, it acts as a donor, however if it replaces As (group V), it is an acceptor. While the usual case is n-doping (which is also true for the samples investigated in this work), p-doping can be obtained by choosing appropriate growth conditions (e.g. temperature, substrate orientation etc. [92]). Figure 5.3.1a depicts the free carrier concentration  $n$  of a Si doped MBE-grown GaAs film as a function of the dopant density  $n_{\text{dop}}$  (i.e. Si concentration), obtained in a temperature range  $T = 750 - 820$  K [93]. Here, this yields free electrons. Up to  $n_{\text{dop}} \approx 7 \times 10^{18} \text{cm}^{-3}$ , every Si atom is incorporated as a donor, so  $n = n_{\text{dop}}$ . For larger  $n_{\text{dop}}$  however (higher Si flux),  $n$  saturates and eventually decreases. This is attributed to an autocompensation mechanism: in this regime, some of the Si atoms tend to occupy the As site, creating holes which recombine with electrons, resulting in a reduction of  $n$ . The example depicted in Figure 5.3.1a corresponding to optimum growth conditions regarding high values of  $n$ , the free electron density in GaAs obtained by doping with Si is limited to  $n \approx 7 \times 10^{18} \text{cm}^{-3}$ . For other growth conditions (e.g. higher temperatures, see [93]), the general behavior is similar, however with  $n$  saturating at smaller values.

Like in all semiconductors, the mobility  $\mu$  of electrons in doped GaAs drops with increasing doping level  $n_{\text{dop}}$  due to an increase of scattering events with impurities. In the Drude model of electrical conduction, the scattering time  $\tau$  and the electron damping  $\gamma_{\text{el}}$  can equivalently be employed to describe the conducting behavior. The former is related to  $\mu$  via

$$\mu = \frac{e\tau}{m^*}, \quad (5.3.1)$$

where  $\tau$  yields  $\gamma_{\text{el}}$  in units of angular frequency according to

$$\gamma_{\text{el}} = \frac{1}{\tau}. \quad (5.3.2)$$



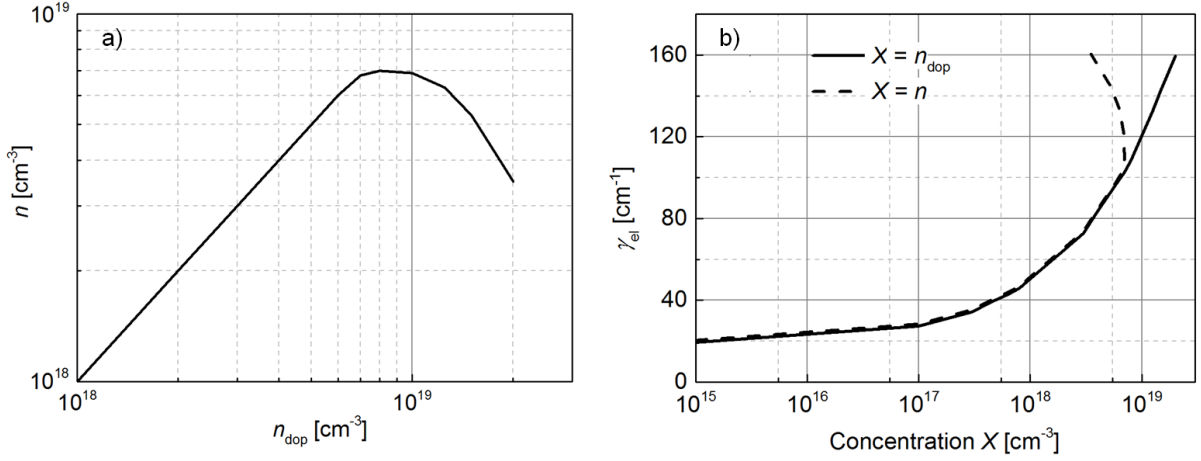


**Figure 5.3.1:** (a) Free electron concentration  $n$  as a function of the dopant concentration  $n_{\text{dop}}$  in a Si doped MBE-grown GaAs film. Values were obtained for growth temperatures  $T = 750 - 820$  K [93]. (b) Electron damping  $\gamma_{\text{el}}$  in units of spectroscopic wavenumbers versus  $n_{\text{dop}}$  (solid line) and  $n$  (dashed line), respectively, based on  $n(n_{\text{dop}})$  in (a) and  $\gamma_{\text{el}}(n_{\text{dop}})$  in Ref. [94].

In this thesis,  $\gamma_{\text{el}}$  is indicated in corresponding units of spectroscopic wavenumbers. Derived from drift mobility measurements [94], Figure 5.3.1b depicts the increase of  $\gamma_{\text{el}}$  with increasing doping  $n_{\text{dop}}$  (solid line), corresponding to a decrease of  $\mu$ . Since, as mentioned above, autocompensation causes a reduction of  $n$  at high  $n_{\text{dop}}$ ,  $\gamma_{\text{el}}$  can take two values for a given  $n$  in this regime, depending on whether the point of saturation was exceeded or not (dashed line). For the calculations in the following section, this  $\gamma_{\text{el}}(n)$  will be applied to obtain the expected superlensing conditions for a given  $n$ . It is important to be conscious that the numbers given here correspond to specific sample growth conditions, which are likely to be different in another case. Therefore, it is recommended to perform a proper electronic characterization of a superlens sample rather than to rely on absolute values given here.

## 5.4 Superlensing condition adjustable by doping

Exploiting a doped semiconductor as a plasmonic superlens provides the potential to adjust the operational wavelength  $\lambda_{\text{SL}}$  (superlensing wavelength) by changing the doping level. In this work, the superlens consists of a doped GaAs layer sandwiched between two intrinsic layers, as introduced in Section 5.1. The permittivity  $\varepsilon_{\text{n-GaAs}}$  of the middle layer, determining  $\lambda_{\text{SL}}$ , depends on the electron density  $n$  and the electron damping  $\gamma_{\text{el}}$  (see

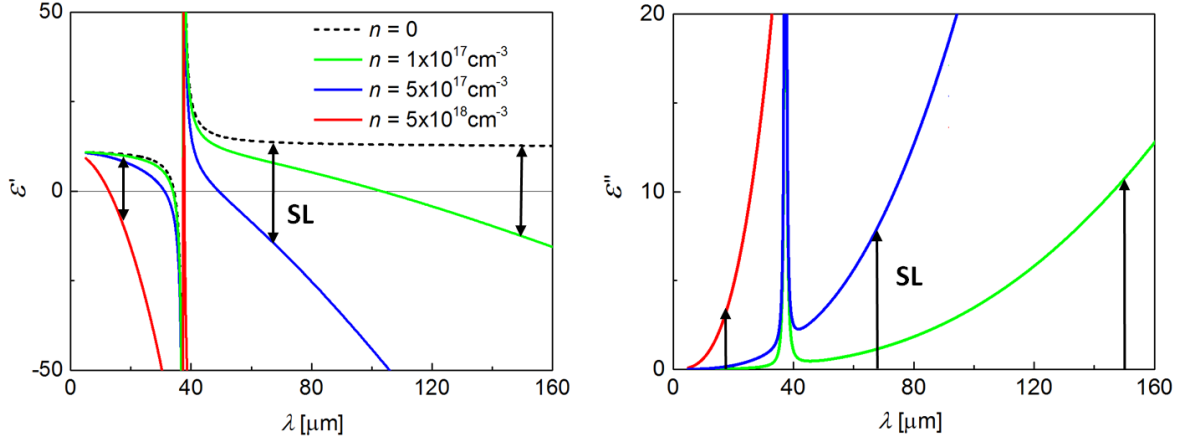


**Figure 5.4.1:** Real part  $\varepsilon'_{n\text{-GaAs}}$  (left) and imaginary part  $\varepsilon''_{n\text{-GaAs}}$  (right) of the dielectric function  $\varepsilon_{n\text{-GaAs}}$  of  $n$ -doped GaAs in the infrared region, calculated for various electron densities  $n$  (the dashed line corresponds to  $\varepsilon'_{\text{GaAs}}$  of intrinsic GaAs). For each  $n$ , black arrows indicate where superlensing (SL) can be expected.

Section 5.2), where the latter increases with increasing  $n$ . Considering  $\gamma_{\text{el}}(n)$  presented in Section 5.3,  $\varepsilon_{n\text{-GaAs}}$  can be calculated by applying Equation 5.2.6. For various  $n$ , we depict the real part  $\varepsilon'_{n\text{-GaAs}}$  and the imaginary part  $\varepsilon''_{n\text{-GaAs}}$  in Figure 5.4.1. Black arrows indicate the superlensing wavelengths  $\lambda_{\text{SL}}$  for the different  $n$  of the doped layer, according to the condition given by Equation 5.1.1. As can be seen, increasing  $n$  results in shorter  $\lambda_{\text{SL}}$ , induced by a spectral shift of the plasma frequency. For the imaging capability of the GaAs superlens at resonance, the critical parameter is the ratio  $\varepsilon''_{n\text{-GaAs}}(\lambda_{\text{SL}})/\varepsilon'_{n\text{-GaAs}}(\lambda_{\text{SL}})$  (see Equation 3.2.9), where it is important to note that, aside from the Reststrahlen band, dissipation within the intrinsic outer layers is negligible. Note that  $\varepsilon'_{n\text{-GaAs}}(\lambda_{\text{SL}}) \approx -12$  independent of  $\lambda_{\text{SL}}$ , set by the resonance condition with respect to the rather constant permittivity of the intrinsic layer (see Figure 5.4.1). Hence,  $\varepsilon''_{n\text{-GaAs}}(\lambda_{\text{SL}})$  is the quantity that determines the obtainable resolution. Despite a strong increase of absorption with  $\lambda$  for a given electron density,  $\varepsilon''_{n\text{-GaAs}}(\lambda_{\text{SL}})$  increases only weakly with  $\lambda_{\text{SL}}$ , as indicated by the black arrows. In the latter case, however, any increase seems counterintuitive, since large values of  $\lambda_{\text{SL}}$  correspond to superlenses with small  $n$ , where little dissipation could be expected. Indeed, a decrease of  $n$  results in less absorption at a given  $\lambda$ , however  $\lambda_{\text{SL}}$  increases, which is accompanied by larger values of  $\varepsilon''$ . As one can see the latter effect dominates, altogether making high  $n$  accompanied by short  $\lambda_{\text{SL}}$  preferable.

Figure 5.4.2a gives an overview about the expected superlensing wavelength  $\lambda_{\text{SL}}$  for electron densities in a range from  $n = 1 \times 10^{17} \text{cm}^{-3}$  up to  $n = 7 \times 10^{18} \text{cm}^{-3}$ . In Figure 5.4.2b, the associated values of  $\varepsilon''_{n\text{-GaAs}}(\lambda_{\text{SL}})$  are depicted. The region of phonon resonances

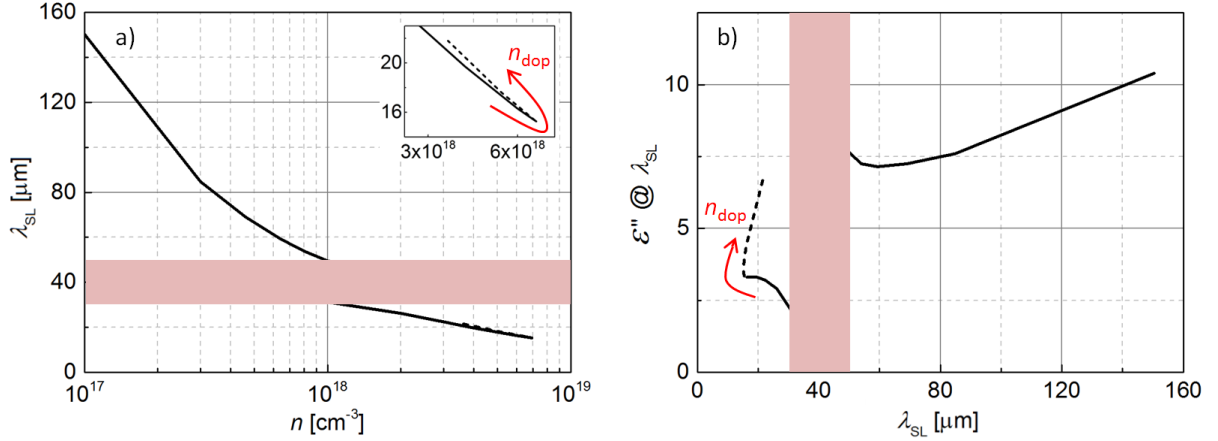


**Figure 5.4.2:** (a) Calculated superlensing wavelength  $\lambda_{\text{SL}}$  as a function of the electron density  $n$  of the doped GaAs layer. The red rectangle marks the Reststrahlen region. Inset: Region of high  $n$  magnified. (b) Imaginary part  $\epsilon''_{\text{n-GaAs}}$  of the permittivity as a function of  $\lambda_{\text{SL}}$ . For both graphs, the dashed line corresponds to the region of autocompensation of  $n$  (see Section 5.3).

(Reststrahlen band), which would predominate the desired plasmonic response of the superlens, is covered by red rectangles since it is beyond the scope of this work. A density of  $n \approx 7 \times 10^{18} \text{cm}^{-3}$  results in  $\lambda_{\text{SL}} \approx 15 \mu\text{m}$ . Since no higher electron density can be obtained by n-doping GaAs with Si (see Section 5.3), this can be regarded as the short wavelength limit for such a superlens. On this side of the Reststrahlen band,  $\lambda_{\text{SL}}$  slowly increases with decreasing  $n$  down to about  $n = 1 \times 10^{18} \text{cm}^{-3}$ . A more prominent increase of  $\lambda_{\text{SL}}$  comes with further decrease of  $n$ , finally reaching  $\lambda_{\text{SL}} \approx 150 \mu\text{m}$  for  $n \approx 1 \times 10^{17} \text{cm}^{-3}$ . Regarding  $\epsilon''_{\text{n-GaAs}}(\lambda_{\text{SL}})$ , the calculations reveal rather constant values of about 3 on the short wavelength side of the Reststrahlen band, whereas  $\epsilon''_{\text{n-GaAs}}(\lambda_{\text{SL}}) \approx 7$  up to 10 on the long wavelength side. As described in Section 5.3, there is autocompensation of free electrons for doping concentrations  $n_{\text{dop}} > 7 \times 10^{18} \text{cm}^{-3}$ , which results in a decrease of  $n$  with increasing  $n_{\text{dop}}$ . Here, the electronic damping  $\gamma_{\text{el}}$  increases further with increasing  $n_{\text{dop}}$ , regardless of the saturation of  $n$ . Since  $\epsilon$  is a function of both  $n$  and  $\gamma_{\text{el}}$ , a given  $n$  can result in different  $\lambda_{\text{SL}}$  in this regime of heavy doping, as it can be accompanied by different values of  $\gamma_{\text{el}}$ . In Figure 5.4.2, the dashed line corresponds to  $n_{\text{dop}} > 7 \times 10^{18} \text{cm}^{-3}$ . While  $\lambda_{\text{SL}}(n)$  is hardly affected (see inset of Figure 5.4.2a),  $\epsilon''_{\text{n-GaAs}}(\lambda_{\text{SL}})$  strongly increases when entering this region of charge carrier saturation. This in turn is accompanied by a drastic degradation of obtainable resolution, as can be seen by applying<sup>2</sup> Equation 3.2.9, and hence should be avoided.

<sup>2</sup>Note, however, that for quantitative accuracy  $\epsilon'' \ll |\epsilon'|$  is required, which is not the case here.

Finally, it should be noted that Figure 5.4.2 is intended to provide a qualitative guidance rather than quantitative numbers. Absolute values of  $\gamma_{\text{el}}(n)$ , which form the basis for the calculations made in this section, depend on the specific MBE growth conditions, which might vary from sample to sample. This is especially valid for very high doping concentrations, where autocompensation may occur, as previously mentioned. In addition, the present considerations are based on literature values extracted from *dc* drift mobility measurements in n-GaAs [94], which may, even for the same sample, quantitatively differ from *ac* values that are relevant for the superlens investigation. This issue is addressed in more detail in Section 6.3.3.

## 5.5 Role of the effective mass

Amongst others, the electron effective mass  $m^*$  is one of the parameters that determine the dielectric function  $\varepsilon$  of n-GaAs. Here,  $m^*$  is given by the curvature of the dispersion relation  $E_{\text{el}}(k_{\text{el}})$ , where  $E_{\text{el}}$  is the electron's energy and  $k_{\text{el}}$  its wavenumber. It is given by [44]

$$m^* = \hbar^2 \left( \frac{d^2 E_{\text{el}}}{dk_{\text{el}}^2} \right)^{-1}. \quad (5.5.1)$$

The low temperature value  $m^* = 0.067m_0$  ( $m_0$  is the mass of a free electron) for electrons at the bottom of the  $\Gamma$  band, i.e. for low electron concentrations  $n$ , is well established [87]. However, due to the non-parabolicity of the conduction band minimum and the thermal expansion of the crystal lattice,  $m^*$  changes with  $n$  and temperature  $T$ , respectively. Figure 5.5.1 depicts how  $m^*$  evolves when independently increasing  $T$  [87] or  $n$ , the latter referring to the calculated curve in Ref. [95]. On the one hand, increasing  $T$  reduces  $m^*$ , whereas it gets larger with increasing  $n$ . As one can see, the influence of  $n$  is much more pronounced, however there is no consensus in literature about absolute values of  $m^*(n)$ , where various calculations and investigations are not yielding quantitative agreement [87, 95]. In particular, we are not aware of room temperature data in literature.

In this work, heavily degenerate semiconductor samples with an electron concentration in the range of  $n = 5 \times 10^{18} \text{cm}^{-3}$  were investigated at room temperature, where for above mentioned reasons, precise values of  $m^*$  are uncertain. Therefore, we insert a constant value of  $m^* = 0.067m_0$  in all our calculations throughout this thesis and legitimate this approximation in the following: To this end, we neglect the weak temperature dependence and show point by point that considering  $m^* = m^*(n)$  would not considerably influence the various aspects of this work. Here, we exemplarily assume the dependence  $m^*(n)$  shown in Figure 5.5.1, presuming that similar behavior is valid at room temperature.

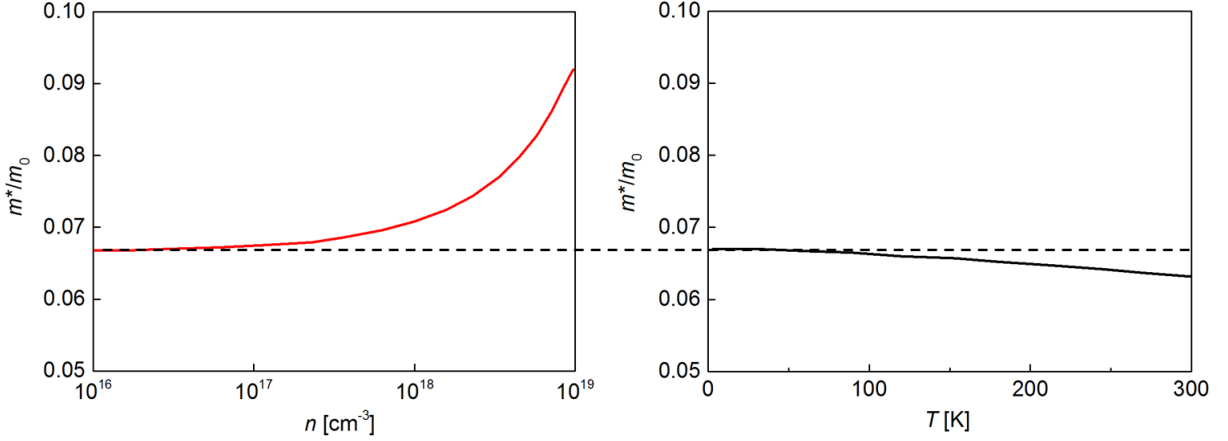


**Figure 5.5.1:** Effective mass  $m^*$  of electrons in the  $\Gamma$  band of GaAs. Red line (left): Increase of  $m^*$  with increasing electron density  $n$  at low temperatures [95]. Black line (right): Decrease of  $m^*$  (band-edge) with increasing temperature  $T$  [87].

- *FTIR measurements (see Section 6.3.1):* Values of  $n$  and  $\gamma_{\text{el}}$  (electron damping) are obtained by utilizing them as fitting parameters for the reflectance simulation, where  $n$  determines the plasma frequency  $\omega_p \propto \sqrt{n/m^*}$  of the doped GaAs layer. Considering  $n \approx 5 \times 10^{18} \text{cm}^{-3}$ , which is in the order of the expected  $n$  for all of the investigated superlens samples, suggests  $m^* \approx 0.08m_0$  if taking into account  $m^* = m^*(n)$ . This results in an increase of the extracted  $n$  by a factor of about 1.2 as compared to the assumption of the band-edge effective mass. In contrast, obtained values of  $\gamma_{\text{el}}$  are unaffected by taking into account the increase of  $m^*$ .
- *Hall measurements (see Section 6.3.2):* Here,  $n$  and  $\mu$  (electron mobility) are determined regardless of  $m^*$ . However, calculating  $\gamma_{\text{el}}$  involves  $m^*$ ,  $\gamma_{\text{el}} \propto 1/(\mu \cdot m^*)$ . So in this case  $n$  stays unaffected, whereas  $\gamma_{\text{el}}$  is reduced by a factor of about 1.2.
- *Calculations (see Section 5.4):* The expected superlensing wavelength  $\lambda_{\text{SL}}$  is calculated as a function of  $n$ , as well as  $\epsilon''_{\text{n-GaAs}}$  at superlensing conditions, which is the relevant parameter for the performance of the superlens. To this end,  $\gamma_{\text{el}}(n)$  is extracted from drift mobility measurements, applying  $\gamma_{\text{el}} \propto 1/(\mu \cdot m^*)$ . In addition,  $m^*$ -dependence arises due to  $\omega_p = \omega_p(m^*)$ . In Figure 5.5.2 it is shown that considering  $m^* = m^*(n)$  barely influences the calculations. It will be seen later that the deviations in  $\lambda_{\text{SL}}(n)$  are much smaller than the operation bandwidth of the superlens (see Section 8.6).
- *Simulation (see Section 8.1):* In order to simulate the performance of a superlens

sample, the permittivity  $\varepsilon_{n\text{-GaAs}}$  of the doped layer is calculated. Here,  $\varepsilon$  is determined by fitting FTIR measurements, where  $n$  and  $\gamma_{\text{el}}$  are the fitting parameters. It is important to notice that, no matter what value is assumed for  $m^*$ , this will just result in a modified extracted value of  $n$  (see first item in this list). In contrast,  $\varepsilon_{n\text{-GaAs}}$  (and therefore also the transfer function) is not affected at all. This can also be understood by regarding  $n/m^*$  as an "effective fitting parameter", which does not change when changing  $m^*$ .

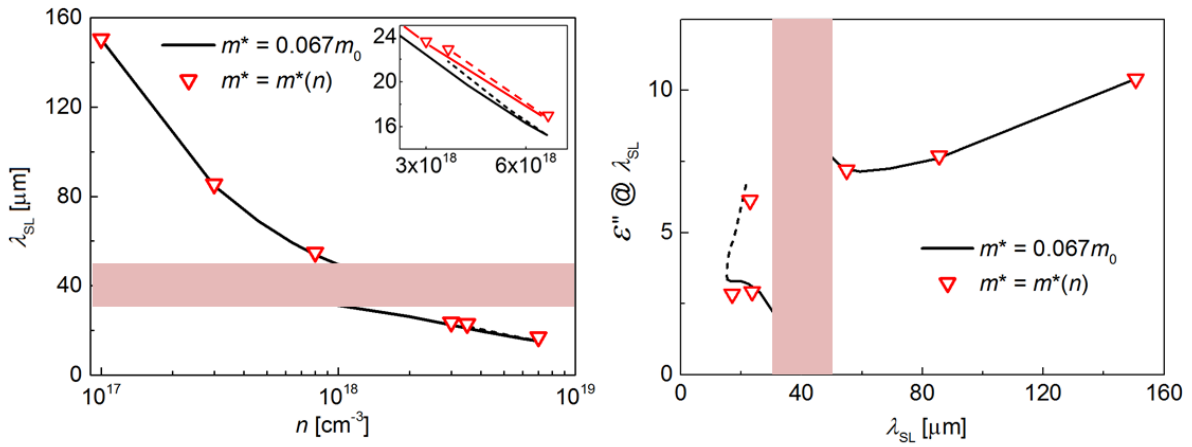


**Figure 5.5.2:** Calculated  $\lambda_{\text{SL}}(n)$  and  $\varepsilon''_{n\text{-GaAs}}(\lambda_{\text{SL}})$  (see Figure 5.4.2). For the black line  $m^* = 0.067m_0 = \text{const.}$  was assumed, the red triangles were computed by inserting  $m^*(n)$  depicted in Figure 5.5.1.



# 6 Preparation and characterization

*In this chapter, we describe how the GaAs superlens structure, grown by molecular beam epitaxy, is further pre-examined and prepared for near-field investigations. The essential constituent of a complete sample is a three-layered system of doped and intrinsic GaAs (which is the superlens) with a total thickness of a few hundred nanometers, placed on top of a gold structure, which serves as the object to be imaged. Here, the processing involves wet chemical etching as well as optical lithography. Being of vital importance for the plasmonic superlensing effect, the electronic properties of the middle, doped layer are determined by both Hall- and Fourier transform infrared spectroscopy (FTIR) measurements. In the latter case, reflectivity measurements are fitted by a multilayer reflectivity simulation based on the Drude-Lorentz model. Also applying FTIR, we exclude that constituents of the sample other than the superlens (glue, gold object, sample holder) give rise to a resonant response to infrared radiation, which could mistakenly be attributed to the superlens.*

## 6.1 Preparation

As depicted schematically in Figure 6.1.1, the preparation of the superlens samples for the near-field investigation comprises the following steps: at first (1), a 100 nm thick  $\text{Al}_{0.9}\text{Ga}_{0.1}\text{As}$  etch-stop layer is grown by molecular beam epitaxy (MBE) on a GaAs substrate, followed by the three superlens layers, of which the middle one (thickness  $d$ ) is doped GaAs and the outer two (thickness  $d/2$ ) are intrinsic. On top of the last intrinsic layer, gold objects are patterned by optical lithography, gold deposition, and lift-off processing (2). After that (3), the entire system is glued top-down by instant adhesive onto high-resistive silicon for the ease of handling. Then (4), the GaAs substrate is etched away by citric acid down to the  $\text{Al}_{0.9}\text{Ga}_{0.1}\text{As}$  etch-stop layer, which is finally (5) removed by concentrated hydrochloric acid (HCl), resulting in the final structure for the SNOM measurements (6). Samples with different thicknesses  $d$  (200 nm and 400 nm) and varying doping concentrations were prepared, an overview being given in Table 6.3.1.

Prior to the etching steps, the surface has to be cleaned in order to ensure a spatially homogeneous reaction with the material (if not doing so, roughening of the surface and slow



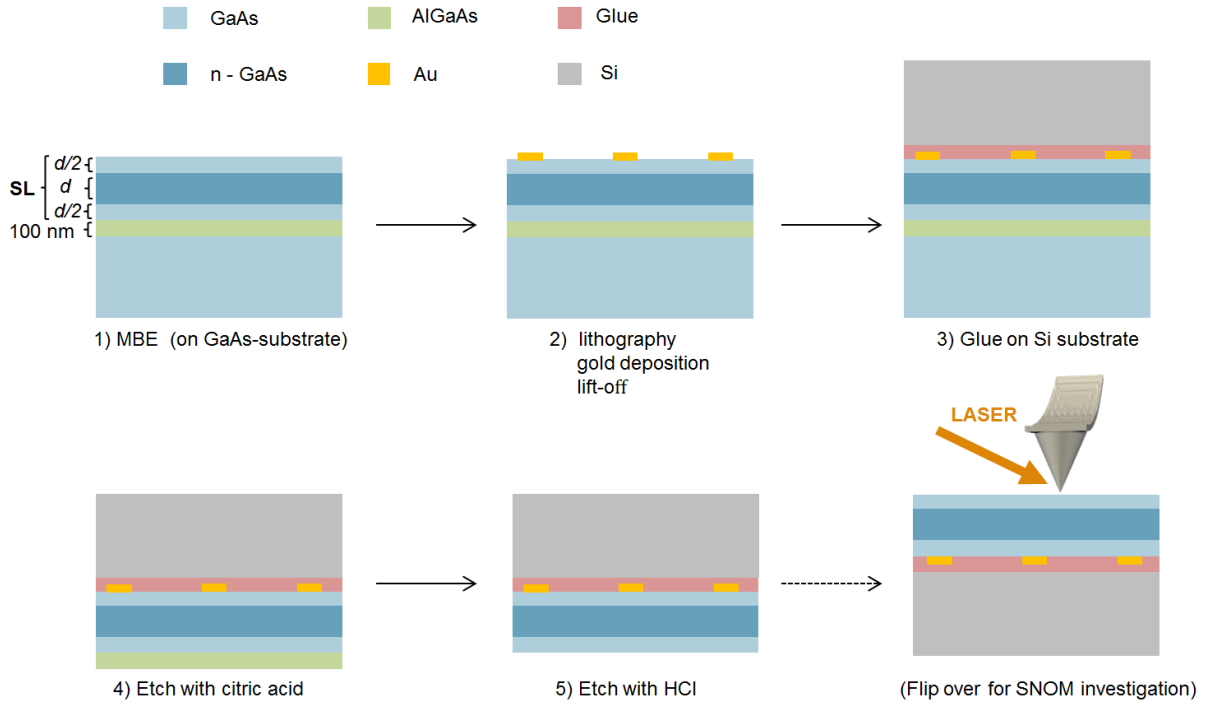


**Figure 6.1.1:** Preparation of the superlens (SL) samples. The thickness  $d$  of the n-doped GaAs layer is 200 and 400 nm for different samples, respectively.

onset of etching was observed). For that purpose, the glued sample is sequentially put into trichloroethylene, acetone, methanol and ethanol for 3 minutes each. Following each step, residues of the corresponding liquids are removed by deionized water (DI-H<sub>2</sub>O) and the sample is blown-dry by nitrogen gas. This is also done after each of the subsequent etching steps. Since GaAs is very fragile, we do not use an ultrasonic bath. After the treatment with the solvents, the native oxide layer is removed by dilute HCl (HCl:DI-H<sub>2</sub>O 1:5; dip for 10 seconds). Having obtained a clean and oxygen free surface, the GaAs substrate (nominal thickness  $500 \pm 25 \mu\text{m}$ ) is etched away by a 4:1 mixture of citric acid (citric acid powder:DI-H<sub>2</sub>O 1:1) and hydrogen peroxide (H<sub>2</sub>O<sub>2</sub>) down to the Al<sub>0.9</sub>Ga<sub>0.1</sub>As etch-stop. Due to the thickness of the substrate, this is done over night for about 18 hours. Here, a magnetic stirrer ensures a homogeneous distribution of the etchant and a flow across the sample surface, accelerating the etching process. The arrival at the Al<sub>0.9</sub>Ga<sub>0.1</sub>As layer can clearly be recognized by eye, the color changing from grey (GaAs) to brownish red<sup>1</sup>. Finally, the 100 nm thick etch-stop layer is removed by a dip into concentrated HCl, which takes about 10 seconds until the entire layer is etched away completely.

It should be mentioned that this removal is not occurring in a spatially homogeneous

<sup>1</sup>It was observed that the 100 nm thick Al<sub>0.9</sub>Ga<sub>0.1</sub>As layer withstands the citric acid - H<sub>2</sub>O<sub>2</sub> mixture for at least 1.5 hours.

manner. Therefore, some parts of the superlens are exposed to HCl for a longer period of time than other parts, which raises the question whether the total thickness  $2d$  of the superlens ( $2d = 400$  nm and 800 nm, respectively, depending on the sample) is constant all over the sample area. This is required to ensure reproducible and comparable results for different samples and different locations on one sample. To answer this question, we exposed the superlens to HCl to determine the etching rate of GaAs, obtaining an upper limit of 0.35 nm per second (after 20 minutes, the 400 nm thick superlens was not entirely removed). Considering the total etching time of the  $\text{Al}_{0.9}\text{Ga}_{0.1}\text{As}$  layer (10 seconds), the variations in the superlens thickness are expected to be smaller than 3.5 nm, which is small in comparison to the total thickness.

## 6.2 Topography

For the final sample structure, it turns out that the surface of the superlens layer is wrinkled on a scale that can be recognized by eye. These wrinkles appear after removing the GaAs substrate by wet etching (see step (4) in Figure 6.1.1). Here, the surface quality is connected both to the thickness of the superlens, being 400 and 800 nm, respectively, and lateral structure of the gold object below, which is either a periodic stripe-pattern (width 2  $\mu\text{m}$ , distance 10  $\mu\text{m}$ ) or a set of non-periodically distributed objects of different shapes and sizes (in the order of 10  $\mu\text{m}$ ). In Figure 6.2.1, images of the sample surface obtained by an optical microscope are depicted for three selected cases (see Section 8.1 for a sample overview), as well as height profiles measured by a profilometer and AFM scans of the topography at positions where near-field measurements (see Chapter 8) were obtained. As one can see, the surface exhibits height distortions in the  $\mu\text{m}$  range for all samples, which get smaller with increasing superlens thickness. This tendency was observed for numerous test samples. For the three depicted samples, the profiles of the profilometer cross the locations where SNOM measurements were performed, red arrows indicating these positions. As one can see in the optical micrograph, they are all located in a flat and well defined environment where reproducible results can be expected<sup>2</sup>.

Importantly, the gold objects are firmly connected to the superlens, since the gold deposition was performed onto the MBE grown GaAs layers (see Section 6.1) rather than on the Si carrier with subsequent covering the pattern by the superlens. Therefore, despite

---

<sup>2</sup>Note that in Figure 6.2.1b the vertical black lines in case of the samples with the striped pattern (left and middle image) and the rectangle on the non-periodically patterned sample (right) are related to boundaries between regions with different patterns. In proximity to these boundaries, the superlens layer is found to exhibit a particularly smooth surface. The same applies to regions around dirt particles (see dark spot in middle image of Figure 6.2.1b) that happen to be under the superlens layer.

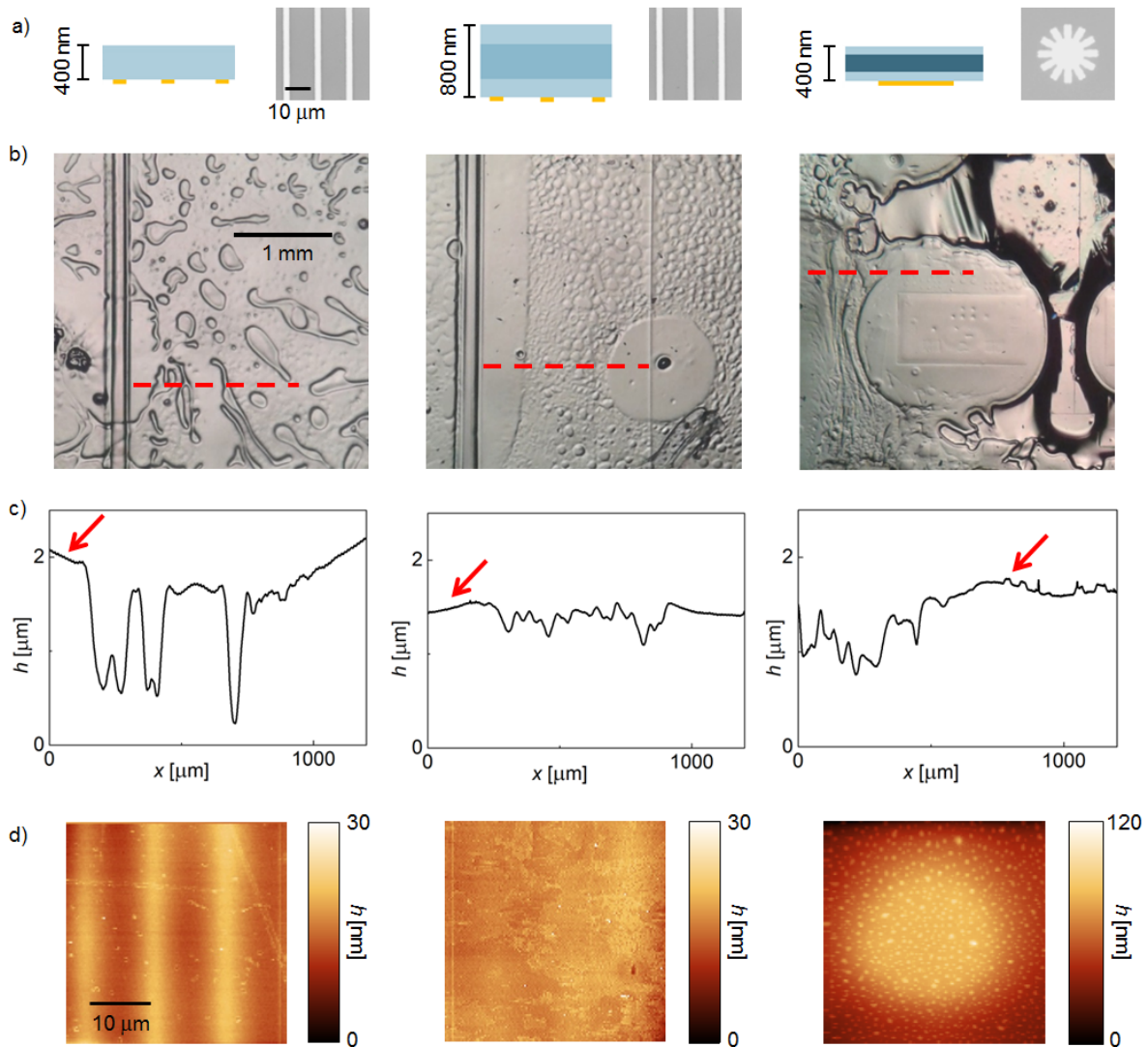


**Figure 6.2.1:** a) Schematic of various superlens samples (blue) and respective optical micrographs (grey) of gold objects to be imaged (taken before covered by the superlens). The differently doped middle layers of the superlens samples, indicated by different shades of blue, are not of interest in this section. b) Images of the sample surface obtained by an optical microscope. Red dashed lines indicate cross sections where height profiles were obtained by a profilometer, which are shown in c). Here, red arrows point to locations where SNOM measurements were performed. d) AFM scans at these locations.

the wrinkled surface, we can rely on the assumption that there is no gap between object and superlens, independent of the specific lateral position.

It has been demonstrated in Ref. [96] that surface roughness reduces the imaging capability of a superlens. In this case, the surface of a silver superlens provides small islands ( $\approx 100$  nm) with sharp edges at a height of about 4-5 nm, scattering the surface plasmon

modes that arise at the silver-air interface, which are responsible for the effect. In order to comment on the expected influence of surface roughness on the performance of the GaAs superlens, the two cases are compared on the scales of the respective resonance wavelength. The longer this wavelength, the less impact of a given roughness can be expected for sub-wavelength imaging. In case of silver, superlensing occurs at  $\lambda = 365$  nm, whereas it is expected at much longer wavelengths around  $\lambda = 20$   $\mu\text{m}$  for our samples, as we will see later (see Section 8.1). The AFM scans shown in Figure 6.2.1 cover an area of  $36 \times 36$   $\mu\text{m}^2$ , which was also the scan range for the near-field measurements. As can be seen, the gold objects give rise to related features in the topography of the samples with the thin superlens layers, the stripe pattern and the round shape of the disc (non-periodic object) being clearly recognizable. While in Ref. [96] superlensing is prohibited by a roughness of about  $\lambda/100$ , the height variations in our case are  $\lambda/2000$  (considering a superlensing wavelength of  $\lambda = 20$   $\mu\text{m}$ ) for the stripes and  $\lambda/300$  for the disc<sup>3</sup> only, which in particular for the former should result in significantly less scattering. In addition, in contrast to the silver superlens, no sharp edges are observed on our system, the height varying gradually over a distance much larger than the height change itself. As a conclusion, we do not expect scattering to impact the superlens performance in our experiment. Finally, please note that the thick superlens exhibits a flat surface almost free of signatures of the gold objects (see Figure 6.2.1d).

### 6.3 Electronic properties

In this section, the characterization of electronic properties of the GaAs superlens samples by both optical and transport methods is presented, which is the basis for the interpretation of the near-field results shown in Chapter 8. The various samples differ both in thickness  $d$  and doping concentration  $n_{\text{dop}}$  of the middle layer. As we saw in Section 5.3, the charge-carrier concentration  $n$  is not necessarily equal to  $n_{\text{dop}}$ . This in particular applies to values of  $n_{\text{dop}} \approx 10^{19}$   $\text{cm}^{-3}$ , which is the case in this work, necessitating a proper determination of  $n$  rather than relying on nominal values (which are given in Table 6.3.1). In the following, samples are denoted as "Sample  $i.j$ ", where  $i$  indicates a certain measured electron concentration and  $j = 1$  and  $j = 2$  represent the different thicknesses  $d = 200$  nm and  $d = 400$  nm, respectively. If  $d = 200$  nm is the only thickness at a given  $n$ , then  $j$  is omitted.

---

<sup>3</sup>Here, the origin of the eye-catching grains in the topography image (see Figure 6.2.1d) is unknown. Note that, in contrast to the island structure on the silver superlens, these do not impact the plasmon modes, which are in this case located below the surface at the GaAs/n-GaAs interface.

### 6.3.1 Fourier transform infrared spectroscopy

In order to determine the electronic properties of the doped GaAs layer, that is the free electron density  $n$  and the electron damping  $\gamma_{el}$ , Fourier transform infrared spectroscopy (FTIR) was performed in reflection geometry on the MBE grown samples prior to further processing (i.e. on the layer sequence GaAs/n-GaAs/GaAs/AlGaAs on GaAs substrate, see step 1 in Figure 6.1.1).

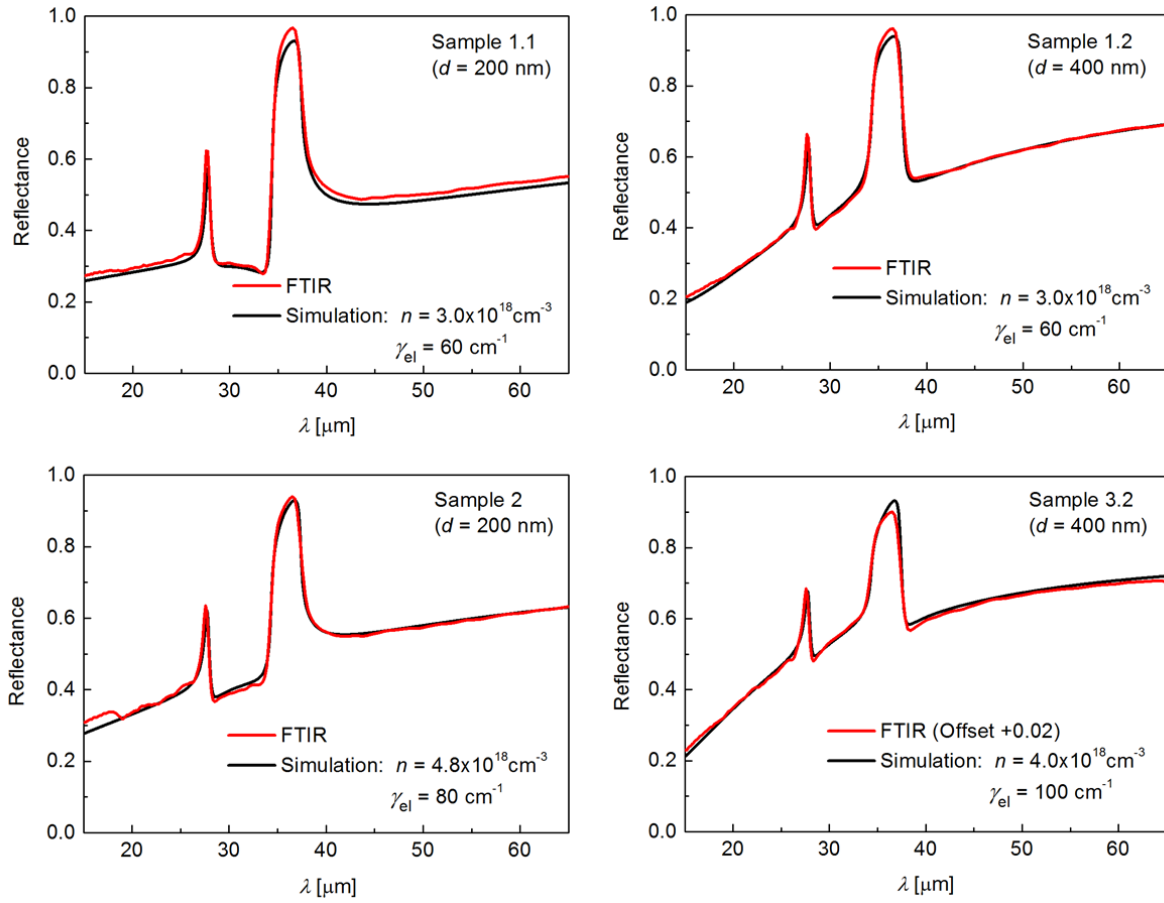


**Figure 6.3.1:** Reflectance of the layer sequence GaAs/n-GaAs/GaAs/AlGaAs on GaAs substrate for various doping concentrations  $n_{\text{dop}}$  (not shown) and thicknesses  $d$  of the doped layer (i.e. total thickness  $2d$  of the superlens). Simulation of the experimental results provides values of  $n$  and  $\gamma_{el}$ . All measurements were performed at room temperature.

FTIR is an efficient technique yielding power spectra  $\propto E^2(\lambda)$  in the infrared, where  $E(\lambda)$  is the magnitude of the electric field at the wavelength  $\lambda$ . Here, a Michelson interferometer is utilized to obtain the interferogram of an incident beam, which is numerically translated into the frequency spectrum by Fourier transformation. To measure the reflectance and transmittance of a sample, an incoherent global source is usually used as a radiation

source, providing broadband infrared radiation. This is also the case here. For the results presented, the spectrometer was evacuated to avoid signatures of atmospheric absorption.

The reflectance curves shown in Figure 6.3.1 are the power spectra of the reflected radiation normalized to a reference spectrum obtained with a gold mirror. At  $\lambda \approx 36 \mu\text{m}$  and  $28 \mu\text{m}$  pronounced maxima are observed for all samples, which is due to the Reststrahlen bands of GaAs and AlGaAs, respectively, associated with their respective phonon resonances. Apart from that, the spectral behavior is dominated by the Drude response of the samples, which is in turn described by the permittivity of the doped GaAs layer (see Section 5.2) since all other layers are intrinsic. Thus, electronic properties can be evaluated by fitting a Drude-Lorentz based multilayer reflectivity simulation (MATLAB) to the FTIR data,  $n$  and  $\gamma_{\text{el}}$  being the fit parameters. Here, the simulation considers the permittivity and thickness  $d$  of all layers, in particular of the conducting one. Both the experimental results<sup>4</sup> and the corresponding fits are shown in Figure 6.3.1, also providing the extracted values of  $n$  and  $\gamma_{\text{el}}$  (a summary is given in Table 6.3.1). As one can see, the overall reflectance increases with increasing  $n$  and  $d$ , which is in agreement with qualitative expectations.

### 6.3.2 Hall measurements

As a complementary characterization, Hall measurements were performed in so-called Van der Pauw geometry [97, 98]. This method allows one to determine both the longitudinal resistivity  $\rho_{xx}$  and the transverse resistivity  $\rho_{xy}$  (Hall resistivity) of a thin layer of known thickness and arbitrary shape, yielding the density and the mobility of the charge carriers. In case of this study, these are free electrons within n-doped GaAs layers with thicknesses of 200 and 400 nm, respectively.

A commercial Hall Measurement System HMS 9709 from Lake Shore was used for the investigations. The sample to be examined is of quadratic shape, which decreases the error due to an easy permutation of the measurement contacts. Therefore, pieces with the dimensions of about  $7 \times 7 \text{ mm}$  were prepared, provided with ohmic contacts by sputtering of gold onto the corners and mounting silver wires with silver glue on top. Measurements were performed at a fixed current of 0.1 mA. Just as for the FTIR measurements, samples were investigated after MBE growth, before patterning the surface with gold objects. The obtained data, measured at room temperature, are shown in Figure 6.3.2.

The Hall resistivity  $\rho_{xy}$  is a linear function of the magnetic field  $B$  applied perpendicular to the sample surface, which was varied in a range from -8T and 8T. The slope is given

<sup>4</sup>Note that a 2% offset is applied to the experimental data in case of Sample 3.2 to obtain better matching with the fit. Such a procedure is very common for FTIR measurements.

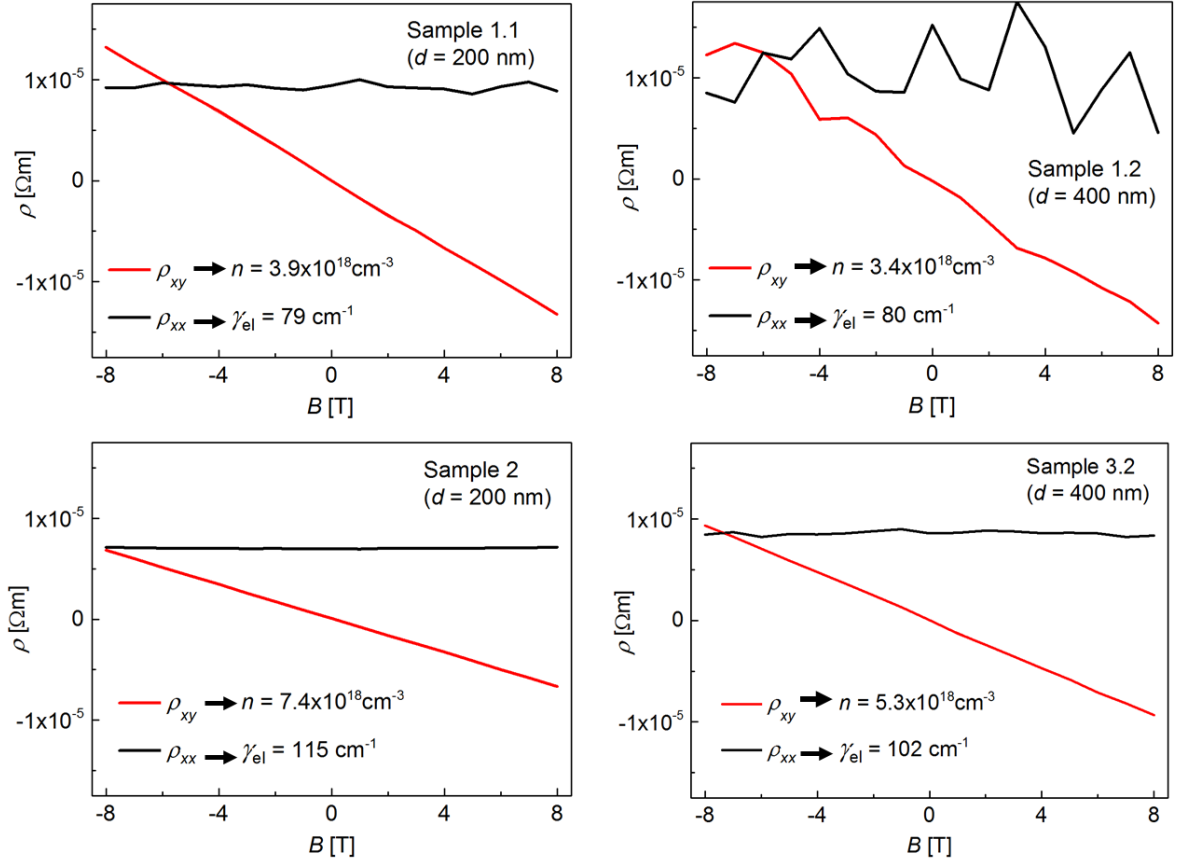


**Figure 6.3.2:** Longitudinal resistivity  $\rho_{xx}$  and transverse resistivity  $\rho_{xy}$  as a function of the magnetic field  $B$ , providing values of  $n$  and  $\mu$  according to Equations 6.3.1 and 6.3.2, respectively. Equations 5.3.1 and 5.3.2 are applied to obtain  $\gamma_{\text{el}}$  from  $\mu$ . All measurements were performed at room temperature.

by the Hall coefficient  $R_{\text{H}}$ , which is in turn a function of the charge-carrier density  $n$  (and the charge  $q$  of a single charge carrier, which is  $q = -e$  in this case), according to

$$\rho_{xy} = R_{\text{H}}B = \frac{r_{\text{H}}}{qn}B. \quad (6.3.1)$$

Here,  $r_{\text{H}}$  is the so-called Hall factor given by  $\langle\tau^2\rangle/\langle\tau\rangle^2$ , where  $\tau$  is the relaxation time and the brackets denote averaging. In most theoretical models, the value of  $r_{\text{H}}$  ranges between 1 and 2 and can be explicitly calculated for certain scattering processes [98], whereas there is also evidence for values smaller than 1 [99]. Usually,  $r_{\text{H}}$  is not known and set to 1, being aware that extracted values of  $n$  might not be precisely accurate due to this uncertainty. This is also done here. In addition, due to the high doping level, the Hall voltage is very low, which as well limits the accuracy.

Having determined  $n$  by linearly fitting  $\rho_{xy}(B)$ , the mobility  $\mu$  is deduced from the longitudinal resistivity  $\rho_{xx}$ , taking into account

$$\rho_{xx} = \frac{1}{qn\mu}. \quad (6.3.2)$$

Considering classical magnetotransport,  $\rho_{xx}$  is independent of  $B$ , which apparently is valid for our measurements (note, however, that this may not be true for all systems). Therefore, it was evaluated by applying a horizontal linear fit, reducing the statistical error. Finally, the electron damping  $\gamma_{\text{el}}$  can be calculated from  $\mu$  by applying Equations 5.3.1 and 5.3.2. Obtained values of  $n$  and  $\gamma_{\text{el}}$  are provided together with corresponding measurements in Figure 6.3.2 and in Table 6.3.1 for summary.

### 6.3.3 Summary and comments

In this section, the electronic properties of all samples are summarized. Values of  $n$  and  $\gamma_{\text{el}}$ , obtained both by FTIR and Hall measurements, are listed in Table 6.3.1. Moreover, the nominal doping concentration  $n_{\text{dop}}$  and the thicknesses  $d$  of the doped layers are given.

		S0	S1.1	S1.2	S2	S3.1	S3.2
$d$	[nm]	200	200	400	200	200	400
$n_{\text{dop}}$	[ $10^{18}\text{cm}^{-3}$ ]	0	5	5	5	15	15
$n^{\text{FTIR}}$	[ $10^{18}\text{cm}^{-3}$ ]	-	<b>3</b>	<b>3</b>	<b>4.8</b>	<b>(4)</b>	<b>4</b>
$\gamma_{\text{el}}^{\text{FTIR}}$	[ $\text{cm}^{-1}$ ]	-	<b>60</b>	<b>60</b>	<b>80</b>	<b>(100)</b>	<b>100</b>
$n^{\text{Hall}}$	[ $10^{18}\text{cm}^{-3}$ ]	-	3.9	3.4	7.4	-	5.3
$\gamma_{\text{el}}^{\text{Hall}}$	[ $\text{cm}^{-1}$ ]	-	79	80	115	-	102

**Table 6.3.1:** Properties of various superlens samples, SX abbreviating Sample X. The table lists the thickness of the doped layer  $d$ , the nominal doping concentration  $n_{\text{dop}}$ , the electron density  $n$  and the electron damping  $\gamma_{\text{el}}$  (obtained by FTIR- and Hall measurements, see Sections 6.3.1 and 6.3.2). FTIR values of Sample 3.1 are denoted in brackets since they were not directly measured but deduced from the FTIR investigations of the other samples (see text below).

As a remark, not all samples were produced in the same fabrication run<sup>5</sup>, giving rise to different growth conditions, with the MBE machine not being well calibrated in each case. Hence, the values of  $n_{\text{dop}}$  should merely be regarded as a rough indication of the

<sup>5</sup>To be more precise, there were two growth runs: one for Sample 2, and one for all other samples.



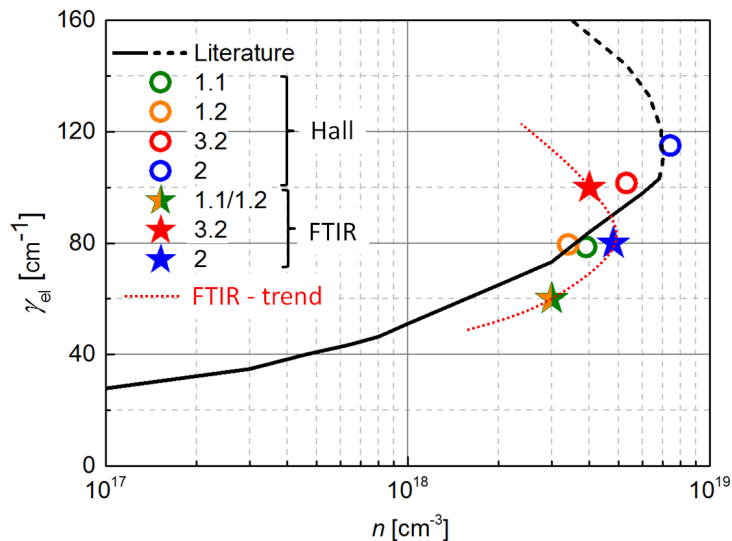


**Figure 6.3.3:** Electron density  $n$  and the electron damping  $\gamma_{\text{el}}$  obtained by both FTIR- and Hall measurements. As a comparison, the black curve depicts  $\gamma_{\text{el}}(n)$  extracted from drift mobility measurements [94] (see Section 5.3). For  $n_{\text{dop}} > 7 \times 10^{18} \text{cm}^{-3}$  autocompensation of  $n$  is considered [93] (dashed line). The red dotted line indicates the trend of the FTIR results.

actual doping concentration. There are two samples with nominal values as large as  $n_{\text{dop}} = 1.5 \times 10^{19} \text{cm}^{-3}$ , which, as we saw in Section 5.3, is expected to cause undesired autocompensation of free electrons. However, we were not aware of this issue at the time of sample preparation. In addition to the overview table, Figure 6.3.3 provides a graphic depiction of the experimentally obtained  $\gamma_{\text{el}}(n)$ , including a comparison to expectations based on values from literature (see Section 5.3). As can be seen, there is general agreement, however the deviations between the various values are not negligible, as discussed in the following.

For two reasons, we rely on values obtained by FTIR rather than by Hall measurements. First, the FTIR results are obtained in a spectral range that includes the expected superlensing wavelength. Therefore, they provide *ac* values of  $\gamma_{\text{el}}$  describing the damping of plasma oscillations, which are directly linked to the superlensing effect (see Section 3.3). In contrast,  $\gamma_{\text{el}}$  extracted from Hall investigations is related to the electron scattering time  $\tau$  in a *dc* current. Second, as we discussed in Section 6.3.2, the accuracy of the Hall measurements is impacted both by small Hall voltages due to high electron densities and the unknown Hall factor  $r_{\text{H}}$ , which is involved in the data evaluation. Here, note that  $r_{\text{H}} = r_{\text{H}}(n)$ , as for instance demonstrated for doped Si in Ref. [100]. Hence, the Hall data only serve as a rough validation of the FTIR investigations.

Since the literature based curve  $\gamma_{\text{el}}(n)$  in Figure 6.3.3 as well relies on *dc* transport

measurements [94], precise quantitative agreement with the FTIR investigations can also not be expected in this case. In addition, absolute values depend on the specific MBE growth conditions, which are certainly different regarding our samples on the one hand and literature based values on the other hand. Nevertheless, the FTIR results agree with qualitative expectations, providing the expected reverse C-shape of  $\gamma_{\text{el}}(n)$  at large values of  $n$ , which arises from the previously mentioned autocompensation of free electrons. In particular, the extracted electron density of Sample 3.2. is just about one third of the nominal doping concentration, which can be attributed to this effect.

For Samples 1.1 and 1.2, identical results are obtained, which was expected since they were grown in two subsequent MBE growth runs with the same intended doping level. Here, the only difference is the layer thickness  $d$ . This accurate match is remarkable, as it implies that for Sample 3.1, which was not investigated by FTIR, the same values as for Sample 3.2 can be assumed (in the table, values of Sample 3.1 are denoted in brackets). Furthermore it confirms that the fit function used for the determination of  $n$  and  $\gamma_{\text{el}}$  also considers  $d$  correctly.

In Section 8.1, values obtained by FTIR measurements are inserted to simulate the superlensing behavior of the samples. In Table 6.3.1, the numbers of interest are highlighted by applying bold font.

## 6.4 Exclusion of resonant artifacts

The objective of this work is to investigate the properties of a GaAs superlens, providing resonant enhancement of evanescent waves. As we will see later in Section 8.1, this is expected to occur at wavelengths between  $\lambda = 17 \mu\text{m}$  and  $23 \mu\text{m}$  for the various samples, these values being based on the electronic characterization presented in the present chapter. To avoid misinterpretation of measured signals, it is important to exclude resonant phenomena in this spectral region caused by constituents of the samples other than the superlens structure itself.

For the ease of handling, the layered system is glued onto a semi-insulating silicon substrate by instant adhesive. An increase of the reflectance of silicon and absorption lines of the glue could lead to increased and decreased near-field signals, respectively, which might mistakenly be attributed to the superlens. As can be seen in Figure 6.4.1a, neither is the case in the spectral range of interest. On the one hand, the substrate provides a rather constant reflectance of about 35%. On the other hand, absorption by the glue was not observed at wavelengths longer than  $\lambda = 12 \mu\text{m}$ , in contrast to shorter wavelengths. This is seen by comparing the transmission through a thin layer of glue ( $\sim 3 \mu\text{m}$ ) on silicon

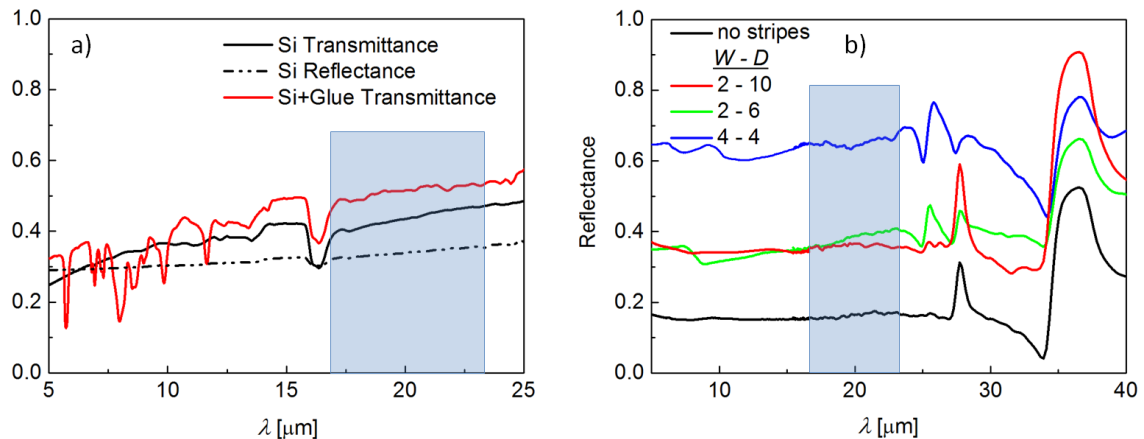


**Figure 6.4.1:** (a) Reflectance of the silicon substrate and transmission with and without a  $\sim 3\mu\text{m}$  thick layer of glue (instant adhesive). (b) Reflectance of gold stripes on the layer sequence GaAs/AlGaAs on GaAs substrate for various stripe widths  $W$  and distances  $D$  (period  $W + D$ ), indicated in  $\mu\text{m}$  in the figure legend. The region of interest for the SNOM investigations is highlighted in blue.

to the transmission through silicon without glue (the absorption line at  $\lambda \approx 16.5 \mu\text{m}$  is due to a two-phonon absorption in silicon [101, 102]). Note that the larger transmission in presence of the glue can be attributed to Fabry-Pérot oscillations caused by this layer.

Another essential constituent of the samples are the gold objects, which are imaged through the superlens. For most investigations presented in this work, this is a periodic pattern of stripes. On the one hand the periodicity eases the experiment, since investigations can be performed at arbitrary positions of the samples without having to search for a particular location. On the other hand, however, periodic structures can cause resonant interference phenomena, which are unwanted for above mentioned reasons. Therefore, the reflectance of various patterns (gold stripe width  $W$ , distance  $D$ ) was measured after the lithography step on a reference structure (i.e. gold stripes on the layer sequence GaAs(400 nm)/AlGaAs(100 nm) on GaAs substrate; no doped layer). This is shown in Figure 6.4.1b. An unpatterned sample is also displayed for comparison (note the difference to the measurements shown in Figure 6.3.1, which arises from the lack of free electrons in this case, reducing the reflectance). As expected, adding gold stripes enlarges the overall reflectance in each case. In addition, also the detailed spectral behavior strongly varies. Obviously, the stripes induce peaks and dips in the reflectance, which depend both on  $W$  and  $D$ . For the cases depicted in blue ( $W = D = 4 \mu\text{m}$ ) and green ( $W = 2 \mu\text{m}$ ,  $D = 6 \mu\text{m}$ ), a pronounced feature arises at  $\lambda \approx 25 \mu\text{m}$ . This corresponds to  $\lambda \approx 8 \mu\text{m}$  in GaAs (considering  $n_{\text{GaAs}}^* = \sqrt{\varepsilon_{\text{GaAs}}} \approx 3$  at this frequency), which equals the periodicity  $W + D$  of

these two patterns. Following the same argumentation, the pattern with a periodicity of  $12\ \mu\text{m}$  gives rise to an increase of reflection at  $\lambda \approx 32\ \mu\text{m}$  ( $n_{\text{GaAs}}^* \approx 2.6$  at this frequency<sup>6</sup>), as can be seen by comparison with the sample without stripes. This pattern ( $W = 2\ \mu\text{m}$ ,  $D = 10\ \mu\text{m}$ ) was chosen for the investigations of the superlens, since the spectrum is least distorted in the range of interest.

---

<sup>6</sup>Note that the value of  $\varepsilon_{\text{GaAs}}$  and hence of  $n_{\text{GaAs}}^*$  drops due to a phonon resonance, see Figure 5.2.1.



# 7 Experimental details

*In this chapter, the experimental methods for the s-SNOM investigation are introduced. Exploiting the tip of an atomic force microscope (AFM) as near-field probe, this technique allows one to control the probe-sample distance on a nanometer scale by recording the movement of a cantilever, which is deflected under the influence of the short-range force between tip and sample. As a radiation source we apply the free-electron laser FELBE, which is continuously frequency tunable over a large infrared spectral region, using relativistic electrons in a periodic magnetic field as adjustable gain medium. The main aspects of the setup and its adjustment are introduced. The scattered near-field is detected in a direct, non-interferometric manner. Here, due to the short coherence length of the FELBE radiation, the signal is not disturbed by interference with far-field background, resulting from scattering at structures surrounding the probe.*

## 7.1 AFM to probe the near-field

In scattering-type scanning near-field optical microscopy (s-SNOM), a nm-sized particle acting as a light-scattering probe is placed in close proximity to the sample, with a laser serving as an intense radiation source in most cases. The scattering at the probe is modified by the near-field interaction with the sample (see Chapter 4), which occurs on a scale of the curvature radius  $a$  of the probe's apex in both vertical and lateral direction. On the one hand, this allows for extracting the local permittivity with a spatial resolution of about  $a$ , independent of the applied radiation wavelength  $\lambda$ , as long as  $a \ll \lambda$ . On the other hand, it requires placing the probe at a distance  $h < a$  to the sample. In our case, this is enabled by atomic force microscopy (AFM), where the short range mechanical force between a sharp tip and the sample is exploited to control their separation on a nanometer scale [69, 103]. Typically,  $a$  is in the range of about 10 nm, providing deep subwavelength SNOM resolution for both the visible ( $\lambda \approx 380 - 780$  nm) and the infrared<sup>1</sup>

---

<sup>1</sup>Note, however, that the intensity of the scattered light is proportional to  $1/\lambda^4$  (see Equation 4.2.14), drastically reducing the SNOM signal at long wavelengths. Also, photodetectors operating in the far-infrared are less efficient than at shorter wavelengths, making this spectral region very challenging for SNOM investigations.

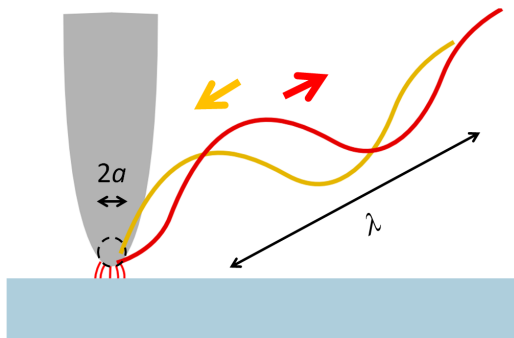


**Figure 7.1.1:** AFM tip as near-field probe: incoming radiation (orange) with a wavelength  $\lambda$  induces near-field coupling between tip and sample on a scale of the tip radius  $a$ . Phase and amplitude of the scattered light (red) depend on the local permittivity of the sample at a spatial resolution of about  $a$ , independent of  $\lambda$ .

( $\lambda \approx 0.78 - 1000 \mu\text{m}$ ) spectral region. By scanning the sample in lateral direction with respect to the tip, an optical image is obtained by recording the scattered light at each position.

During a SNOM scan, it is crucial to keep the distance  $h$  between the sample and the tip constant, since the scattering behavior strongly varies with  $h$ . While the position of the tip is fixed, both the lateral ( $x, y$ ) and the vertical ( $z$ ) displacement of the sample are realized by piezoelectric scanners. Here, scanning the tip instead of the sample, which is also a common approach in AFM, is disadvantageous in s-SNOM, since this would require tracking the laser beam which is illuminating the tip. The voltage applied to the  $z$ -scanner, ensuring constant  $h$ , is interpreted as the topography of the sample surface and is recorded simultaneously to the near-field image. In AFM, the probing tip is located at the end of a cantilever. There are several operational modes, each of them exploiting the motion of the cantilever induced by the force between tip and sample in order to control the tip-sample distance  $h$ . The mechanical interaction is qualitatively well described by the Lennard-Jones potential  $V_{LJ}$  [104], which takes into account long-range attractive van der Waals and short-range repulsive covalent forces between electrically neutral counterparts. It can be written as

$$V_{LJ}(h) = 4\tilde{A} \left[ \left( \frac{\tilde{B}}{h} \right)^{12} - \left( \frac{\tilde{B}}{h} \right)^6 \right], \quad (7.1.1)$$

where the parameters  $\tilde{A}$  and  $\tilde{B}$  depend, amongst others, on the material and geometry of

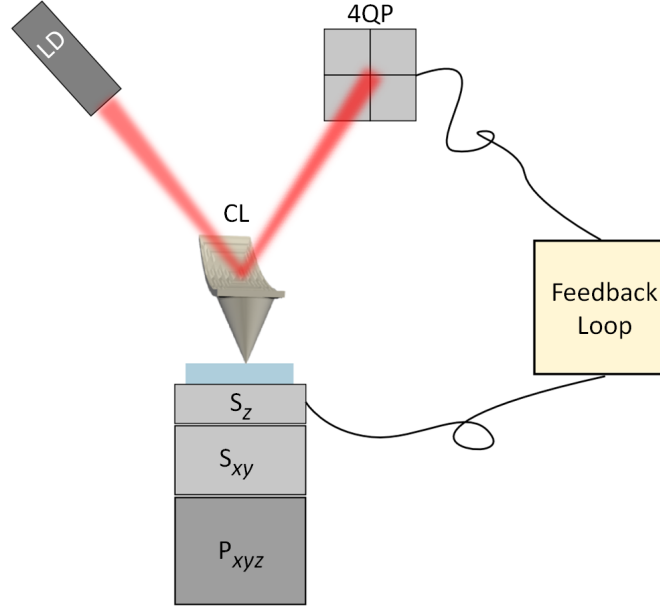


**Figure 7.1.2:** AFM operation: the cantilever (CL) motion is recorded by the reflection of a laser diode's (LD) beam onto a four-quadrant photodiode (4QP), providing the input signal of a feedback loop that ensures constant distance  $h$  between tip and sample. To this end, a voltage is applied to a piezoelectric scanner ( $S_z$ ) in vertical direction. Lateral displacement is also enabled by scanners  $S_{xy}$ . Piezoelectric slip-stick actuators ( $P_{xyz}$ ) allow for coarse positioning of the sample.

tip and sample. The corresponding force  $F_{LJ}$  is given by

$$F_{LJ}(h) = -\frac{\partial V_{LJ}}{\partial h}. \quad (7.1.2)$$

The cantilever bends under the influence of this force as the tip approaches the sample. In this work this bending is recorded by the method of beam deflection. To this end, the visible beam of a laser diode is focused onto the backside of the cantilever, where it is reflected onto a four-quadrant photodiode (see Figure 7.1.2). The difference of the photocurrents generated in the top quadrants and the bottom quadrants (top-minus-bottom signal) corresponds to a certain deflection of the cantilever and therefore to a certain  $h$ , which is kept constant during a scan by employing the diode signal as the input signal of a control circuit acting on the voltage applied to the  $z$ -scanner. This mode is referred to as the *static mode*. On the other hand, the cantilever can be excited by piezoelectric shakers to oscillate close to its resonance frequency, with this resonance being shifted by the force gradient between tip and sample. This *dynamic mode* is applied in s-SNOM, since the periodic modulation of  $h$  allows for suppressing background signals due to unwanted



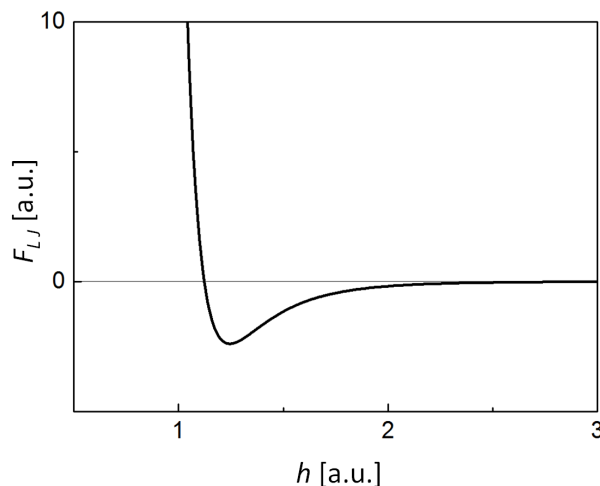


**Figure 7.1.3:** Force  $F_{LJ}$  between tip and sample as a function of their distance  $h$ , derived from the Lennard-Jones potential  $V_{LJ}$ .

scattering events (see Section 4.4). The resonance frequency  $f_0$  of the cantilever is given by [105]

$$f_0 = \frac{1}{2\pi} \sqrt{\frac{D}{m_{eff}}}, \quad (7.1.3)$$

where  $D$  is the spring constant and  $m_{eff}$  the effective mass of cantilever and tip. In the present work, silicon cantilevers with a thickness  $t = 7 \mu\text{m}$ , width  $w = 38 \mu\text{m}$  and length  $l = 225 \mu\text{m}$  are applied. The tip consists of silicon as well. For this geometry, the spring constant is given by [106]

$$D = \frac{Et^3w}{4l^3}, \quad (7.1.4)$$

where  $E$  is Young's modulus of silicon. This provides a nominal resonance frequency of  $f_0 = 190 \text{ kHz}$ , which is much higher than the frequency of undesired vibrations (building vibrations, acoustic waves) potentially disturbing the measurement. In proximity to the sample,  $f_0$  is shifted by the gradient of the force  $F_{LJ}$  according to

$$f_0 = \frac{1}{2\pi} \sqrt{\frac{D - \frac{\partial F_{LJ}}{\partial h}}{m_{eff}}}. \quad (7.1.5)$$

While the long range attractive forces barely impact the oscillation, the short range repulsive forces lead to an increase of  $f_0$  induced by the large gradient  $\partial F_{LJ}/\partial h < 0$  (see Figure 7.1.3). If the excitation frequency is kept constant, this shift of  $f_0$  gives rise to a reduced amplitude of the cantilever oscillation, which is the parameter to control  $h$  in this

*amplitude-modulated (AM-)* version of the dynamic mode, also often referred to as *tapping mode*. Alternatively,  $f_0$  itself can serve as the control parameter, where the excitation frequency is tracking the resonance. This is called *frequency-modulated (FM-)* AFM, allowing for an almost constant oscillation amplitude due to an additional controller. Therefore, it is the preferred AFM mode for SNOM measurements, since the scattering condition is kept constant. In contrast, when applying AM-AFM, the amplitude necessarily changes at topographical steps before the control circuit adjusts the distance to the sample. This gives rise to variations of the optical signal, which might erroneously be interpreted as near-field contrast. However, the samples of interest in this work are lacking any relevant topographical features related to such artifacts. Thus we apply AM-AFM, providing a more stable performance than FM-AFM with our setup.

For the present study, a home-built AFM [107] is applied, designed to provide easy optical access to the tip-sample junction. The sample is moved by commercial piezoelectric scanners in all three dimension, providing a nominal scan range of  $40 \times 40 \times 4.3 \mu\text{m}^3$  ( $x \times y \times z$ ). For a coarse positioning of the sample, the scanners are placed on a stack of piezoelectric slip-stick actuators, offering a range of  $5 \times 5 \times 5 \text{ mm}^3$  at a precision of at least 50 nm. As already mentioned above, the AFM tip is located at the end of a cantilever, which in turn is attached to the microscope by an alignment chip, allowing for the exchange of probes with high spatial accuracy. This is especially relevant for SNOM studies, where the position of the tip with respect to the incoming laser beam has to be kept constant.

A final remark is dedicated to the AFM-tip, which is of course of critical importance both for the AFM and the SNOM performance, since it is the apex of the tip which mechanically and optically interacts with the sample. The spatial resolution of both the topography and the near-field image, which are recorded simultaneously, is in the order of the curvature radius of the apex. In SNOM, a sharp tip comes with a decrease of the signal strength, since the scattering amplitude is reduced. Hence, a compromise has to be found, depending on the detector sensitivity and the structure size to be investigated, for instance. In this work, we apply silicon tips coated by a 25 nm thick double layer of chromium and platinum iridium<sup>2</sup> (Pt-Ir5), providing a radius of about 50 nm. In contrast to a pure silicon tip, this coating ensures a spectrally flat polarizability in the infrared (see Equation 4.2.17), which is desired for the investigation of wavelength dependent near-field phenomena, since spectral changes can exclusively be attributed to the sample. Also, Pt-Ir5 is mechanically very stable compared to other metal coatings (e.g. gold), being of particular importance in s-SNOM where a change of the tip geometry would give rise to a

---

<sup>2</sup>NANOSENSORS, PPP-NCLPt

change of near-field signal.

## 7.2 Radiation source FELBE

In this work, the spectral behavior of a plasmonic superlens was investigated in the infrared spectral region. To this end, the free-electron laser FELBE<sup>3</sup> at the Helmholtz-Zentrum Dresden-Rossendorf was applied as a radiation source, providing intense narrowband radiation that is continuously tunable within a large wavelength range.

A conventional LASER (Light Amplification by Stimulated Emission of Radiation) makes use of stimulated transitions between quantized states of a gain medium at fixed energies, such as bound electrons in gas- or solid-state lasers. In contrast, as the name suggests, free electrons represent the laser medium of a free-electron laser (FEL) [108], where lasing arises from the wiggling motion of a relativistic electron beam. Here, the extraordinary attribute of an FEL is its wide spectral tuning range, which makes it highly valuable for spectroscopic studies. The concept of this kind of laser can be understood in purely classical terms [109], as shortly introduced in the following. The main components are schematically depicted in Figure 7.2.1 (note that there are designs that differ from the example presented here, however they follow the same principle). A beam of electrons with velocity  $v$ , provided by an electron accelerator, is injected into a so called undulator, which consists of an array of alternately poled permanent magnets generating a spatially periodic magnetic field  $\mathbf{B}$  with period  $\lambda_u$ ,

$$\mathbf{B} = B\mathbf{e}_B \sin \frac{2\pi z}{\lambda_u}, \quad (7.2.1)$$

where  $\mathbf{e}_B$  is the unit vector along the axis of the magnets and  $z$  is the direction along the beam. The arising Lorentz force induces an oscillatory motion of the electrons transverse to  $B$  while moving through the undulator, giving rise to synchrotron radiation. Due to their relativistic speed, i.e. almost the speed of light  $c$ , this emission occurs in forward direction only (from the laboratory frame of observation, other directions would result in electrons and photons moving away from each other at a speed greater than  $c$ ). The wavelength  $\lambda_s$  of the spontaneously emitted light is given by

$$\lambda_s = \frac{1 + K^2}{2\gamma^2} \lambda_u, \quad (7.2.2)$$

---

<sup>3</sup>Free-electron laser at ELBE (Electron Linear accelerator for beams with high Brilliance and low Emission)

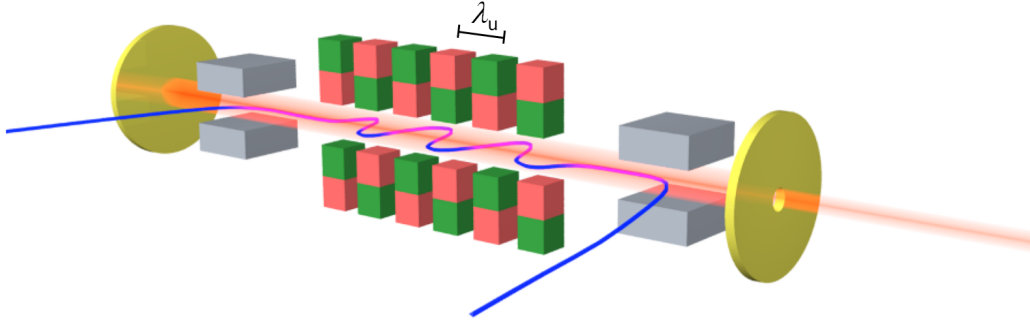


**Figure 7.2.1:** Scheme of a free-electron laser (FEL). Dipole magnets (gray) direct a relativistic electron beam (blue) into an *undulator*, consisting of magnets (red/green) that provide an altering magnetic field (period  $\lambda_u$ ). The oscillatory motion of the electrons gives rise to synchrotron radiation, where light amplification is obtained in an optical cavity (mirrors depicted in gold, one of them providing a small hole for radiation output).

with the Lorentz factor

$$\gamma = \frac{1}{\sqrt{1 - \frac{v^2}{c^2}}} \quad (7.2.3)$$

and the undulator parameter

$$K = \frac{eB\lambda_u}{2\pi m_0 c}, \quad (7.2.4)$$

where  $-e$  and  $m_0$  are the electron charge and rest mass, respectively. Note that typically  $K$  is in the order of one, and hence the emitted  $\lambda_s$  is in the order of the undulator period  $\lambda_u$  divided by  $\gamma^2$ . With  $\lambda_u$  being fixed,  $\lambda_s$  can be tuned by both altering the electron velocity  $v$  and the magnetic field  $B$ , where the latter is realized by changing the gap of the undulator. The spectral linewidth of the spontaneous emission is determined by the number of undulator periods  $N_u$ , narrowing with increasing  $N_u$ . With  $\omega_s = 2\pi/\lambda_s$ , the spectral intensity distribution is given by

$$I(\omega) \propto \left( \frac{\sin(\pi N_u (\omega - \omega_s)/\omega_s)}{\pi N_u (\omega - \omega_s)/\omega_s} \right)^2. \quad (7.2.5)$$

According to this, a linewidth of about 1% can be expected for  $N_u = 100$  [107].

As considered so far, the light emitted by the arbitrarily positioned electrons is incoherent due to the random phases of the respective waves. However, coherence arises from an effect called *microbunching*: If a feedback is provided by an optical cavity (see Figure 7.2.1), the undulator acts as a gain medium, where the interaction between electrons and the radiation

field yields a redistribution of the charge carriers. This leads to stimulated emission of photons. In particular, the ponderomotive force acting on the transverse motion of the electrons results in a formation of bunches at a distance of the radiation wavelength, which are referred to as microbunches. Hence, the photons emitted by all electrons are in phase with each other, enabling coherent light amplification. It has been found that this amplification (or gain) is proportional to the derivative of the spontaneous emission line (see Equation 7.2.5), obviously resulting in zero gain for the center wavelength  $\lambda_s$ . In contrast, amplification occurs for slightly longer wavelengths, while shorter wavelengths are absorbed by the electrons.

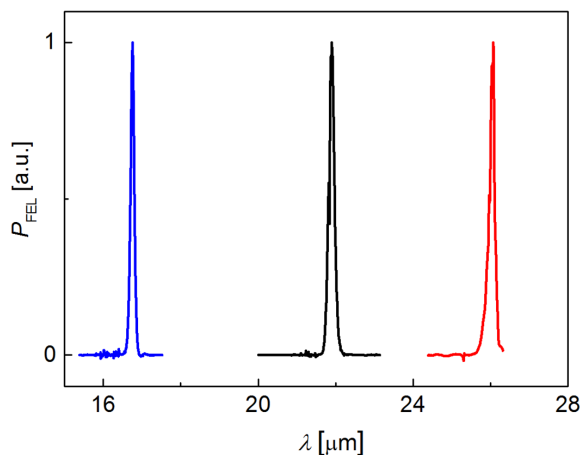


**Figure 7.2.2:** Exemplary emission lines of FELBE. Normalized laser power  $P_{\text{FEL}}$  as a function of the radiation wavelength  $\lambda$  depicted for various settings of operation.

The free-electron laser FELBE consists of two undulators with different undulator periods  $\lambda_u$ , called U27 and U100, where the numbers indicate  $\lambda_u$  in units of mm. Note that both undulators cannot be operated at the same time. Here, U27 provides radiation wavelengths between  $4 \mu\text{m}$  and  $22 \mu\text{m}$ , while U100 covers the range from  $18 \mu\text{m}$  to  $250 \mu\text{m}$ . Both undulators were applied for the near-field investigations in this work, where Figure 7.2.2 depicts exemplary emission lines obtained when performing the near-field measurements presented in Chapter 8. The polarization of the laser light is determined by the sinusoidal motion of the electron beam, giving rise to linear polarization with horizontal orientation in case of FELBE. For the SNOM measurements, it is rotated by  $90^\circ$  on the optical table. Due to a pulsed operation of the electron accelerator ELBE, which delivers the electron beam, the infrared radiation of FELBE is also pulsed. Here, the rate is fixed to 13 MHz, related to a cavity length of 11.53 m. Since this is much faster than the oscillation frequency of the AFM tip (i.e. the SNOM probe) at which the near-field signal is

demodulated in our measurements, the laser beam can be regarded as continuous in this work. By a system of mirrors, it is forwarded from the FEL to the laboratory housing the SNOM setup, which will be described in the next section.

### 7.3 *s*-SNOM setup and adjustment

The infrared electromagnetic radiation of the FEL, invisible to the human eye, has to be focused onto the scattering AFM tip, whereupon the scattered near-field is directed to a liquid nitrogen cooled mercury cadmium telluride (MCT) detector<sup>4</sup>. To this end, a visible alignment laser (red,  $\lambda = 633$  nm) is applied, following the same path as the FEL beam. A simplified scheme of the optical setup is shown in Figure 7.3.1. In order to ensure suitability for the whole infrared spectrum of the widely tunable FEL, it is solely based on reflection optics instead of diffracting elements (e.g. lenses), providing close to 100% reflectivity throughout this spectral region. Plane and parabolic mirrors with gold coatings are utilized as well as a gold coated defined edge of a silicon wafer, which is applied as a beam splitter that reflects half of the profile of the incoming beam.

The beam paths of alignment laser and FEL are adjusted by two independent pairs of plane mirrors, allowing for both a parallel shift and a change of direction for each case. In Figure 7.3.1, these dedicated mirrors are labeled by hand shaped symbols depicted in the same colors as the associated laser beams. One of these mirrors being on a flip mount enables the two beam paths to merge after they have passed the adjustment mirrors. Here, two iris diaphragms at a large distance ensure collinearity. Half of the laser beam passes the beam splitter to a powermeter, recording the laser power during a SNOM measurement for signal normalization. The other half is directed to a parabolic mirror (diameter 2 inch, focal length 4 inch), which focuses the laser beam onto the tip-sample junction at an angle of  $65^\circ$  against the sample surface normal. The same parabolic mirror collimates the backscattered light, half of it passing the beam splitter and being refocused on the active area of the MCT detector, which generates a voltage that is processed by a lock-in amplifier (see Section 4.4 regarding the modulation of the scattered near-field by the oscillation of the AFM tip).

The adjustment of the FEL beam is carried out in four steps. First, the visible alignment laser, passing the two iris diaphragms, is focused onto the AFM tip. To make sure a Gaussian profile in the focus with well defined polarization, the flat back surface of the parabolic mirror needs to be perpendicular to the incoming beam. Fine tuning of the position of the focus is enabled by a piezo stage carrying the mirror, providing an accuracy

---

<sup>4</sup>InfraRed Associates, Inc; FTIR-22-2-0

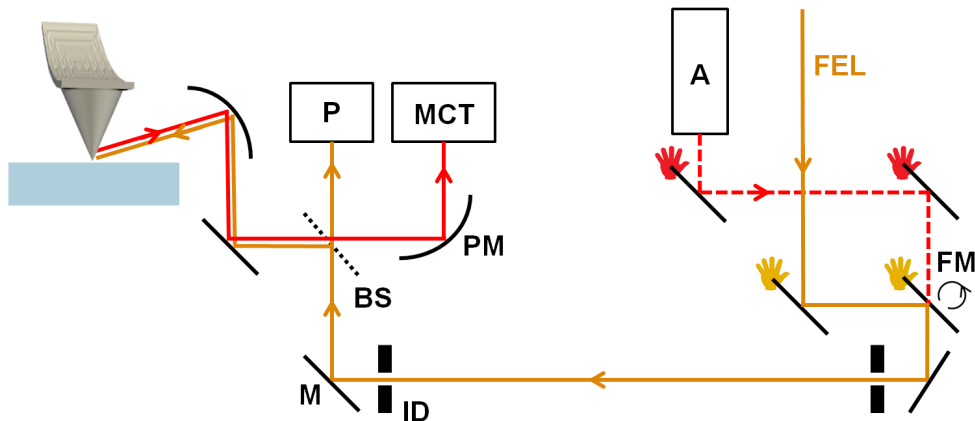


**Figure 7.3.1:** Simplified scheme of the s-SNOM setup comprising following elements: plane gold mirrors (M), plane gold mirror on flip mount (FM), parabolic gold mirrors (PM), iris diaphragms (ID), beam splitter (BS), powermeter (P) and MCT detector. Radiation sources: alignment laser (A, red dashed line) and free-electron laser FEL (orange line). Hand shaped symbols depicted in the respective colors label the mirrors exploited for beam path adjustment. The red solid line represents the scattered near-field.

of about  $1 \mu\text{m}$  in all three dimensions. The AFM tip gives rise to a shadow within the laser profile behind the focus, being largest in case of the focus meeting the tip, which is desired (if the focus is smaller than the tip, a diffraction pattern can be seen). The adjustment laser is also exploited for adjusting the position of the detector behind the second parabolic mirror. As a second step, the FEL beam is directed through the iris diaphragms with the help of a pyroelectric camera, which is applied to image the beam directly behind each of the diaphragms. The FEL beam now should be collinear to the adjustment laser, being focused at the tip of the AFM. This can be checked by recording the lock-in signal at the tip oscillation frequency, arising since the cantilever is periodically moving through the focus, which modulates the scattered light reaching the detector. Next, the tip is brought into contact with the sample. Due to the near-field interaction, a lock-in signal at higher harmonics of the oscillation frequency (see Section 4.4) arises if the apex of the tip is illuminated. This signal is optimized by fine tuning the position of the focus. Typically, the second and third harmonic signals,  $NF_{2\Omega}$  and  $NF_{3\Omega}$ , are chosen as parameters for that purpose, where the latter comes with the advantage of being less impacted by background radiation, however also with the disadvantage of significantly reduced signal strength. Finally, the dependence of  $NF_{2\Omega}$  and  $NF_{3\Omega}$  to the distance  $h$  between tip and sample (retract curves) is recorded. As we saw in Section 4.4, a nonlinear decay to zero on the length scale of the tip radius ( $\approx 50 \text{ nm}$ ) can be expected if background

signals are suppressed efficiently, verifying the quality of the FEL alignment. Typically, a decay within 100 nm is an indicator for a near-field signal with negligible background contribution (see Section 8.5).

## 7.4 Direct detection at FELBE

The s-SNOM results presented in this work, exploiting the free-electron laser FELBE as a radiation source, are obtained by direct, non-interferometric detection. In Section 4.4, we discussed that in this case the signal  $NF_{n\Omega}$  is given by

$$NF_{n\Omega} \propto E_{bc}s_n \cos(\varphi_{bc} - \varphi_n), \quad (7.4.1)$$

where  $E_{bc}$  is the background field scattered at the sample surface and  $s_n e^{i\varphi_n}$  arises from a Fourier expansion of the tip apex related scattering coefficient  $se^{i\varphi}$  modulated by the probe oscillation, which yields the information about the local near-field. As one can see, the signal strength is in particular impacted by phase changes of the two fields, where  $\varphi_{bc}$  is unknown.

In general, the interference with background radiation has two consequences: First, a determination of  $s_n$ , disentangled from  $\varphi_n$ , is not possible. Second, since  $\varphi_{bc}$  strongly depends on the specific experimental arrangement, for instance the exact position and orientation of the sample (i.e. the position of scatterers on the sample surface), bad reproducibility of obtained results is expected. Therefore, interferometric detection is preferential (see Section 4.4). In the past, there were several attempts to realize interferometric detection with FELBE. However, this was not successful for technical reasons, mainly due to large intensity noise as compared to table top lasers.

Despite the uncertainties arising from the unknown background phase  $\varphi_{bc}$ , well reproducible results were obtained [18, 19, 37, 38, 110] over many years. Spectral positions of observed resonances, the strength of near-field signals and obtained contrasts are very stable and not sensitive to occasional modifications of the optical setup, which in general can be expected to modify the background light and hence the signal. The origin of this might be the comparatively large focus size of about 100  $\mu\text{m}$  with a rather homogeneous illumination of the area surrounding the tip-sample junction. This gives rise to interference with light originating from a large number of scattering centers on the sample surface, all providing different  $\varphi_{bc}$ , where an average impact on the signal seems to be stable. In addition to this, FELBE is a pulsed infrared source with a pulse length of few ps. Hence, for path-length differences in the mm-regime, no interferences are observed. Note that



with a table top cw CO<sub>2</sub> laser, providing a much longer coherence length, we observe significantly stronger modulations when measuring non-interferometrically (see Figure 7.4.1). Here, interference stripes arise due to a relative displacement of AFM tip and sample when scanning the latter, thereby changing  $\varphi_{bc}$ .

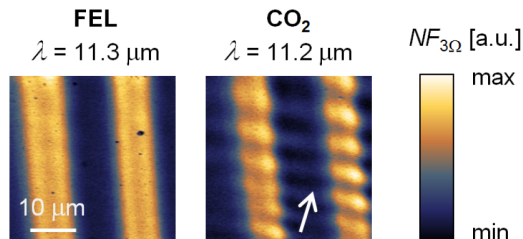


**Figure 7.4.1:** Near-field images of gold-strips (width 10  $\mu\text{m}$ ) obtained with the FEL (left) and a CO<sub>2</sub> laser (right) at a radiation wavelength of  $\lambda = 11.3 \mu\text{m}$  and 11.2  $\mu\text{m}$ , respectively. The white arrow indicates the direction of the incoming laser beam for both cases.

If the signal is not influenced by a change of  $\varphi_{bc}$ , as it seems to be the case for the measurements with the FEL, then this also applies to  $\varphi_n$ . Hence, we can assume for our specific setup in combination with FELBE as a radiation source that

$$NF_{n\Omega} \propto s_n, \quad (7.4.2)$$

where a signal change related to the optical properties of a sample solely arises due to a change of the scattering amplitude  $s_n$ . Please note that this section only discusses the interference of the scattered near-field with *background radiation*. In general, this excludes phase effects, however if the SNOM tip couples to various objects with different permittivities at the same time, which is not considered here, the phase can become relevant. Such an effect was also observed in this work and will be discussed in Section 8.3.3.

## 8 Results of near-field investigation

*In this chapter, SNOM images of gold patterns obtained via various superlens structures are presented, where superlensing is induced by the plasmonic response of a doped GaAs layer. Measurements are shown in a wide mid-infrared spectral range, utilizing a FEL as a radiation source. In order to relate the results to theory, we calculate the permittivity of each superlens, based on the electronic properties obtained by FTIR measurements. The comparison of the doped superlens to an intrinsic GaAs reference sample at the expected superlensing wavelength confirms that enhancement of evanescent waves is indeed induced by the presence of free electrons. A detailed wavelength dependence of both the strength of the transmitted near-field through the superlens and the respective resolution of the imaged gold pattern provides excellent agreement to the resonant behavior of the calculated transfer function. As a secondary effect, the image contrast reverses at a wavelength well separated from the superlensing condition, which can be attributed to a resonant coupling between SNOM probe and doped layer. When comparing different samples in spectral proximity to the superlensing wavelength, we find that the obtained resolution decreases with increasing layer thickness, however, the resonant nature of the effect gets subtle for too thin samples. Even though the various superlenses do not exhibit large differences in terms of electron density, our results provide indications for a corresponding spectral shift of the resonance, demonstrating that the superlensing wavelength can be controlled by changing the doping level. For all investigations the near-field signal nonlinearly decays to zero when increasing the distance between probe and superlens surface. This is evidence that the measurements are free of far-field background. Finally, we qualitatively discuss the origin of the comparably large working bandwidth of the plasmonic GaAs superlenses.*

### 8.1 Sample overview and expectations

The superlens structures to be investigated consist of an n-doped GaAs layer (thickness  $d$ ) sandwiched between two intrinsic layers (thickness  $d/2$ ). For the SNOM measurements, the superlenses were placed onto gold patterns to be imaged. As described in Section 5.4, doping offers the potential to control the superlensing wavelength  $\lambda_{SL}$ , which is determined

by the electron density  $n$  and the electronic damping  $\gamma_{\text{el}}(n)$  of the conductive GaAs layer. Values of  $n$  and  $\gamma_{\text{el}}$ , obtained by FTIR reflectivity measurements (see Section 6.3.1), are inserted to calculate the dielectric function  $\varepsilon$ . In Figure 8.1.1, all investigated samples are depicted schematically, varying in  $n$ ,  $\gamma_{\text{el}}$ , total thickness  $2d$  and object to be imaged. Here, the numbering of the samples is the same as in Table 6.3.1, where the results of

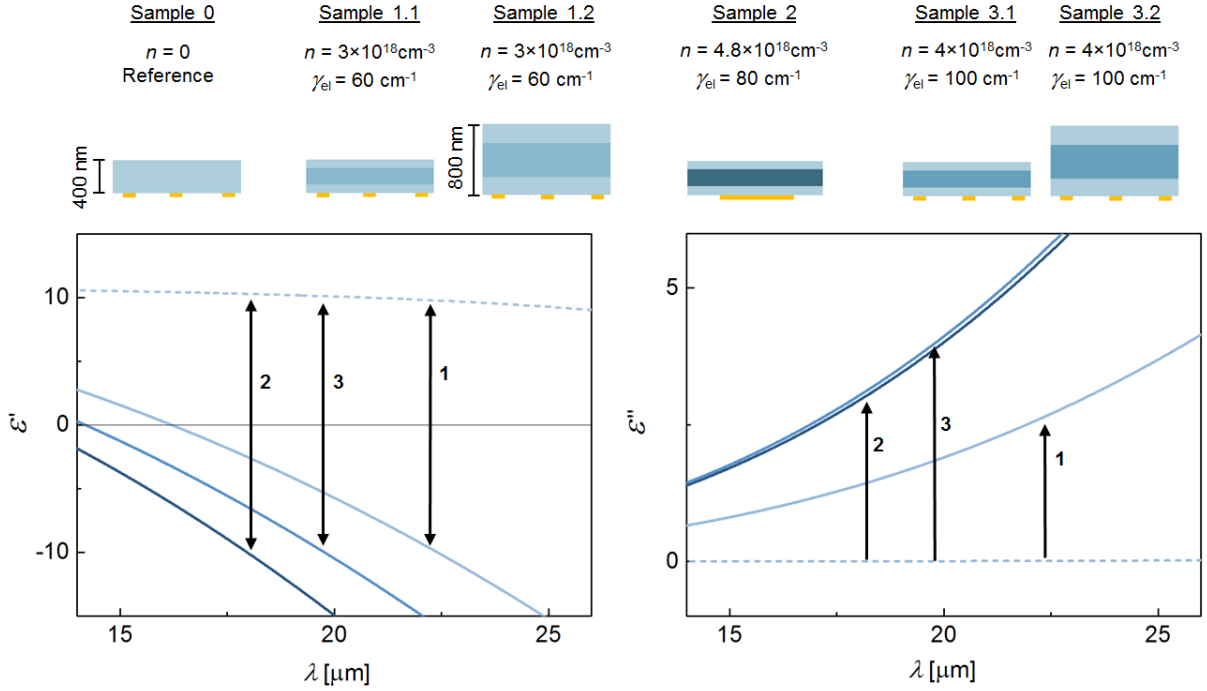


**Figure 8.1.1:** Overview of all investigated superlenses. For each sample,  $\varepsilon'$  and  $\varepsilon''$  of the doped middle layer were calculated based on the respective values of  $n$  and  $\gamma_{\text{el}}$ . Arrows indicate the expected resonance wavelengths, pointing to the  $\varepsilon$  of the respective numbered sample. The dashed line corresponds to intrinsic GaAs.

the electronic pre-characterization were summarized. For the doped layer in the middle, different nuances of blue correspond to different  $n$ , dark blue indicating a high value of  $n$ . The same color code is applied to depict for each case the real and imaginary part of the permittivity,  $\varepsilon'$  and  $\varepsilon''$ , respectively. Black arrows, numbered according to the associated superlenses, indicate the expected superlensing wavelengths, following the condition  $\varepsilon'_{\text{n-GaAs}} = -\varepsilon'_{\text{GaAs}}$  (see Equation 5.1.1). In the graphs, the dashed line corresponds to  $\varepsilon$  of the outer, intrinsic layers. As one can see, superlensing can be expected within the wavelength range  $\lambda = 17 \dots 23 \mu\text{m}$  in all cases, the resonances being separated from each other

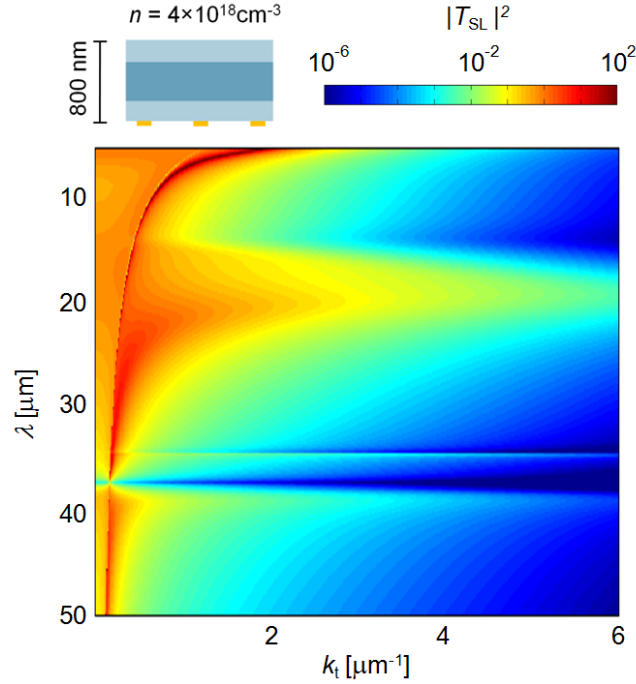


**Figure 8.1.2:** Calculated transfer function  $|T_{\text{SL}}|^2$  of Sample 3.2, plotted in logarithmic scale for good visibility [26].

by  $\approx 2 \mu\text{m}$ . Since for all samples  $\varepsilon''(\lambda_{\text{SL}})$  is quite similar<sup>1</sup>, image qualities are expected not to differ a lot from each other (for a given  $d$ ). When presenting the experimental results in the following sections, sample numbers according to Figure 8.1.1 are indicated in the figure captions.

For the superlens which was investigated in most detail (Sample 3.2), the transfer function  $|T_{\text{SL}}|^2$  (see Section 3.2.3) was calculated<sup>2</sup> and is shown in Figure 8.1.2. Here,  $|T_{\text{SL}}|^2$  is the transmittance through the three-layered structure, which is considered to be adjacent to air on both sides for the calculation, providing the intrinsic properties of the superlens. The transmittance of large tangential wavenumbers  $k_t$  is resonantly enhanced at a radiation wavelength  $\lambda \approx 20 \mu\text{m}$ , where an increase of spatial resolution and of near-field signal is expected. Here, the resonance wavelength is consistent with the condition in terms of  $\varepsilon'$ , which is visualized in Figure 8.1.1. Note that the prominent red line in the color scaled plot of the transfer function corresponds to the light line, i.e.  $k_t = k = \omega/c$ , separating propagating waves on its left hand side and evanescent waves on the right hand side.

<sup>1</sup>Since both increasing  $\gamma_{\text{el}}$  and increasing  $n$  leads to an increase of  $\varepsilon''$ , it happens that  $\varepsilon''(\lambda)$  is almost identical for Sample 2 and Sample 3 in the displayed wavelength range.

<sup>2</sup>The transfer functions presented in this thesis were calculated by cooperation partners (PhD student Kan Yao under supervision of Prof. Yongmin Liu) at the Department of Electrical and Computer Engineering, Northeastern University, Boston, Massachusetts 02115, United States.

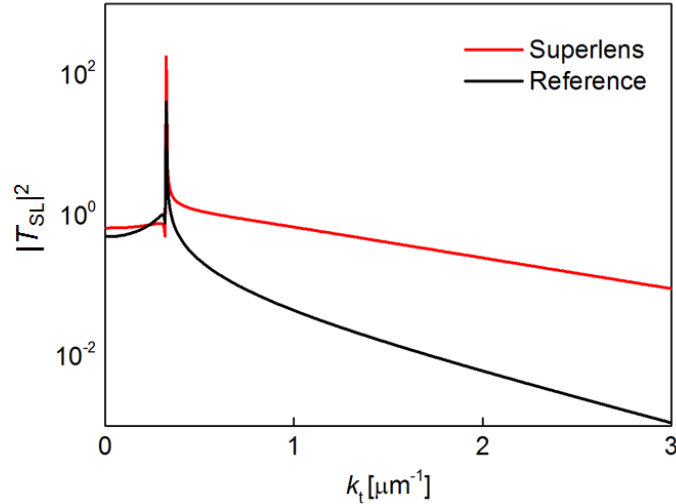


**Figure 8.1.3:** Transfer function  $|T_{\text{SL}}|^2$  at the expected resonance wavelength  $\lambda = 19.8 \mu\text{m}$ , depicted both for Sample 3.2 and an undoped reference structure of equal thickness.

The decreased transmission around  $\lambda \approx 37 \mu\text{m}$  is attributed to the Reststrahlen band of GaAs. Figure 8.1.3 depicts the transfer functions of Sample 3.2 and of a corresponding undoped reference structure of the same total thickness at fixed  $\lambda = 19.8 \mu\text{m}$ , which is the wavelength where superlensing is expected. As can be seen, the transmittance of large tangential wavenumbers is significantly enhanced by the presence of the doping layer in the superlens structure.

## 8.2 Data acquisition and evaluation

Near-field images of the gold objects via the GaAs superlenses are obtained by a scattering-type scanning near-field optical microscope (s-SNOM) in combination with a free-electron laser (FEL), which is frequency tunable over a large infrared spectral range (for experimental details and theory see Chapters 7 and 4, respectively). This is depicted schematically in Figure 8.2.1. The s-SNOM probe, a metallized atomic force microscope (AFM) tip, is illuminated at an angle of  $65^\circ$  with respect to the surface normal, with the light scattered at the probe-sample junction (near-field (NF) signal) being detected in backward direction. Here, the laser beam is p-polarized, with the electric field vector  $\mathbf{E}$  oriented parallel to the plane of incidence. The AFM is operated in tapping mode and near-field signals are obtained by demodulating the scattered light at the second and third harmonic of the cantilever oscillation frequency  $\Omega$ , denoted as  $NF_{2\Omega}$  and  $NF_{3\Omega}$ , respectively. While  $NF_{2\Omega}$  provides a larger signal strength and therefore a better signal-to-noise ratio,  $NF_{3\Omega}$

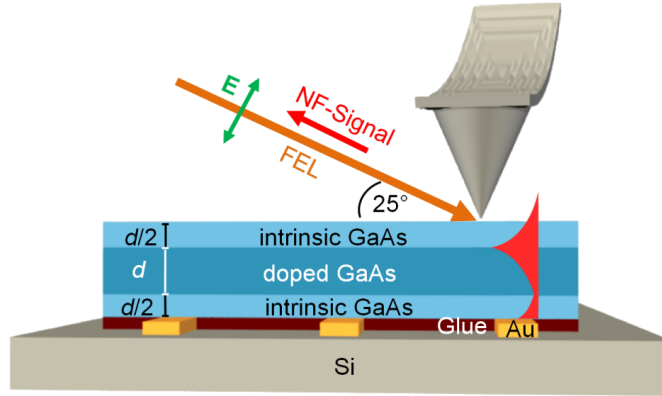


**Figure 8.2.1:** Schematic illustration of the experiment [26]. At the resonance wavelength  $\lambda_{SL}$ , the GaAs superlens structure is expected to provide a non-diffraction-limited image of the buried gold-patterns, caused by an enhanced transfer of evanescent waves (red feature in the sample) through the multilayer slab.

can be expected to be less disturbed by far-field background radiation (see Section 4.4). A two-dimensional image arises by scanning the probe across the superlens surface and recording both  $NF_{2\Omega}$  and  $NF_{3\Omega}$  simultaneously at each position. In this section, most of the SNOM images are depicted by applying a full-range color scale, which is convenient for a comparison of the spatial resolution. For an evaluation of the transmitted near-field strength, however, images of a series of measurements are all plotted in the same color scale. To this end, signals are normalized to detector response, lock-in sensitivity and laser power, where the latter is recorded during the measurement with the help of a beam splitter and a powermeter (see Section 7.3).

## 8.3 Imaging a periodic stripe-pattern

In this section, near-field images of a periodic pattern of gold stripes (width  $2 \mu\text{m}$ , distance  $10 \mu\text{m}$ ), obtained via a number of superlens structures, are presented. The imaging is performed in the wavelength range from  $\lambda = 12 \mu\text{m}$  to  $26 \mu\text{m}$ .

### 8.3.1 Doping induced near-field enhancement

In order to prove the enhancement of evanescent waves induced by the superlensing effect, the near-field of the gold-stripe pattern underneath a  $400 \text{ nm}$  thick superlens (doped layer:  $d = 200 \text{ nm}$ ;  $n = 4 \times 10^{18} \text{ cm}^{-3}$ ) was compared to the case of an equally thick intrinsic reference structure [26]. The measurement was performed at a radiation wavelength of

$\lambda = 20.4 \mu\text{m}$ , which is close to the wavelength where superlensing is expected. The result is shown in Figure 8.3.1. Additionally, an optical micrograph of the stripes is shown for comparison, which was obtained before the pattern was covered by the superlens.

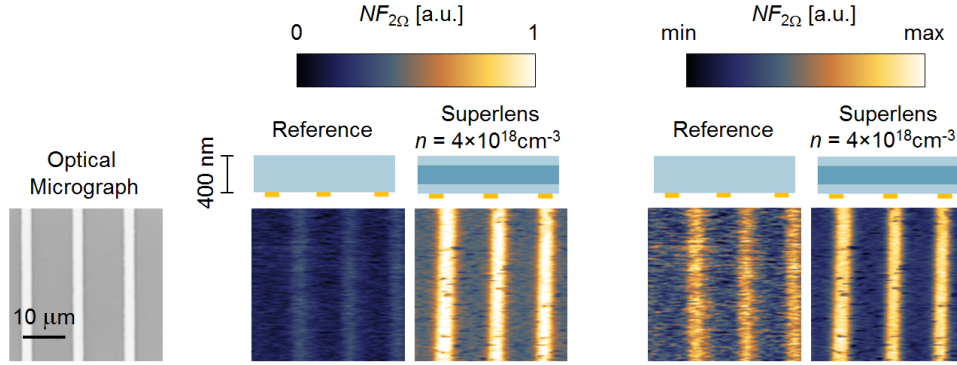


**Figure 8.3.1:** Near-field images ( $NF_{2\Omega}$ ) of gold stripes, obtained via a superlens and via an intrinsic GaAs layer for reference (Sample 3.1 and Sample 0, respectively; see Section 8.1), recorded at expected resonance conditions ( $\lambda = 20.4 \mu\text{m}$ ). Left: Same color scale applied to each image. Right: Full-range color scale applied to each image. For comparison, an optical micrograph is also shown.

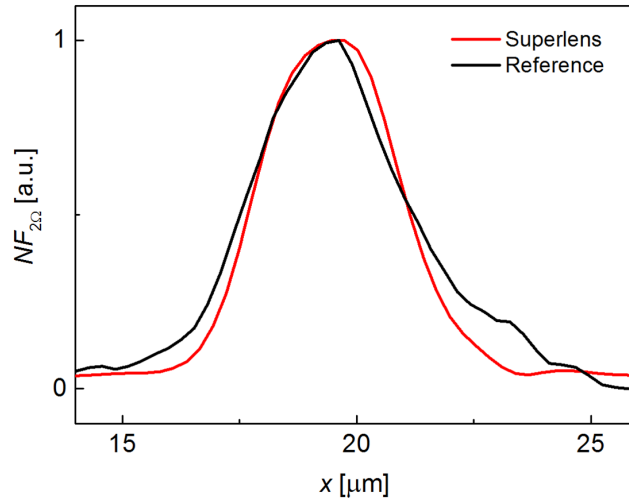


**Figure 8.3.2:** Line profiles across a gold-stripe's image at  $\lambda = 20.4 \mu\text{m}$ . For both curves, the signal between the stripes was subtracted and the maximum value was normalized to one.

Comparing the strength of the near-field signal provides clear evidence for superlensing. Applying the same color scale to each image (obtained at equal experimental conditions) illustrates that the doped layer significantly enhances the transmittance of the gold stripes' near-field. If there were no superlensing effect, one would expect even weaker signals in

case of the superlens sample, since doping results in free-carrier absorption that attenuates the near-field of the object.

The analysis of the spatial resolution, on the other hand, yields rather subtle differences, which is seen by applying a full-range color scale to each image. Despite the different signal strengths, the resolution appears to be very similar. In both cases, the  $2\ \mu\text{m}$  stripes are imaged with an apparent width of about  $3\ \mu\text{m}$ . At this point it is important to mention that burying structures to be imaged by SNOM *always* results in a decreased resolution as compared to imaging the surface directly. In case of an intrinsic GaAs layer (reference sample), the reason for this is the increased distance between the SNOM tip and the structure [20], whereas in case of the superlens, losses (i.e.  $\varepsilon''$ ) within the doped layer reduce the imaging quality (see Equation 3.2.9). For the layer thickness chosen here, this happens to provide the same apparent width of a gold stripe in both cases. However, even though there are no large differences at first view concerning this aspect, a line profile across one stripe (see Figure 8.3.2) reveals that the lateral distribution of the near-field differs. To be more precise, the rise of the signal is considerably steeper in case of the superlens, pointing to a transfer of larger tangential wavenumbers of the stripe's emitted field as compared to the reference sample. This is exactly what is shown in Figure 8.1.3, where the calculated transfer function for the two cases is depicted (with the only difference of doubled layer thickness and slightly reduced  $\lambda$  in case of the calculation).

The conclusion of the observations presented in this section is that the introduction of a doped layer, converting the intrinsic GaAs layer into a superlens, enables imaging of buried structures with drastically increased signal while maintaining subwavelength resolution.

### 8.3.2 Spectral dependence of the superlensing effect

Having proven the enhancement of evanescent waves by the GaAs superlens, the spectral dependence of the effect was investigated [26]. As it was shown in the previous section, the pattern to be imaged did not vanish completely in case of the reference sample. Thus, one can assume that the near-field transmitted through the doped structure is not purely induced by the superlensing effect, but provides an offset which is independent of it. In order to suppress this background, the superlens thickness was doubled to  $800\ \text{nm}$  for further investigations. Images were obtained in a wavelength range between  $\lambda = 16.7\ \mu\text{m}$  and  $\lambda = 25.8\ \mu\text{m}$ .

In Figure 8.3.3, both  $NF_{2\Omega}$  and  $NF_{3\Omega}$  images are shown, applying full-range color scale to each measurement. This depiction is convenient to recognize differences in terms of resolution. Obviously, in the  $NF_{2\Omega}$  images, the stripes get blurred to both sides of the



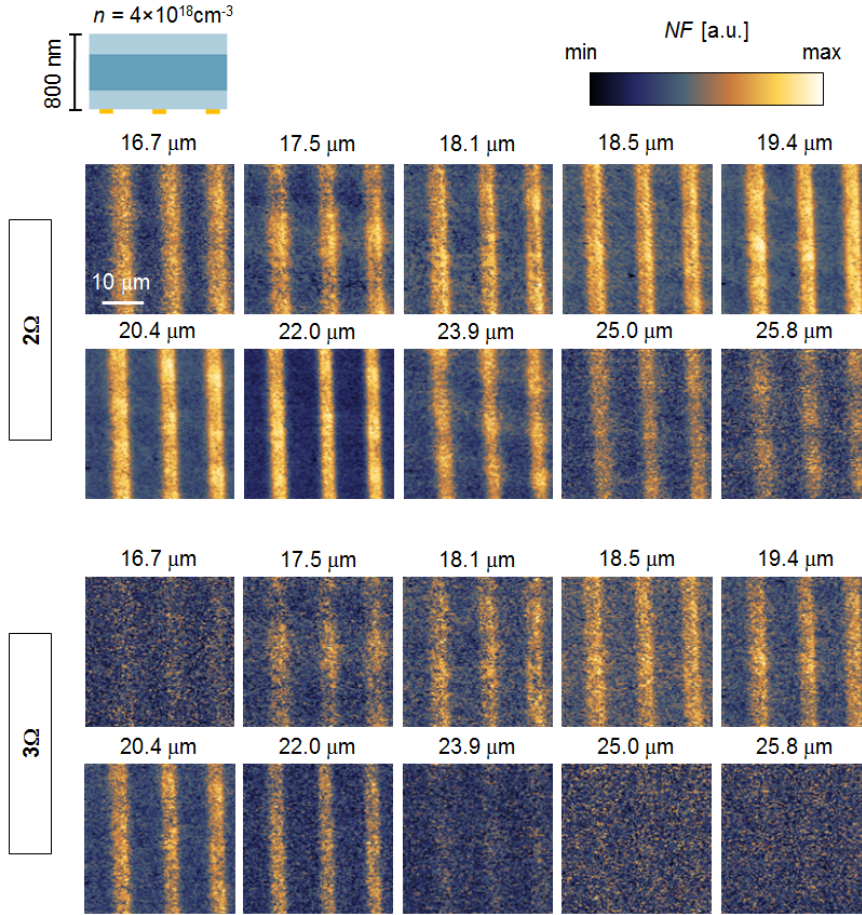


**Figure 8.3.3:** Wavelength dependence with full-range color scale applied to all images. Top:  $NF_{2\Omega}$  signals. Bottom:  $NF_{3\Omega}$  signals (Sample 3.2; see Section 8.1).

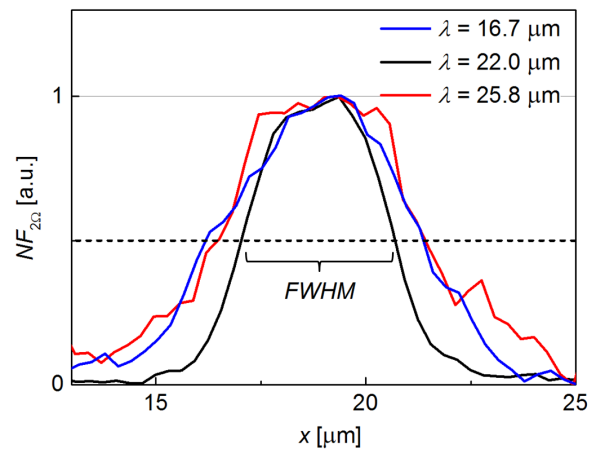


**Figure 8.3.4:** Offset subtracted and normalized profiles of a gold-stripe's image for selected radiation wavelengths. For  $\lambda = 22.0 \mu\text{m}$ , the full width at half maximum ( $FWHM$ ) is indicated.

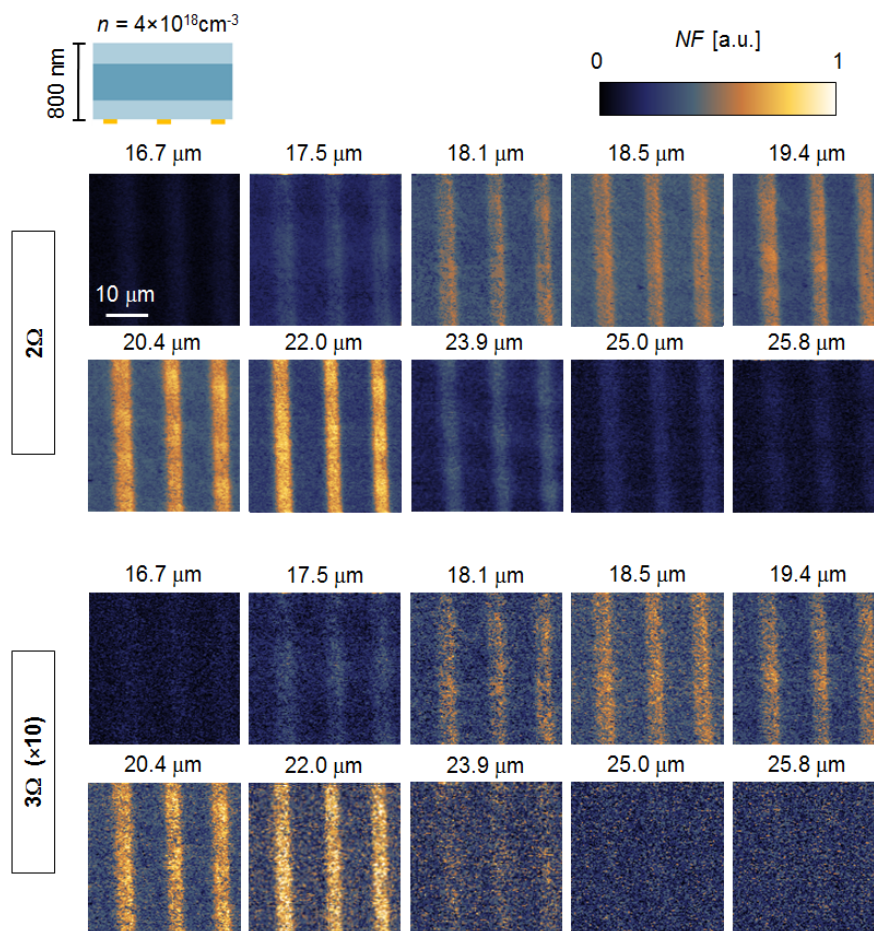


**Figure 8.3.5:** Wavelength dependence with same color scale applied to all images. Signals are normalized to laser power, detector response and lock-in sensitivity (Sample 3.2; see Section 8.1).

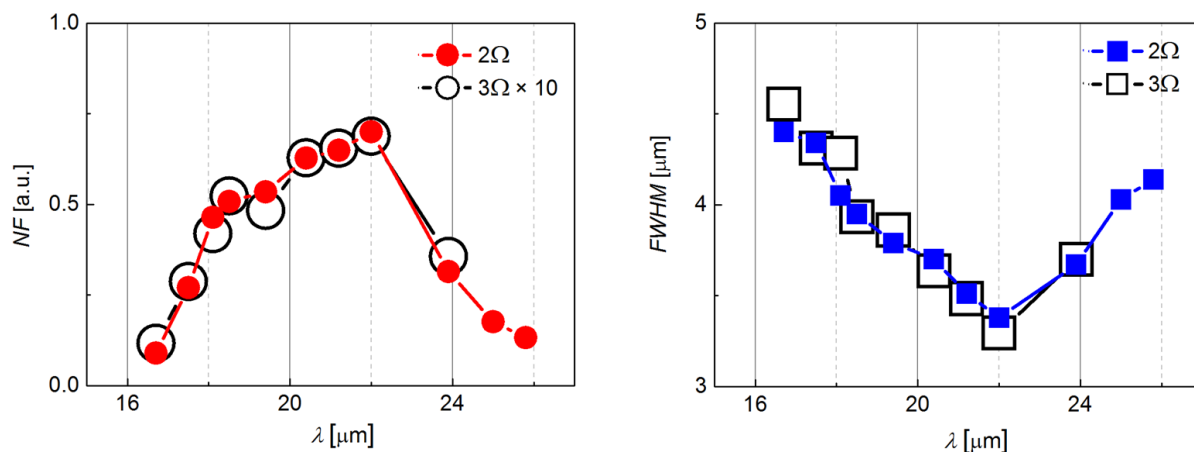


**Figure 8.3.6:** Near-field signal  $NF$  at the position of gold and  $FWHM$  of a stripe's image as a function of  $\lambda$ .

investigated spectral range. This also holds for  $NF_{3\Omega}$ , however here the stripes vanish completely<sup>3</sup> if  $\lambda > 24 \mu\text{m}$ . The best resolution corresponding to the smallest apparent width of a stripe is observed at  $\lambda = 22.0 \mu\text{m}$ . This is in very good agreement to calculations (see Figure 8.1.1), whereupon superlensing is expected<sup>4</sup> at  $\lambda \approx 20 \mu\text{m}$ . For a quantitative evaluation, the full width at half maximum ( $FWHM$ ) of a stripe's image was determined at each wavelength. In Figure 8.3.4, this is shown exemplary for the  $NF_{2\Omega}$  images obtained at  $\lambda = 16.7, 22.0$  and  $25.8 \mu\text{m}$ . The complete  $\lambda$ -dependence is depicted in Figure 8.3.6, demonstrating the resonant character of resolution improvement. Here, very similar values were extracted for both  $NF_{2\Omega}$  and  $NF_{3\Omega}$ . At resonance, we obtain  $FWHM \approx 3.4 \mu\text{m}$ , corresponding to a subwavelength resolution of  $\lambda/6$ . Note that the width of the stripe itself ( $2 \mu\text{m}$ ) considerably contributes to the  $FWHM$ , so it can be expected that the actual obtainable resolution is even better.

Figure 8.3.5 depicts the same measurements as Figure 8.3.3, however this time all signals are plotted applying the same color scale. This allows one to quantitatively compare the strength of the evanescent field which is transmitted through the superlens. Just like the obtained resolution, the signal resonantly peaks at  $\lambda = 22.0 \mu\text{m}$ , significantly decreasing to both sides of the spectrum. The near-field signal at the position of the gold-stripes as function of the applied wavelength is shown in Figure 8.3.6. Again,  $NF_{2\Omega}$  and  $NF_{3\Omega}$  exhibit the same spectral dependence (apart from a factor of 10). Note in particular that this indicates the high quality of the  $NF_{2\Omega}$  signal in these measurements, which is usually more impacted by unwanted far-field background radiation compared to  $NF_{3\Omega}$  (see Section 4.4).

Both the improvement of resolution and the near-field enhancement resonantly appear with a relative spectral width  $\Delta\lambda/\lambda_{\text{SL}}$  of about 25%. This is significantly larger than for other infrared superlenses investigated in the past, where  $\Delta\lambda/\lambda_{\text{SL}} \approx 10\%$  was observed. This will be discussed later in Section 8.6.

### 8.3.3 Near-field resonance of the doped layer

In Section 8.3.2 superlensing was demonstrated at  $\lambda = 22 \mu\text{m}$  (superlens Sample 3.2), where the near-field signal of the gold objects resonantly increases. The signal strength of the superlensed image gets weaker when going either to longer or to shorter  $\lambda$ , as demonstrated by recording near-field images in a range from  $\lambda = 16.7 \mu\text{m}$  to  $25.8 \mu\text{m}$  (see Figure 8.3.5). At even shorter  $\lambda$ , the signal remains comparably weak, however an

<sup>3</sup>Typically,  $NF_{2\Omega}$  is significantly larger than  $NF_{3\Omega}$ .

<sup>4</sup>The reason for the small discrepancy between experiment and theory might be that the Lorentz-Drude model (see Section 5.2), which is applied for simulations, simplifies the actual system.

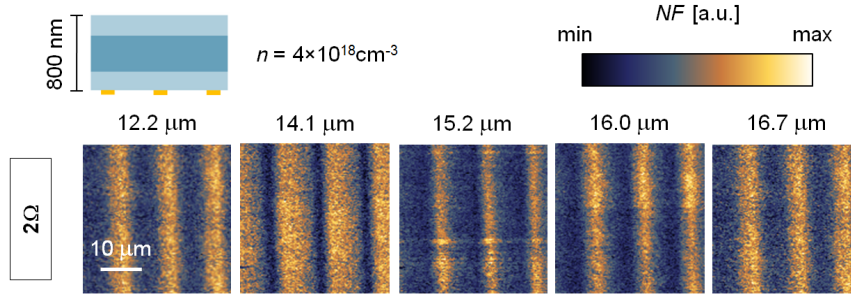


**Figure 8.3.7:** Spectral dependence of  $NF_{2\Omega}$  images at wavelengths well separated from the superlensing condition (Sample 3.2; see Section 8.1)

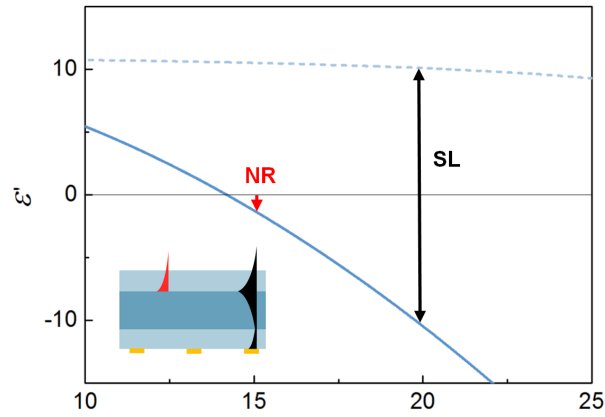


**Figure 8.3.8:** Real permittivities  $\epsilon'_{n-\text{GaAs}}$  (solid) and  $\epsilon'_{\text{GaAs}}$  (dashed) of the middle doped layer and the outer intrinsic layers, respectively. The condition for superlensing (SL) is  $\epsilon'_{n-\text{GaAs}} = -\epsilon'_{\text{GaAs}}$ , whereas the near-field resonance (NR) of the doped layer occurs if  $\epsilon'_{n-\text{GaAs}} \approx -1$ . The inset schematically illustrates the corresponding fields in respective colors.

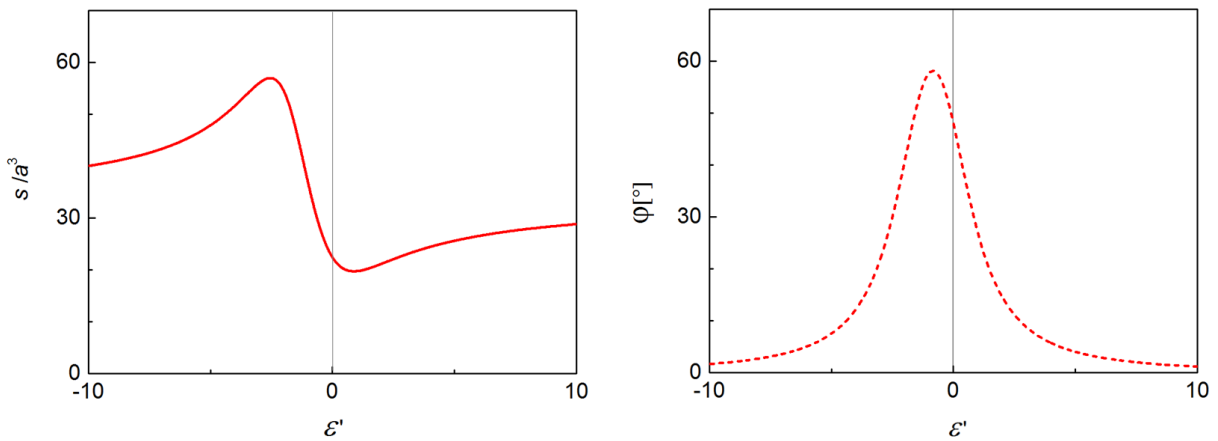


**Figure 8.3.9:** Scattering amplitude  $s$  and scattering phase  $\varphi$  of the SNOM probe (curvature radius  $a$ ) in contact with a sample of permittivity  $\epsilon = \epsilon' + i\epsilon''$  with  $\epsilon'' = 2 = \text{const.}$

interesting effect occurs: At  $\lambda = 14.1 \mu\text{m}$  the image contrast is reversed, the gold-stripes appearing darker than the surroundings (see Figure 8.3.7)<sup>5</sup>. This can be attributed to resonant near-field coupling between the doped GaAs layer and the SNOM probe (near-field resonance), which occurs if the real permittivity  $\varepsilon'$  exhibits small negative values close to  $-1$  (see Figure 8.3.8). According to the calculations,  $\varepsilon'_{\text{n-GaAs}}$  of this conductive layer becomes negative at  $\lambda \approx 14 \mu\text{m}$ , giving rise to strong changes of the related scattering phase  $\varphi$  and an increase of the scattering amplitude  $s$  (see Figure 4.2.2 in Section 4.2.3), which are directly connected to the near-field signal  $NF_{n\Omega}$  (see Section 4.4). In Figure 8.3.9  $s$  and  $\varphi$  are shown as a function of  $\varepsilon'_{\text{n-GaAs}}$  with  $\varepsilon''_{\text{n-GaAs}}$  (imaginary part) approximated by a constant value of 2, which is the calculated value for  $\lambda \approx 14 \mu\text{m}$  (see Figure 8.1.1, Sample 3.2). Note that for the calculation of  $s(\varepsilon'_{\text{n-GaAs}})$  and  $\varphi(\varepsilon'_{\text{n-GaAs}})$  we do not consider that the doped layer is buried underneath 200 nm of intrinsic GaAs. Hence we cannot rely on absolute values, nevertheless it allows the following qualitative discussion. Let us consider the signal to be a superposition of two effects, one originating from the coupling between probe and gold-object through the superlens structure,  $NF_{\text{Au}}$ , and one resulting from the interaction between probe and doped layer<sup>6</sup>,  $NF_{\text{n-GaAs}}$ . At the superlensing condition, i.e. at  $\lambda = 20 \mu\text{m}$  (calculated value), we can expect that  $NF_{\text{Au}}$  dominates the signal due to the resonant enhancement of the gold-stripe's evanescent waves through the superlens. Away from the resonance, we may assume that  $NF_{\text{Au}}$  and  $NF_{\text{n-GaAs}}$  are of comparable amplitude. For off-resonant excitation (i.e. no superlensing effect and no near-field resonance), phase effects are negligible and the two contributions can be expected to be in phase, taking into account that the distance of 600 nm between the upper surface of the n-GaAs layer and the gold objects is much smaller than the radiation wavelength  $\lambda > 10 \mu\text{m}$ . Hence, the stripes appear brighter since the signals add up constructively. However, if  $NF_{\text{n-GaAs}}$  exhibits strong phase changes, which seems to be the case at  $\lambda \approx 15 \mu\text{m}$  where  $\varepsilon'_{\text{n-GaAs}} = -1$ , they can interfere destructively at the position of the stripes, letting them appear dark compared to areas where solely  $NF_{\text{n-GaAs}}$  is measured.

Note that the results presented here not only reveal an interesting secondary effect, they also confirm the accuracy of the calculated permittivity of the superlens layers, obtained by pre-characterization (see Section 6.3), which is the basis for interpreting the superlensing effect.

<sup>5</sup>Note that only  $NF_{2\Omega}$  is depicted in this case, since the signal is too weak to provide contrast for  $NF_{3\Omega}$ .

<sup>6</sup>Note that, in addition, there is a third contribution due to the coupling between tip and upper intrinsic layer,  $NF_{\text{GaAs}}$ . However, since  $\varepsilon_{\text{GaAs}} \approx 10$  for all SNOM investigations presented in this work (no near-field resonance), this contribution can be regarded as a constant offset accompanying all our measurements, which does not impact any statements made.

### 8.3.4 Comparison of various superlens structures - indication of spectral tuning

In this section, images obtained via various superlenses are compared in a spectral range between  $\lambda = 17.5 \mu\text{m}$  and  $24.8 \mu\text{m}$ . In contrast to the previous sections, all of them are presented in full-range color scale only, not providing absolute values of the near-field signal<sup>7</sup>.  $NF_{2\Omega}$  and  $NF_{3\Omega}$  signals are shown in Figure 8.3.10 and in Figure 8.3.11,

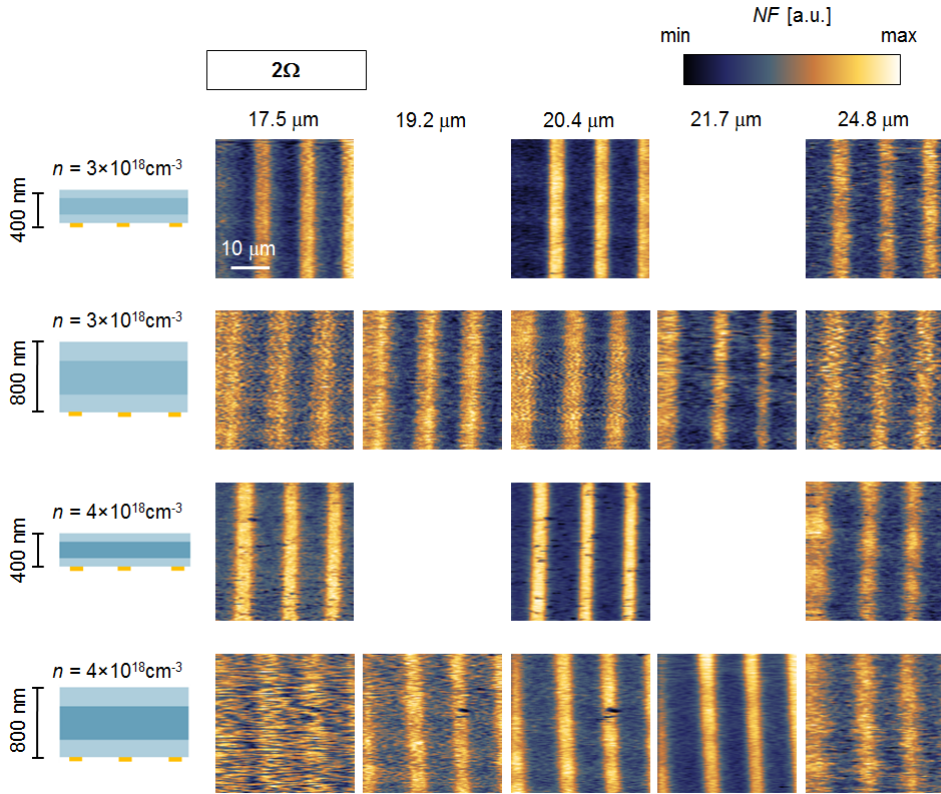


**Figure 8.3.10:** Spectral dependence of  $NF_{2\Omega}$  images obtained via superlenses of various thicknesses  $2d$  and electron densities  $n$  (Samples 1.1, 1.2, 3.1 and 3.2 from top to bottom; see Section 8.1).

respectively. The superlenses differ in thickness  $2d$  (400 and 800 nm;  $d$  is the thickness of the doped layer) and electron concentration  $n$  ( $3 \times 10^{18}$  and  $4 \times 10^{18} \text{ cm}^{-3}$ ). For the sample providing higher  $n$ , the superlensing wavelength  $\lambda_{\text{SL}}$  was demonstrated to be

<sup>7</sup>All of the measurements presented in this section were performed in the frame of one single beamtime period at the free-electron laser FELBE. Due to a lack of time, all samples had to be investigated consecutively at each wavelength  $\lambda$ , necessitating a frequent exchange in the setup. In order to reasonably evaluate the spectral dependence of the near-field signal's absolute value, however, all data should be obtained with exclusively varying  $\lambda$ .

about<sup>8</sup>  $22 \mu\text{m}$  in the previous section. According to the calculations (see Figure 8.1.1),  $\lambda_{\text{SL}}$  is expected to shift to longer wavelengths in case of the superlens with lower  $n$  by about  $\Delta\lambda = 2.5 \mu\text{m}$ . There is no reason to assume that  $\lambda_{\text{SL}}$  changes when changing the thickness of the superlens.

As a first observation, all samples provide images with resonantly increasing sharpness of the gold stripes, indicating the superlensing effect to occur within the investigated wavelength range in every case. For the thick superlenses, it turns out that the effect is

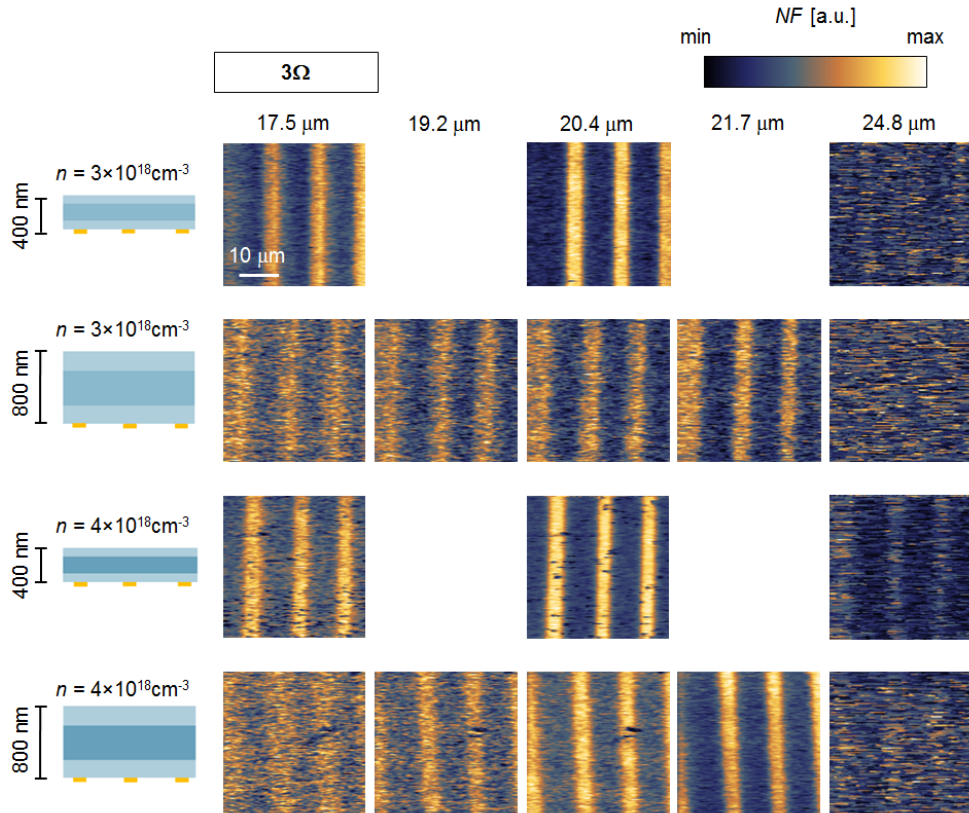


**Figure 8.3.11:** Spectral dependence of  $NF_{3\Omega}$  images obtained via superlenses of various thicknesses  $2d$  and electron densities  $n$  (Samples 1.1, 1.2, 3.1 and 3.2 from top to bottom; see Section 8.1).

much more pronounced than for the thin ones. This can be understood by considering the limit  $d \rightarrow 0$ , where the image converges to the case of imaging the gold pattern directly at its surface with a wavelength independent near-field signal (in the mid-infrared spectral range, the permittivity of gold is almost constant) and spatial resolution. Increasing  $d$  to infinity of course results in zero near-field transmission, so there must be an optimum

<sup>8</sup>An exact determination would require smaller  $\lambda$ -intervals in the measurements, which was not possible due to limitations concerning the FELBE operation.

thickness for the investigation of the superlensing effect. Here,  $2d = 800$  nm seems to be a better choice than  $2d = 400$  nm. This is in agreement with the observation that a non vanishing signal is obtained via the 400 nm reference structure, suggesting that the resonant behavior observed with the 400 nm thick superlens is accompanied by a non-resonant offset (see Section 8.3.1). Nevertheless, the thin samples yield better images than the thick ones for a given  $\lambda$ , since there is less dissipation. Note that this difference is most significant at  $\lambda = 17.5 \mu\text{m}$ , which is farthest from the expected resonances for all samples.

While the thin superlenses with different  $n$  do not yield results that differ significantly, this does not apply for the thick samples. Here, the spectral dependencies are clearly different. Not considering the superlensing effect, stronger near-field signals of the gold stripes are expected to be obtained in case of less charge carriers, since there is less Drude absorption which attenuates the evanescent waves. Indeed this was observed at  $\lambda = 17.5 \mu\text{m}$ , where the stripes appear clearer when utilizing the superlens sample providing lower free electron concentration. As shown in Section 8.3.2,  $17.5 \mu\text{m}$  is just at the short wavelength edge of the observed superlensing effect for the higher doped sample (see Figure 8.3.6), and therefore is expected to be even more off-resonant for the superlens providing lower  $n$  (i.e. longer  $\lambda_{\text{SL}}$ ). Thus, this result at off-resonance is in agreement with expectations. Increasing  $\lambda$  to  $19.2 \mu\text{m}$  reverses the relation between the two samples. Now, higher  $n$  provides clearer images. For both samples the resolution gets better until  $\lambda = 21.7 \mu\text{m}$ , however the improvement is much clearer in case of high  $n$  (especially for the  $NF_{3\Omega}$  images), where  $\lambda_{\text{SL}}$  was already determined to be around  $22 \mu\text{m}$ . This is in agreement with the expectation that  $\lambda_{\text{SL}}$  for the lower doped superlens is shifted to longer wavelengths. As already mentioned (see Footnote 7 in this section), a sophisticated evaluation of absolute values of the near-field signal, as it was done in Section 8.3.2, was not possible in this case. In addition, the data presented here are too noisy to allow for a proper comparison of the  $FWHM$ . However, even though more measurements have to be performed for a conclusive confirmation, these results indicate superlenses with different resonance wavelengths due to different electron densities<sup>9</sup>.

## 8.4 Imaging a non-periodic object

As presented in the previous sections, a periodic pattern of gold stripes was imaged to evidence the superlensing effect. In order to rule out that this periodicity gives rise to resonant phenomena, which misleadingly could be interpreted as superlensing, near-field images of a gold disc with radially oriented stripes (non-periodic) were obtained in a

<sup>9</sup>Unfortunately, there was not enough beamtime at FELBE for a more accurate investigation.



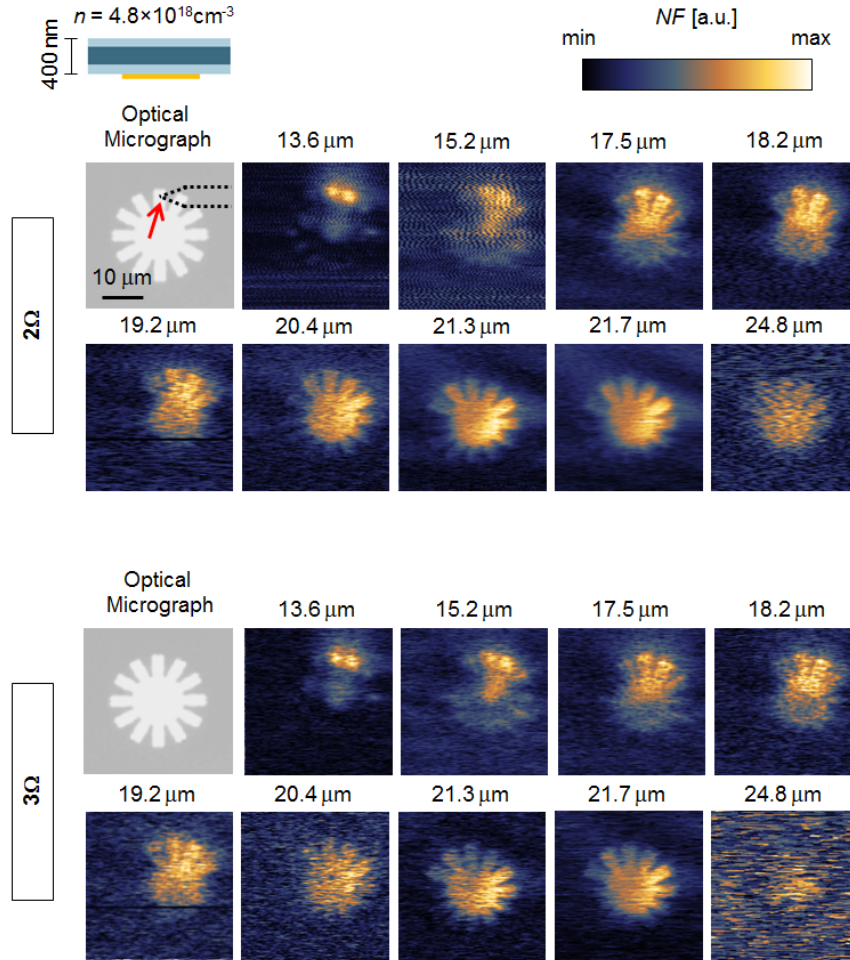


**Figure 8.4.1:** Superlens mediated near-field images of a flower-like pattern obtained at various radiation wavelengths (Sample 2; see Section 8.1). The direction of the p-polarized laser (FEL) beam is given by the red arrow in the optical micrograph on the top left (taken before the object was buried below the superlens), where the black dotted line indicates the orientation of the cantilever during a measurement. Note that in reality the cantilever is larger than depicted.

complementary study. Here, the thickness of the superlens is  $2d = 400$  nm and the measured electron-concentration is  $n = 4.8 \times 10^{18} \text{ cm}^{-3}$ . For the same reason as in Section 8.3.4, all images are presented in full-range color scale only.

The measurements depicted in Figure 8.4.1 demonstrate that, like for the periodic pattern, the disc is imaged with subwavelength resolution in a spectrally resonant fashion. As can be seen,  $\lambda = 21.3 \mu\text{m}$  yields the best result, which is slightly shorter than  $\lambda_{\text{SL}}$  obtained with other investigated superlenses. This is in agreement with expectations, since we deal here with the sample providing the highest value of  $n$ .

At  $\lambda = 13.6 \mu\text{m}$  the image almost vanishes completely, because there is no superlensing. However, large local field enhancement is observed at two stripes of the object which are oriented along the direction of the incoming laser beam (red arrow in the optical micrograph shown in Figure 8.4.1). Since the radiation is p-polarized, this also corresponds to the orientation of the in-plane component of the electric field  $\mathbf{E}$ . This points to an antenna-like optical response of the pattern, which for an elongated structure like the stripes occurs if  $\mathbf{E}$  is parallel to its axis [111]. Being a resonant effect, the resonance wavelength depends on the surrounding medium of the structure and its size and shape. Note that, at one side, the gold-stripes border on intrinsic GaAs, which exhibits a refractive index  $n^* \approx 3.2$  at  $\lambda = 13.6 \mu\text{m}$ , resulting in a wavelength of about  $4 \mu\text{m}$  in GaAs. This is in the order of the length of the stripes. On the other side, they are surrounded by glue of unknown  $n^*$ . Due to this uncertainty and due to the rather complicated shape of the complete object, a further analysis is beyond the scope of this work.

Finally it should be noted that the asymmetry, which is present for all images and most striking at short wavelengths, might be due to shadowing the sample by the structure carrying the SNOM probe, i.e. the tip shaft and the cantilever of the AFM (indicated by the black dotted line in the optical micrograph shown in Figure 8.4.1). When probing at a position corresponding to the lower area of the image, less radiation (indicated by the red arrow in Figure 8.4.1) reaches the pattern as compared to probing at the upper area, since part of the light is reflected by the cantilever. Therefore, the lower part of the object appears significantly darker than the upper part. Such an effect was also observed and discussed in Ref. [37]. Note that only at  $\lambda = 21.3 \mu\text{m} = \lambda_{\text{SL}}$ , details at the lower side of the object can be recognized.

## 8.5 Distance dependence

For all near-field measurements presented in this work, the signal is largest when the SNOM probe is in contact with the superlens surface, decaying to zero within a distance  $h \approx 100 \text{ nm}$ . With this characteristic behavior being always the same, Figure 8.5.1 exemplary depicts  $NF_{2\Omega}(h)$  and  $NF_{3\Omega}(h)$  obtained with superlens Sample 3.2 at the position of a gold-stripe for  $\lambda = 21.7 \mu\text{m}$ . This is very close to the superlensing wavelength, as demonstrated in Section 8.3.2. In contrast to our observation, a closely related superlens study [37] based on perovskites reports on enhanced signal at a certain distance  $h \neq 0$  away from the surface. Here, the experimental data were supported by a detailed simulation of the probe-object coupling through the superlens structure. In contrast to our sample, however, these results refer to an asymmetric superlens, where the top layer is omitted. In the same work,

a symmetric structure including the top layer was investigated as well, where, in agreement with our results, the signal strength of the superlensed images was found to be largest at  $h = 0$ . Here, maximum signal for  $h \neq 0$  can only be expected when the real permittivity  $\varepsilon'$  of the top layer becomes negative. This results in resonant coupling between this layer and the tip, as we discussed in Section 4.2.3. For the symmetric superlens, however, this is spectrally well separated from the imaging effect, which in particular applies to the GaAs superlens (see Figure 8.1.1).

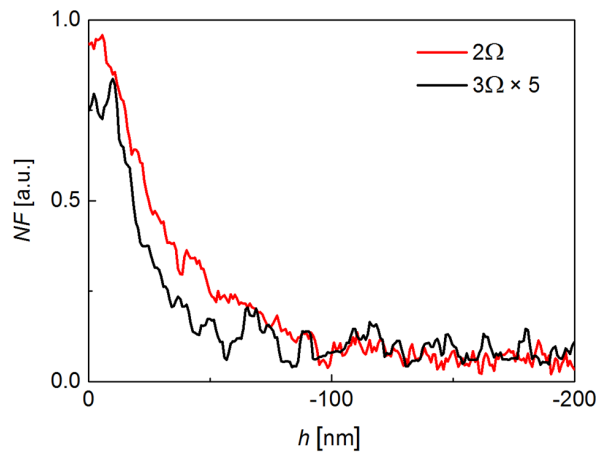


**Figure 8.5.1:** Near-field signals  $NF_{2\Omega}(h)$  and  $NF_{3\Omega}(h)$  as a function of the probe's distance  $h$  from the surface of superlens (Sample 3.2; see Section 8.1). Measurements were obtained at  $\lambda = 21.7 \mu\text{m}$  at the position of the gold-stripes underneath the superlens.

Note that  $NF_{3\Omega}(h)$  provides a steeper decay than  $NF_{2\Omega}(h)$  in the experiment. This is in agreement with theory (see Figure 4.4.3), where for the calculations the tapping amplitude  $A$  of the tip was assumed to be much smaller than the curvature radius  $a$  of the s-SNOM probe. According to these calculations the signals are expected to reach zero at  $h \approx a$ , where  $a$  of the AFM tips used in the near-field studies is approximately 50 nm. In contrast, we observe a decay within not less than 100 nm. This is due to the fact that in the experiment  $A$  is about 80 nm (peak to peak), which is even larger than  $a$ . It was shown in reference [71] that this results in a less steep decrease, whereas the fact that  $NF_{3\Omega}(h)$  decays faster than  $NF_{2\Omega}(h)$  remains valid.

We emphasize that the signal decay within  $\approx 100$  nm applies to all investigations presented here, Figure 8.5.1 just providing an example. This is important, proving that we measure near-field signals free of unwanted far-field background.

## 8.6 Bandwidth of superlensing - discussion

At the end of Section 8.3.2, we mention that the experimentally observed operational bandwidth of the plasmonic GaAs superlens ( $\Delta\lambda/\lambda_{\text{SL}} \approx 25\%$ ) is considerably larger than of other infrared superlenses ( $\Delta\lambda/\lambda_{\text{SL}} \approx 10\%$ ) studied in the past [36, 37, 38]. Here, we refer to systems consisting of three layers, following the same concept as we do in this work. Despite this similarity, the effect is induced by a phonon resonance in all of these investigations, whereas we exploit the Drude response of free electrons in a doped layer. Our experimental results of the spectral behavior (Sample 3.2) are presented in Section 8.3.2. In the following, we exemplarily compare the plasmonic GaAs superlens to a phonon based version consisting of perovskites [37], namely bismuth ferrite ( $\text{BiFeO}_3$ ) and strontium titanate ( $\text{SrTiO}_3$ ; middle layer), in order to qualitatively discuss the origin of the different bandwidths. Both superlenses are resonant in the mid-infrared, with calculated values of  $\lambda_{\text{SL}} = 20 \mu\text{m}$  (GaAs) and  $14 \mu\text{m}$  (perovskites).

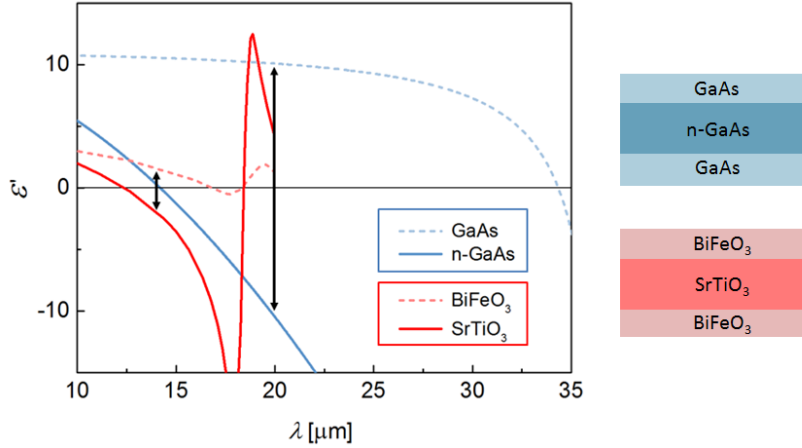


**Figure 8.6.1:** Real permittivities  $\epsilon'$  of the constituents of the plasmonic doped GaAs based superlens (Sample 3.2, see Section 8.1) and a phononic perovskite based superlens (values extracted from [37]). In each case, the solid line represents the middle layer, providing negative  $\epsilon'$ . Superlensing conditions are indicated by black arrows.

At first, we take a look at the real permittivity  $\epsilon'$  of the two superlens structures, since this is what determines the respective superlensing conditions (see Figure 8.6.1). As mentioned many times in this thesis, the resonance wavelength  $\lambda_{\text{SL}}$  is given by the condition  $\epsilon'_B(\lambda_{\text{SL}}) = -\epsilon'_A(\lambda_{\text{SL}})$ , where A and B refer to the outer layers and the middle layer, respectively. For the two cases discussed here, this is  $\epsilon'_{\text{n-GaAs}}(\lambda_{\text{SL}}) = -\epsilon'_{\text{GaAs}}(\lambda_{\text{SL}}) \approx -10$  and  $\epsilon'_{\text{SrTiO}_3}(\lambda_{\text{SL}}) = -\epsilon'_{\text{BiFeO}_3}(\lambda_{\text{SL}}) \approx -2$ . In Figure 8.6.2, the ratios  $R(\lambda) = \epsilon'_B(\lambda)/\epsilon'_A(\lambda)$  are depicted, where  $R(\lambda_{\text{SL}}) = -1$  applies at resonance. Here, a slow change of  $R(\lambda)$  corresponds

to a large spectral width of the superlensing effect, since the resonance condition is well fulfilled in the spectral proximity of the center wavelength. In this regard, the comparably large absolute values of  $\varepsilon'_{\text{n-GaAs}}(\lambda_{\text{SL}})$  and  $\varepsilon'_{\text{GaAs}}(\lambda_{\text{SL}})$  and the slow variation of  $\varepsilon'_{\text{GaAs}}(\lambda)$  favor a large bandwidth of the GaAs superlens. In order to provide a more quantitative picture, we consider the superlensing condition to be fulfilled as long as  $R = -1.5 \dots -0.5$ . As can be seen in Figure 8.6.2, this region is considerably larger for the GaAs system as compared to the perovskite superlens, confirming the experimental observation.

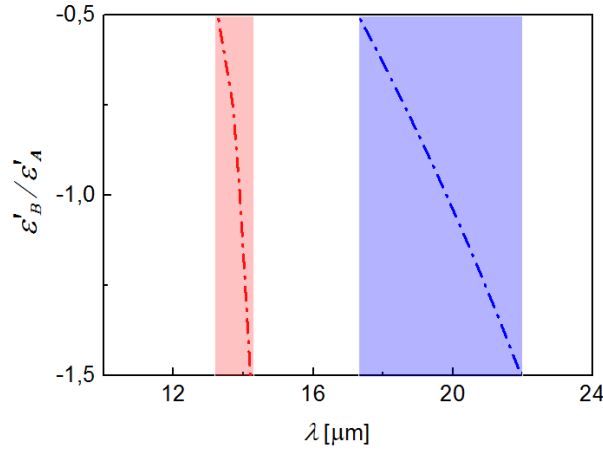


**Figure 8.6.2:** Ratio  $R$  between real permittivities of the middle layer ( $\varepsilon'_B$ ) and the outer layers ( $\varepsilon'_A$ ), depicted both for the GaAs superlens (blue) and the perovskite superlens (red). At resonance,  $R = \varepsilon'_B / \varepsilon'_A = -1$ . Within the colored regions, the deviation from this condition is less than 50% for the respective case.

Another issue impacting the bandwidth is dissipation within the superlens. This is seen in Figure 8.6.3, where we compare the calculated transfer function  $|T_{\text{SL}}|^2$  of the GaAs superlens (Sample 3.2, see Section 8.1) to a fictitious sample with artificially reduced values of the permittivity's imaginary part  $\varepsilon''_{\text{n-GaAs}}$  of the middle doped layer. Obviously, dissipation comes both with a broader profile but also with a decrease of transmission at large wavenumbers, reducing the imaging capability. Nevertheless, in spite of exhibiting clearly different values of  $\varepsilon''(\lambda_{\text{SL}})$ , the obtainable resolution for the plasmonic GaAs superlens ( $\varepsilon_{\text{n-GaAs}}(\lambda_{\text{SL}}) \approx -10 + 4i$ ) and the phononic perovskite superlens ( $\varepsilon_{\text{SrTiO}_3}(\lambda_{\text{SL}}) \approx -2 + 0.5i$ ) appears to be similar. Here, it is important to notice that the smallest observable structure size does not exclusively depend on  $\varepsilon''$ , but on the ratio  $\varepsilon''/\varepsilon'$  (see Equation 3.2.9)<sup>10</sup>.

Remarkably, small losses come with an unexpected disadvantage. As can be seen in Figure 8.6.3, the simulation with reduced  $\varepsilon''$  yields transmission divergences at wavelengths close to the superlens resonance (the two red lines at  $\lambda \approx 20 \mu\text{m}$ , reaching large values of

<sup>10</sup>Note, however, that for quantitative accuracy  $\varepsilon'' \ll |\varepsilon'|$  is required, which is not the case here.

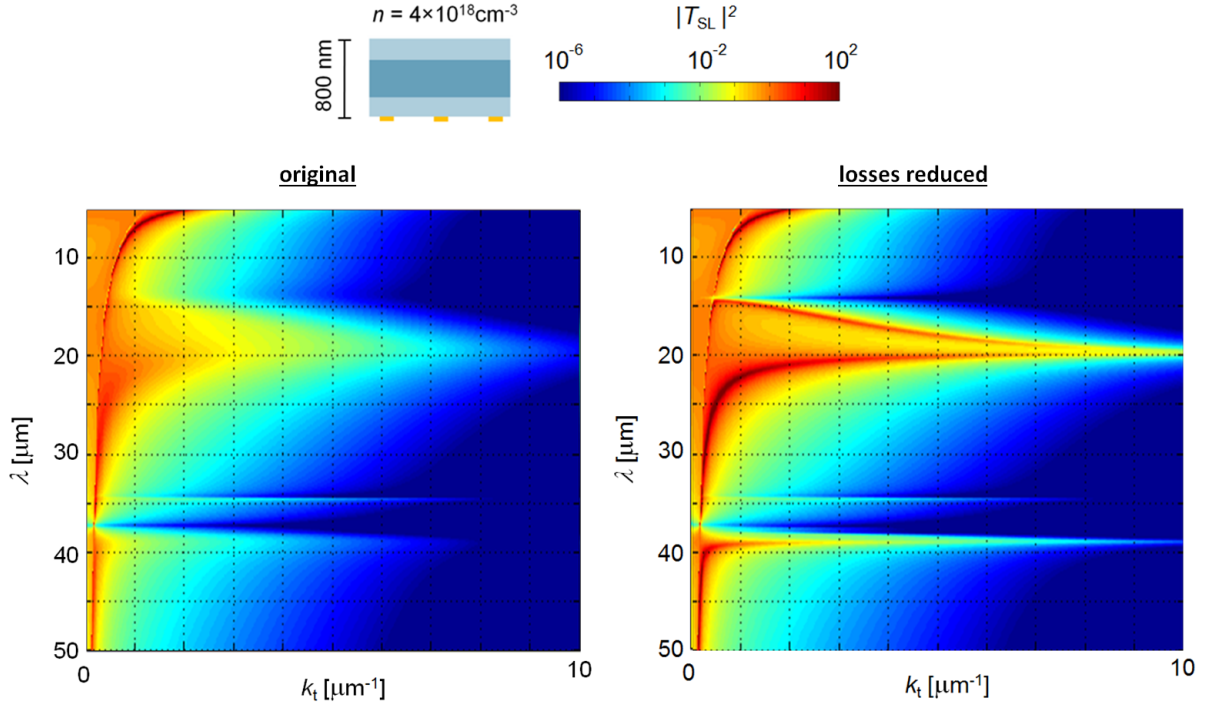


**Figure 8.6.3:** Left: calculated transfer function  $|T_{\text{SL}}|^2$  of the GaAs superlens (Sample 3.2, see Section 8.1), taking into account the complex permittivity  $\varepsilon = \varepsilon' + \varepsilon''$  of the three layers. Right: Losses of the middle doped layer artificially reduced,  $\varepsilon''_{\text{n-GaAs}} \rightarrow \varepsilon''_{\text{n-GaAs}}/10$ .

$k_t$ ). Hence, for a given  $\lambda$  in this spectral region, a certain value of  $k_t$  is strongly enhanced, possibly introducing artifacts that dominate the image. These divergences correspond to coupled plasmon resonances at the interfaces of the doped layer, which are removed with increasing dissipation [35]. Hence, a certain degree of absorption is vital for the performance of the superlens.

Having stated two possible broadening mechanisms for the superlens operation, a more detailed analysis is required for a deeper understanding. However, this is beyond the scope of this work.



## 9 Conclusion and outlook

In summary, it was shown that a trilayer structure consisting of highly n-doped GaAs sandwiched between intrinsic layers is capable to act as a plasmonic near-field superlens in the mid-infrared spectral region [26]. This system essentially benefits from its spectral tunability, where the Drude response of the conducting layer can be controlled by the doping level. The present work is the first experimental evidence of such a frequency-adjustable superlens.

Applying scattering-type scanning near-field optical microscopy (s-SNOM) in combination with a frequency-tunable free-electron laser as radiation source, we observed resonantly enhanced near-field transmission with subwavelength spatial resolution by imaging gold objects underneath the GaAs superlens. Here, an electron concentration of  $4 \times 10^{18} \text{cm}^{-3}$ , determined by FTIR pre-characterization, provided a resonant wavelength of  $22 \mu\text{m}$ . This is in excellent agreement with theory, where the Drude-Lorentz model was applied to calculate the transfer function of the layered slab. In general, the superlensing wavelength increases with decreasing the electron density, induced by a shift of the plasma frequency. Since the electron concentration in the case described above is close to the achievable maximum by doping with silicon, a superlensing wavelength of about  $20 \mu\text{m}$  can be regarded as the high frequency limit of such a system. According to our calculations, we expect that superlensing with doped GaAs is possible over a wide infrared spectral range reaching well into the terahertz regime. The losses are expected to be rather constant at operational conditions.

While investigations with slightly different doping concentrations, also presented in this thesis, provide first indications of the accompanied spectral shift of the effect, a clear demonstration is lacking so far. To this end, the investigation of a sample providing superlensing on the long wavelength side of the GaAs Reststrahlen band would be of interest, where the resonance is spectrally clearly separated from the observations made in this work. For instance, an electron density of  $3 \times 10^{17} \text{cm}^{-3}$  will result in a superlensing wavelength of about  $80 \mu\text{m}$ . Even though we expect dissipation at resonance to be somewhat larger as compared to higher doping concentrations, the clear superlensing signatures obtained in this work suggest that going to these long wavelengths is promising. Note, however, that



such experiments are challenging, since both the scattering cross section of the s-SNOM probe and the sensitivity of photodetectors are decreased in the terahertz region. Another aspect to be tackled in the future could be the improvement of the superlens performance by subdividing the structure into thinner layers, i.e. a sequence of doped and intrinsic GaAs with the same total thickness as the trilayer superlens. It was theoretically discussed [35, 46] that distributing the amplification process of evanescent waves reduces the effects of absorption. Such a thin layered superlens structure is easy to achieve by MBE growth, and by choosing the doping level to be the same as for the investigations presented here, there is no need to experimentally search for the spectral position of the resonance.

Spectral tunability and compatibility with semiconductor technology give rise to practical application opportunities of the plasmonic GaAs superlens. As mentioned, a good performance can be expected within a large part of the mid-infrared and terahertz range. Designing devices for this region that is less developed with respect to technology, is very valuable. Here, our superlens might be useful as a building block of devices that exploit plasmonic coupling of the radiation field to small structures. For GaAs based III-V semiconductor compounds, even monolithic integration is possible. Taking advantage of the resonant character of the superlensing effect, one might think of an application as a spectral filter, where only desired wavelengths exhibit enhanced coupling. In this context, it depends on the particular case if the rather large bandwidth, which was discussed in the results section, is of use or not. Aside from these general considerations, there is immediate application potential for SNOM studies of buried objects. In particular, this applies to nanoelectronic objects which are *necessarily* buried below a layer of intrinsic GaAs in order to avoid depletion due to surface fields [112] or imposed by the penetration depth of ion implantation [113]. Introducing a doped layer into the capping, thereby converting the intrinsic layer into a superlens, enables enhanced subwavelength spatial resolution and contrast of otherwise blurred images at a designed wavelength. For example, near-field studies of buried quantum dots [114], doping profiles [110] and charge carriers in a field-effect transistor [115] can be significantly improved by this concept. Concerning the latter two, a superlens operating in the far-infrared enables mapping buried distributions of rather low charge carrier densities with low plasma frequencies.

While doped GaAs has been a convenient choice for this proof-of-principle study of a frequency adjustable plasmonic superlens, the concept should be easily transferable to other materials. Here, shorter superlensing wavelengths can be obtained by materials supporting higher dopings, better spatial resolution may be accomplished in case of less absorption. Besides, the question of suitability is of course also connected to availability and application potential. In the past years, doped semiconductors have already been multiply suggested

as spectrally adjustable plasmonic devices [40, 65, 66, 67]. Here, indium arsenide (InAs) is an excellent candidate [66] to expand the accessible spectral range of superlensing towards shorter wavelengths and to improve the obtainable resolution. Due to a small electron effective mass and the feasibility of very high doping, a plasma wavelength as short as about  $5 \mu\text{m}$  was obtained [65], which is in proximity to the expected superlensing wavelength. The high electron mobility in InAs, in addition, should give rise to a good superlensing performance. While traditional semiconductors like GaAs and InAs provide superlensing potential within a large part of the mid- and far-infrared spectral range, the near-infrared region can be explored by transparent conducting oxides (TCO's). A good performance is expected to be obtained with aluminum-zinc-oxide (AZO), indium-tin-oxide (ITO) and gallium-zinc-oxide (GZO), for instance [40]. This work may be the starting point for such related projects.



# Bibliography

- [1] P. E. Batson, N. Dellby, and O. L. Krivanek. Sub-ångstrom resolution using aberration corrected electron optics. *Nature*, 418:617–620, 2002.
- [2] D. M. Eigler and E. K. Schweizer. Positioning single atoms with a scanning tunnelling microscope. *Nature*, 344:524–526, 1990.
- [3] F. J. Giessibl. Atomic Resolution of the Silicon (111)-(7x7) Surface by Atomic Force Microscopy. *Science*, 267:68–71, 1995.
- [4] E. Abbe. Beiträge zur Theorie des Mikroskops und der mikroskopischen Wahrnehmung. *Archiv für mikroskopische Anatomie*, 9:413–418, 1873.
- [5] S. M. Mansfield and G. S. Kino. Solid immersion microscope. *Applied Physics Letters*, 57:2615–2616, 1990.
- [6] S. Hell and E. H. K. Stelzer. Properties of a 4Pi confocal fluorescence microscope. *J. Opt. Soc. Am. A*, 9:2159–2166, 1992.
- [7] T. A. Klar and S. W. Hell. Subdiffraction resolution in far-field fluorescence microscopy. *Opt. Lett.*, 24:954–956, 1999.
- [8] A. Lewis, M. Isaacson, A. Harootunian, and A. Muray. Development of a 500 Å spatial resolution light microscope. *Ultramicroscopy*, 13:227–231, 1984.
- [9] M. Specht, J. D. Pedarnig, W. M. Heckl, and T. W. Hänsch. Scanning plasmon near-field microscope. *Phys. Rev. Lett.*, 68:476–479, 1992.
- [10] H. Sahoo. Fluorescent labeling techniques in biomolecules: a flashback. *RSC Adv.*, 2:7017–7029, 2012.
- [11] J. Wessel. Surface-enhanced optical microscopy. *J. Opt. Soc. Am. B*, 2:1538–1541, 1985.
- [12] Y. Inouye and S. Kawata. Near-field scanning optical microscope with a metallic probetip. *Opt. Lett.*, 19:159–161, 1994.

- [13] D. W. Pohl, W. Denk, and M. Lanz. Optical stethoscopy: Image recording with resolution  $\lambda/20$ . *Applied Physics Letters*, 44:651–653, 1984.
- [14] E. Betzig and J. K. Trautman. Near-Field Optics: Microscopy, Spectroscopy, and Surface Modification Beyond the Diffraction Limit. *Science*, 257:189–195, 1992.
- [15] B. Knoll and F. Keilmann. Electromagnetic fields in the cutoff regime of tapered metallic waveguides. *Optics Communications*, 162:177–181, 1999.
- [16] F. Huth, A. Govyadinov, S. Amarie, W. Nuansing, F. Keilmann, and R. Hillenbrand. Nano-FTIR Absorption Spectroscopy of Molecular Fingerprints at 20 nm Spatial Resolution. *Nano Letters*, 12:3973–3978, 2012.
- [17] P. Hermann, A. Hoehl, P. Patoka, F. Huth, E. Rühl, and G. Ulm. Near-field imaging and nano-Fourier-transform infrared spectroscopy using broadband synchrotron radiation. *Opt. Express*, 21:2913–2919, 2013.
- [18] S. Schneider, J. Seidel, S. Grafström, L. M. Eng, S. Winnerl, D. Stehr, and M. Helm. Impact of optical in-plane anisotropy on near-field phonon polariton spectroscopy. *Applied Physics Letters*, 90:143101, 2007.
- [19] S. C. Kehr, M. Cebula, O. Mieth, T. Härtling, J. Seidel, S. Grafström, L. M. Eng, S. Winnerl, D. Stehr, and M. Helm. Anisotropy Contrast in Phonon-Enhanced Apertureless Near-Field Microscopy Using a Free-Electron Laser. *Phys. Rev. Lett.*, 100:256403, 2008.
- [20] R. Krutokhvostov, A. A. Govyadinov, J. M. Stiegler, F. Huth, A. Chuvilin, P. S. Carney, and R. Hillenbrand. Enhanced resolution in subsurface near-field optical microscopy. *Opt. Express*, 20:593–600, 2012.
- [21] A. P. Engelhardt, B. Hauer, and T. Taubner. Visibility of weak contrasts in subsurface scattering near-field microscopy. *Ultramicroscopy*, 126:40–43, 2013.
- [22] J. B. Pendry. Negative Refraction Makes a Perfect Lens. *Phys. Rev. Lett.*, 85:3966–3969, 2000.
- [23] J. B. Pendry and D. R. Smith. The Quest for the Superlens. *Scientific American*, 295:60–67, 2006.
- [24] V. A. Podolskiy and E. E. Narimanov. Near-sighted superlens. *Opt. Lett.*, 30:75–77, 2005.

- [25] H. Liu, B. Wang, L. Ke, J. Deng, C. C. Chum, S. L. Teo, L. Shen, S. A. Maier, and J. Teng. High Aspect Subdiffraction-Limit Photolithography via a Silver Superlens. *Nano Letters*, 12:1549–1554, 2012.
- [26] M. Fehrenbacher, S. Winnerl, H. Schneider, J. Döring, S. C. Kehr, L. M. Eng, Y. Huo, O. G. Schmidt, K. Yao, Y. Liu, and M. Helm. Plasmonic Superlensing in Doped GaAs. *Nano Letters*, 15:1057–1061, 2015.
- [27] M. Born and E. Wolf. *Principles of Optics*. Cambridge University Press, 1999.
- [28] J. D. Jackson. *Classical electrodynamics*. Wiley, 1975.
- [29] V. Veselago. The electrodynamics of substances with simultaneously negative values of  $\varepsilon$  and  $\mu$ . *Sov. Phys. Uspekhi*, 10:509–514, 1968.
- [30] S. A. Ramakrishna. Physics of negative refractive index materials. *Reports on Progress in Physics*, 68:449–521, 2005.
- [31] J. T. Shen and P. M. Platzman. Near field imaging with negative dielectric constant lenses. *Applied Physics Letters*, 80:3286–3288, 2002.
- [32] X. Zhang and Z. Liu. Superlenses to overcome the diffraction limit. *Nature Materials*, 7:435–441, 2008.
- [33] D. R. Smith, D. Schurig, M. Rosenbluth, S. Schultz, S. A. Ramakrishna, and J. B. Pendry. Limitations on subdiffraction imaging with a negative refractive index slab. *Applied Physics Letters*, 82:1506–1508, 2003.
- [34] C. M. Soukoulis, S. Linden, and M. Wegener. Negative Refractive Index at Optical Wavelengths. *Science*, 315:47–49, 2007.
- [35] S. A. Ramakrishna, J. B. Pendry, M. C. K. Wiltshire, and W. J. Stewart. Imaging the near field. *Journal of Modern Optics*, 50:1419–1430, 2003.
- [36] T. Taubner, D. Korobkin, Y. Urzhumov, G. Shvets, and R. Hillenbrand. Near-Field Microscopy Through a SiC Superlens. *Science*, 313:1595, 2006.
- [37] S. C. Kehr, Y. M. Liu, L. W. Martin, P. Yu, M. Gajek, S.-Y. Yang, C.-H. Yang, M. T. Wenzel, R. Jacob, H.-G. von Ribbeck, M. Helm, X. Zhang, L. M. Eng, and R. Ramesh. Near-field examination of perovskite-based superlenses and superlens-enhanced probe-object coupling. *Nature Communications*, 2:249, 2011.

- [38] S. C. Kehr, P. Yu, Y. Liu, M. Parzefall, A. I. Khan, R. Jacob, M. T. Wenzel, H.-G. von Ribbeck, M. Helm, X. Zhang, L. M. Eng, and R. Ramesh. Microspectroscopy on perovskite-based superlenses. *Opt. Mater. Express*, 1:1051–1060, 2011.
- [39] S. A. Ramakrishna, J. B. Pendry, D. Schurig, D. R. Smith, and S. Schultz. The asymmetric lossy near-perfect lens. *Journal of Modern Optics*, 49:1747–1762, 2002.
- [40] P. R. West, S. Ishii, G. V. Naik, N. K. Emani, V. M. Shalaev, and A. Boltasseva. Searching for better plasmonic materials. *Laser & Photonics Reviews*, 4:795–808, 2010.
- [41] D. E. Aspnes and A. A. Studna. Dielectric functions and optical parameters of Si, Ge, GaP, GaAs, GaSb, InP, InAs, and InSb from 1.5 to 6.0 eV. *Phys. Rev. B*, 27:985–1009, 1983.
- [42] H. Raether. *Surface Plasmons on Smooth and Rough Surfaces and on Gratings*. Springer, 1988.
- [43] S. Hayashi and T. Okamoto. Plasmonics: visit the past to know the future. *Journal of Physics D: Applied Physics*, 45:433001, 2012.
- [44] C. Kittel. *Introduction to Solid State Physics*. Wiley, 1986.
- [45] S. Kawata, Y. Inouye, and P. Verma. Plasmonics for near-field nano-imaging and superlensing. *Nature Photonics*, 3:388–394, 2009.
- [46] J. B. Pendry and S. A. Ramakrishna. Refining the perfect lens. *Physica B: Condensed Matter*, 338:329–332, 2003.
- [47] Z. Fei, G. O. Andreev, W. Bao, L. M. Zhang, A. S. McLeod, C. Wang, M. K. Stewart, Z. Zhao, G. Dominguez, M. Thiemens, M. M. Fogler, M. J. Tauber, A. H. Castro-Neto, C. N. Lau, F. Keilmann, and D. N. Basov. Infrared Nanoscopy of Dirac Plasmons at the Graphene-SiO<sub>2</sub> Interface. *Nano Letters*, 11:4701–4705, 2011.
- [48] J. B. Pendry, A. J. Holden, W. J. Stewart, and I. Youngs. Extremely Low Frequency Plasmons in Metallic Mesostructures. *Phys. Rev. Lett.*, 76:4773–4776, 1996.
- [49] J. B. Pendry, A. J. Holden, D. J. Robbins, and W. J. Stewart. Low frequency plasmons in thin-wire structures. *Journal of Physics: Condensed Matter*, 10:4785–4809, 1998.

- [50] J. B. Pendry, A. J. Holden, D. J. Robbins, and W. J. Stewart. Magnetism from conductors and enhanced nonlinear phenomena. *IEEE Transactions on Microwave Theory and Techniques*, 47:2075–2084, 1999.
- [51] D. R. Smith, W. J. Padilla, D. C. Vier, S. C. Nemat-Nasser, and S. Schultz. Composite Medium with Simultaneously Negative Permeability and Permittivity. *Phys. Rev. Lett.*, 84:4184–4187, 2000.
- [52] R. A. Shelby, D. R. Smith, and S. Schultz. Experimental Verification of a Negative Index of Refraction. *Science*, 292:77–79, 2001.
- [53] G. V. Eleftheriades, A. K. Iyer, and P. C. Kremer. Planar negative refractive index media using periodically L-C loaded transmission lines. *IEEE Transactions on Microwave Theory and Techniques*, 50:2702–2712, 2002.
- [54] A. Grbic and G. V. Eleftheriades. Overcoming the Diffraction Limit with a Planar Left-Handed Transmission-Line Lens. *Phys. Rev. Lett.*, 92:117403, 2004.
- [55] M. Wiltshire, J. Hajnal, J. Pendry, D. Edwards, and C. Stevens. Metamaterial endoscope for magnetic field transfer: near field imaging with magnetic wires. *Opt. Express*, 11:709–715, 2003.
- [56] G. Dolling, M. Wegener, C. M. Soukoulis, and S. Linden. Negative-index metamaterial at 780 nm wavelength. *Opt. Lett.*, 32:53–55, 2007.
- [57] Z. Liu, N. Fang, T.-J. Yen, and X. Zhang. Rapid growth of evanescent wave by a silver superlens. *Applied Physics Letters*, 83:5184–5186, 2003.
- [58] N. Fang, H. Lee, C. Sun, and X. Zhang. Sub-Diffraction-Limited Optical Imaging with a Silver Superlens. *Science*, 308:534–537, 2005.
- [59] P. Li, T. Wang, H. Böckmann, and T. Taubner. Graphene-Enhanced Infrared Near-Field Microscopy. *Nano Letters*, 14:4400–4405, 2014.
- [60] P. Li and T. Taubner. Multi-wavelength superlensing with layered phonon-resonant dielectrics. *Opt. Express*, 20:11787–11795, 2012.
- [61] X. Yang, Y. Liu, J. Ma, J. Cui, H. Xing, W. Wang, C. Wang, and X. Luo. Broadband super-resolution imaging by a superlens with unmatched dielectric medium. *Opt. Express*, 16:19686–19694, 2008.



- [62] P. Li and T. Taubner. Broadband Subwavelength Imaging Using a Tunable Graphene-Lens. *ACS Nano*, 6:10107–10114, 2012.
- [63] W. Cai, D. A. Genov, and V. M. Shalaev. Superlens based on metal-dielectric composites. *Phys. Rev. B*, 72:193101, 2005.
- [64] D. Lu, J. Kan, E. E. Fullerton, and Z. Liu. Tunable surface plasmon polaritons in Ag composite films by adding dielectrics or semiconductors. *Applied Physics Letters*, 98:243114, 2011.
- [65] S. Law, D. C. Adams, A. M. Taylor, and D. Wasserman. Mid-infrared designer metals. *Opt. Express*, 20:12155–12165, 2012.
- [66] S. Law, V. Podolskiy, and D. Wasserman. Towards nano-scale photonics with micro-scale photons: the opportunities and challenges of mid-infrared plasmonics. *Nanophotonics*, 2:103–130, 2013.
- [67] G. V. Naik, V. M. Shalaev, and A. Boltasseva. Alternative Plasmonic Materials: Beyond Gold and Silver. *Advanced Materials*, 25:3264–3294, 2013.
- [68] G. Binnig, H. Rohrer, C. Gerber, and E. Weibel. Tunneling through a controllable vacuum gap. *Applied Physics Letters*, 40:178–180, 1982.
- [69] G. Binnig, C. F. Quate, and C. Gerber. Atomic Force Microscope. *Phys. Rev. Lett.*, 56:930–933, 1986.
- [70] E. A. Ash and G. Nicholls. Super-resolution Aperture Scanning Microscope. *Nature*, 237:510–512, 1972.
- [71] B. Knoll and F. Keilmann. Enhanced dielectric contrast in scattering-type scanning near-field optical microscopy. *Optics Communications*, 182:321–328, 2000.
- [72] C. F. Bohren and D. R. Huffman. *Absorption and scattering of light by small particles*. Wiley, 1998.
- [73] T. Taubner. *Infrarotspektroskopie im Nahfeld einer Tastspitze*. PhD thesis, TU München, 2004.
- [74] M. A. Ordal, L. L. Long, R. J. Bell, S. E. Bell, R. R. Bell, R. W. Alexander, and C. A. Ward. Optical properties of the metals Al, Co, Cu, Au, Fe, Pb, Ni, Pd, Pt, Ag, Ti, and W in the infrared and far infrared. *Appl. Opt.*, 22:1099–1119, 1983.

- [75] B. Knoll and F. Keilmann. Infrared conductivity mapping for nanoelectronics. *Applied Physics Letters*, 77:3980–3982, 2000.
- [76] N. Ocelic and R. Hillenbrand. Subwavelength-scale tailoring of surface phonon polaritons by focused ion-beam implantation. *Nature Materials*, 3:606–609, 2004.
- [77] T. Taubner, F. Keilmann, and R. Hillenbrand. Nanomechanical Resonance Tuning and Phase Effects in Optical Near-Field Interaction. *Nano Letters*, 4:1669–1672, 2004.
- [78] R. Hillenbrand, T. Taubner, and F. Keilmann. Phonon-enhanced light-matter interaction at the nanometre scale. *Nature*, 418:159–162, 2002.
- [79] R. Esteban, R. Vogelgesang, and K. Kern. Tip-substrate interaction in optical near-field microscopy. *Phys. Rev. B*, 75:195410, 2007.
- [80] R. Esteban, R. Vogelgesang, and K. Kern. Full simulations of the apertureless scanning near field optical microscopy signal: achievable resolution and contrast. *Opt. Express*, 17:2518–2529, 2009.
- [81] S. C. Schneider. *Scattering Scanning Near-Field Optical Microscopy on Anisotropic Dielectrics*. PhD thesis, TU Dresden, 2007.
- [82] R. Hillenbrand. *Nahfeldoptische Amplituden- und Phasenkontrastmikroskopie zur nanoskopischen optischen Abbildung von Materialkontrast und optisch resonanten Partikeln*. PhD thesis, TU München, 2001.
- [83] S. Aubert, A. Bruyant, S. Blaize, R. Bachelot, G. Lerondel, S. Hudlet, and P. Royer. Analysis of the interferometric effect of the background light in apertureless scanning near-field optical microscopy. *J. Opt. Soc. Am. B*, 20:2117–2124, 2003.
- [84] L. Gomez, R. Bachelot, A. Bouhelier, G. P. Wiederrecht, S. Chang, S. K. Gray, F. Hua, S. Jeon, J. A. Rogers, M. E. Castro, S. Blaize, I. Stefanon, G. Lerondel, and P. Royer. Apertureless scanning near-field optical microscopy: a comparison between homodyne and heterodyne approaches. *J. Opt. Soc. Am. B*, 23:823–833, 2006.
- [85] N. Ocelic, A. Huber, and R. Hillenbrand. Pseudoheterodyne detection for background-free near-field spectroscopy. *Applied Physics Letters*, 89:101124, 2006.
- [86] B. Deutsch, R. Hillenbrand, and L. Novotny. Near-field amplitude and phase recovery using phase-shifting interferometry. *Opt. Express*, 16:494–501, 2008.

- [87] J. S. Blakemore. Semiconducting and other major properties of gallium arsenide. *Journal of Applied Physics*, 53:R123–R181, 1982.
- [88] W. Cochran, S. J. Fray, F. A. Johnson, J. E. Quarrington, and N. Williams. Lattice Absorption in Gallium Arsenide. *Journal of Applied Physics*, 32:2102–2106, 1961.
- [89] A. A. Kukharskii. Plasmon-phonon coupling in GaAs. *Solid State Communications*, 13:1761–1765, 1973.
- [90] P. G. Huggard, J. A. Cluff, G. P. Moore, C. J. Shaw, S. R. Andrews, S. R. Keiding, E. H. Linfield, and D. A. Ritchie. Drude conductivity of highly doped GaAs at terahertz frequencies. *Journal of Applied Physics*, 87:2382–2385, 2000.
- [91] J. Lloyd-Hughes. Generalized conductivity model for polar semiconductors at terahertz frequencies. *Applied Physics Letters*, 100:122103, 2012.
- [92] P. O. Vaccaro. Epitaxial growth and amphoteric doping on GaAs (n11)A-oriented substrates. In *Indium Phosphide and Related Materials, IEEE International Conference*, pages 47–50, 2001.
- [93] J. H. Neave, P. J. Dobson, J. J. Harris, P. Dawson, and B. A. Joyce. Silicon doping of MBE-grown GaAs films. *Applied Physics A*, 32:195–200, 1983.
- [94] S. M. Sze. *Physics of Semiconductor Devices*. Wiley, 1981.
- [95] A. Raymond, J. L. Robert, and C. Bernard. The electron effective mass in heavily doped GaAs. *Journal of Physics C: Solid State Physics*, 12:2289–2293, 1979.
- [96] H. Lee, Y. Xiong, N. Fang, W. Srituravanich, S. Durant, M. Ambati, C. Sun, and X. Zhang. Realization of optical superlens imaging below the diffraction limit. *New Journal of Physics*, 7:255, 2005.
- [97] L. J. van der Pauw. A method of measuring the resistivity and Hall coefficient on lamellae of arbitrary shape. *Philips Technical Review*, 20:220–224, 1958.
- [98] P. Blood and J. W. Orton. *The Electrical Characterization of Semiconductors: Majority Carriers and Electron States*. Academic Press, 1992.
- [99] J. F. Lin, S. S. Li, L. C. Linares, and K. W. Teng. Theoretical analysis of Hall factor and Hall mobility in p-type silicon. *Solid-State Electronics*, 24:827–833, 1981.

- [100] I. G. Kirnas, P. M. Kurilo, P. G. Litovchenko, V. S. Lutsyak, and V. M. Nitsovich. Concentration dependence of the Hall factor in n-type silicon. *Physica Status Solidi (A)*, 23:K123–K127, 1974.
- [101] G. Deinzer and D. Strauch. Two-phonon infrared absorption spectra of germanium and silicon calculated from first principles. *Phys. Rev. B*, 69:045205, 2004.
- [102] M. Ikezawa and M. Ishigame. Far-Infrared Absorption Due to the Two-Phonon Difference Process in Si. *Journal of the Physical Society of Japan*, 50:3734–3738, 1981.
- [103] D. Sarid. *Scanning Force Microscopy*. Oxford University Press, 1991.
- [104] J. E. Jones. On the Determination of Molecular Fields. II. From the Equation of State of a Gas. *Royal Society of London Proceedings Series A*, 106:463–477, 1924.
- [105] E. Meyer. Atomic force microscopy. *Progress in Surface Science*, 41:3–49, 1992.
- [106] O. Wolter, T. Bayer, and J. Greschner. Micromachined silicon sensors for scanning force microscopy. *Journal of Vacuum Science & Technology B*, 9:1353–1357, 1991.
- [107] R. Jacob. *Scanning near-field infrared microspectroscopy on semiconductor structures*. PhD thesis, TU Dresden, 2011.
- [108] P. G. O’Shea and H. P. Freund. Free-Electron Lasers: Status and Applications. *Science*, 292:1853–1858, 2001.
- [109] C. A. Brau. *Free-Electron Lasers*. Academic Press, 1990.
- [110] R. Jacob, S. Winnerl, H. Schneider, M. Helm, M. T. Wenzel, H.-G. von Ribbeck, L. M. Eng, and S. C. Kehr. Quantitative determination of the charge carrier concentration of ion implanted silicon by IR-near-field spectroscopy. *Opt. Express*, 18:26206–26213, 2010.
- [111] V. Giannini, A. I. Fernández-Domínguez, S. C. Heck, and S. A. Maier. Plasmonic Nanoantennas: Fundamentals and Their Use in Controlling the Radiative Properties of Nanoemitters. *Chemical Reviews*, 111:3888–3912, 2011.
- [112] W. R. Buchwald, J. W. Cleary, and J. Hendrickson. Surface depletion mediated control of inter-sub-band absorption in GaAs/AlAs semiconductor quantum well systems. *Applied Physics Letters*, 100:051110, 2012.

- [113] D. K. Brice. Ion implantation depth distributions: energy deposition into atomic processes and ion locations. *Applied Physics Letters*, 16:103–106, 1970.
- [114] R. Jacob, S. Winnerl, M. Fehrenbacher, J. Bhattacharyya, H. Schneider, M. T. Wenzel, H.-G. von Ribbeck, L. M. Eng, P. Atkinson, O. G. Schmidt, and M. Helm. Intersublevel Spectroscopy on Single InAs-Quantum Dots by Terahertz Near-Field Microscopy. *Nano Letters*, 12:4336–4340, 2012.
- [115] A. J. Huber, F. Keilmann, J. Wittborn, J. Aizpurua, and R. Hillenbrand. Terahertz Near-Field Nanoscopy of Mobile Carriers in Single Semiconductor Nanodevices. *Nano Letters*, 8:3766–3770, 2008.

# Acknowledgement

I want to say *thank you* to

Manfred Helm - for supervision and constructive feedback.

Harald Schneider - for extensive discussions and pleasant working atmosphere.

Stephan Winnerl - for lots of patience and even more good advice.

Thomas Taubner - for reviewing this thesis.

Lukas Eng, Susanne Kehr, Hans-Georg von Ribbeck and Jonathan Döring - for teaching me how to SNOM.

Oliver Schmidt and Yongheng Huo - for providing superlensing superlenses.

Claudia Neisser and the cleanroom team - for helping me preparing the samples.

Yongmin Liu and Kan Yao - for simulations that fit the experiment.

Wolfgang Seidel and the ELBE team - for the FELBE radiation to be superlensed.

Carsten Franke and Jan Fiedler - for friendly assistance with FTIR- and Hall-measurements.

All other colleagues from HZDR and TU Dresden - for a great time.

My family and my friends - for support in every way.



# Publications

## Publications related to this thesis

(Publications related to the GaAs Superlens highlighted in red)

### *Journals*

#### 01/2015

M. Fehrenbacher, S. Winnerl, H. Schneider, J. Döring, S. C. Kehr, L. M. Eng, Y. Huo, O. G. Schmidt, K. Yao, Y. Liu and M. Helm. Plasmonic Superlensing in Doped GaAs. *Nano Letters*, 15:1057–1061, 2015.

#### 08/2014

J. Döring, H.-G. von Ribbeck, M. Fehrenbacher, S. C. Kehr, and L. M. Eng. Near-field resonance shifts of ferroelectric barium titanate domains upon low-temperature phase transition. *Applied Physics Letters*, 105:053109, 2014.

#### 09/2012

R. Jacob, S. Winnerl, M. Fehrenbacher, J. Bhattacharyya, H. Schneider, M. T. Wenzel, H.-G. von Ribbeck, L. M. Eng, P. Atkinson, O. G. Schmidt, and M. Helm. Intersublevel Spectroscopy on Single InAs-Quantum Dots by Terahertz Near-Field Microscopy. *Nano Letters*, 12:4336–4340, 2012.

### *Conference Contributions (presenting author underlined)*

#### 06/2015

M. Fehrenbacher, S. Winnerl, H. Schneider, J. Döring, S. C. Kehr, L. M. Eng, Y. Huo, O. G. Schmidt, K. Yao, Y. Liu and M. Helm. A plasmonic GaAs near-field superlens. Poster, *German THz Conference*, Dresden, Germany, 2015.

#### 08/2014

M. Fehrenbacher, S. Winnerl, H. Schneider, J. Döring, S. C. Kehr, L. M. Eng, Y. Huo, O. G. Schmidt, K. Yao, Y. Liu and M. Helm. Near-field investigation of a plasmonic GaAs superlens. Poster, *International Conference on the Physics of Semiconductors (ICPS)*, Austin, Texas, 2014.

#### 04/2013

R. Jacob, S. Winnerl, M. Fehrenbacher, J. Bhattacharyya, H. Schneider, M. T.



Wenzel, H.-G. von Ribbeck, L. M. Eng, P. Atkinson, O. G. Schmidt, M. Helm. Terahertz spectroscopy on single buried InAs quantum dots by scanning near-field nano-microscopy. Poster, *International Workshop on Optical Terahertz Science and Technology (OTST)*, Kyoto, Japan, 2013.

#### **07/2012**

R. Jacob, M. Fehrenbacher, S. Winnerl, J. Bhattacharyya, H. Schneider, M. Helm, H.-G. von Ribbeck, L. M. Eng, P. Atkinson, A. Rastelli and O. G. Schmidt. Scanning near-field infrared nano-spectroscopy on buried InAs quantum dots. Poster, *International Conference on Superlattices, Nanostructures and Nanodevices (ICSNN)*, Dresden, Germany, 2012.

### **Other publications**

#### *Journals*

#### **12/2011**

J. Karch, C. Drexler, P. Olbrich, M. Fehrenbacher, M. Hirmer, M. M. Glazov, S. A. Tarasenko, E. L. Ivchenko, B. Birkner, J. Eroms, D. Weiss, R. Yakimova, S. Lara-Avila, S. Kubatkin, M. Ostler, T. Seyller, and S. D. Ganichev. Terahertz Radiation Driven Chiral Edge Currents in Graphene. *Phys. Rev. Lett.*, 107:276601, 2011.

#### **04/2011**

P. Olbrich, J. Karch, E. L. Ivchenko, J. Kamann, B. März, M. Fehrenbacher, D. Weiss, and S. D. Ganichev. Classical ratchet effects in heterostructures with a lateral periodic potential. *Phys. Rev. B*, 83:165320, 2011.

#### **11/2010**

J. Karch, P. Olbrich, M. Schmalzbauer, C. Zoth, C. Brinsteiner, M. Fehrenbacher, U. Wurstbauer, M. M. Glazov, S. A. Tarasenko, E. L. Ivchenko, D. Weiss, J. Eroms, R. Yakimova, S. Lara-Avila, S. Kubatkin, and S. D. Ganichev. Dynamic Hall Effect Driven by Circularly Polarized Light in a Graphene Layer. *Phys. Rev. Lett.*, 105:227402, 2010.

# Eidesstattliche Versicherung

Die vorliegende Dissertation entstand am Helmholtz-Zentrum Dresden-Rossendorf unter wissenschaftlicher Betreuung durch Prof. Dr. Manfred Helm, Professor im Institut für Angewandte Physik der Fakultät Mathematik und Naturwissenschaften der Technischen Universität Dresden.

Hiermit versichere ich, dass ich die vorliegende Arbeit ohne unzulässige Hilfe Dritter und ohne Benutzung anderer als der angegebenen Hilfsmittel angefertigt habe; die aus fremden Quellen direkt oder indirekt übernommenen Gedanken sind als solche kenntlich gemacht. Die Arbeit wurde bisher weder im Inland noch im Ausland in gleicher oder ähnlicher Form einer anderen Prüfungsbehörde vorgelegt.

Ich erkenne die Promotionsordnung der Fakultät Mathematik und Naturwissenschaften der Technischen Universität Dresden in der aktuell gültigen Fassung an.

Dresden, \_\_\_\_\_ 2015

\_\_\_\_\_  
Markus Fehrenbacher



Bautzner Landstr. 400  
01328 Dresden, Germany  
Tel. +49 351 260-3522  
Fax +49 351 260-13522  
s.winnerl@hzdr.de  
<http://www.hzdr.de>